3D *Coiling* at the Protrusion Tip: New Perspectives on How Cancer Cells Sense Their Fibrous Surroundings

Apratim Mukherjee

Dissertation submitted to the faculty of the Virginia Polytechnic Institute and State University in partial fulfillment of the requirements for the degree of

Doctor of Philosophy

In

Mechanical Engineering

Amrinder S. Nain, Co-Chair

Bahareh Behkam, Co-Chair

Yong Woo Lee

Rafael Davalos

Xiaoyu (Rayne) Zheng

Date: 2.26.2021

Blacksburg, Virginia

Keywords: Protrusion, *coiling*, extracellular matrix fibers, biophysical sensing, cell migration, cell forces, ovarian cancer, cancer progression, metastatic potential, curvature sensing proteins

3D *Coiling* at the Protrusion Tip: New Perspectives on How Cancer Cells Sense Their Fibrous Surroundings

Apratim Mukherjee

ABSTRACT

Cancer metastasis, the spread of cancer from the primary site to distant regions in the body, is the major cause of cancer mortality, accounting for almost 90% of cancer related deaths. During metastasis, cancer cells from the primary tumor initially probe the surrounding fibrous tumor microenvironment (TME) prior to detaching and subsequently migrating towards the blood vessels for further dissemination. It has widely been acknowledged that the biophysical cues provided by the fibrous TME greatly facilitate the metastatic cascade. Consequently, there has been a tremendous wealth of work devoted towards elucidating different modes of cancer cell migration. However, our knowledge of how cancer cells at the primary tumor site initially sense their fibrous surroundings *prior* to making the decision to detach and migrate remains in infancy. In part, this is due to the lack of a fibrous *in vitro* platform that allows for precise, repeatable manipulation of fiber characteristics. In this study, we use the non-electrospinning, Spinneret based Tunable Engineered Parameters (STEP) technique to manufacture suspended nanofiber networks with exquisite control on fiber dimensions and network architecture and use these networks to investigate how single cancer cells biophysically sense fibers mimicking *in vivo* dimensions. Using high spatiotemporal resolution imaging (63x magnification/1-second imaging interval), we report

for the first time, that cancer cells sense individual fibers by *coiling* (i.e. wrapping around the fiber axis) at the tip of a cell protrusion. We find that *coiling* dynamics are mediated by both the fiber curvature and the metastatic capacity of the cancer cells with less aggressive cancer cells showing diminished *coiling*. Based on these results, we explore the possibility of using *coiling* in conjunction with other key biophysical metrics such as cell migration dynamics and forces exerted in the development of a genetic marker independent, biophysical predictive tool for disease progression. Finally, we identify the membrane curvature sensing Insulin Receptor tyrosine kinase Substrate protein of 53 kDa (IRSp53) as a key regulator of protrusive activity with IRSp53 knockout (KO) cells exhibiting significantly slower protrusion dynamics and diminished *coil* width compared to their wild-type (WT) counterparts. We demonstrate that the hindered protrusive activity ultimately translates to impaired contractility, alteration in the nucleus shape and slower migration dynamics, thus highlighting the unique role of IRSp53 as a signal transducer – linking the protrusive activity at the cell membrane to changes in cytoskeletal contractility. Overall, these findings offer novel perspectives to our understanding of how cancer cells biophysically sense their fibrous surroundings. The results from this study could ultimately pave the way for elucidating the precise fiber configurations that either facilitate or hinder cancer cell invasion, allowing for the development of new therapeutics in the long term that could inhibit the metastatic cascade at a relatively nascent stage and yield a more promising prognosis in the perennial fight against cancer.

3D *Coiling* at the Protrusion Tip: New Perspectives on How Cancer Cells Sense Their Fibrous Surroundings

Apratim Mukherjee

GENERAL ABSTRACT

Cancer is a leading cause of death worldwide. Almost ninety percent of cancer related deaths arise from the spreading of cancer cells from the primary tumor site to secondary sites in the body – a processed termed as metastasis. The environment surrounding a tumor (tumor microenvironment) is highly fibrous in nature and can assist in the metastatic process by providing biophysical cues to the cells at the tumor boundary. These cells sense the presence of the surrounding fibers by extending "arms" termed as protrusions, and then eventually detach from the primary tumor and start migrating through the fibrous microenvironment. While numerous studies have investigated the various modes of cell migration in fibrous environments, there is very little information regarding how cancer cells use protrusions to initially sense the fibers prior to detaching. In this study, we used the Spinneret based Tunable Engineered Parameters (STEP) technique to manufacture suspended nanofiber networks with robust control on fiber diameter and network architecture and use these networks to systematically investigate how single cancer cells biophysically sense fibers that mimic in vivo dimensions. We discovered that cancer cells sense individual fibers by "wrapping-around" the axis of the fiber at the tip of the protrusion – a phenomenon we refer to as coiling. We found both the fiber diameter as well as the invasive capacity of cells can influence the coiling mechanics. Based on these results, we explored the use of coiling in conjunction with other key biophysical metrics such as the cell migration speed and

how much force a cell can exert to develop a biophysical predictor for cancer cell aggressiveness. Finally, given that cells sense the fiber curvature by coiling, we explored the role of a key curvature sensing protein Insulin Receptor tyrosine kinase Substrate protein of 53 kDa (IRSp53) in mediating coiling activity and found that knocking out (KO) IRSp53 results in reduced coiling and slower protrusions compared to wild-type (WT) cells. Furthermore, IRSp53 KO cells showed impaired contractility which led to an alteration in the nucleus shape and slower migration dynamics thus highlighting the role of IRSp53 in linking changes at the cell membrane to the underlying cell skeleton. The results from this study could ultimately help us understand what type of fiber conditions around a primary tumor would either help or delay the emergence of the tumor boundary cells and thus allow for the development of therapeutics that could significantly slow down the metastatic process at a relatively early stage.

Dedicated to the memory of my grandparents: Tatu, Dida, and Dadu. Your wisdom I miss every day and your love I will cherish for always.

Acknowledgement

I am extremely grateful for everyone who has helped me along this rewarding journey at Virginia Tech. While my words will never be enough to repay everyone, here is my humble attempt to acknowledge their invaluable support.

First and foremost, I would like to thank my co-advisors Dr. Nain and Dr. Behkam for guiding me along this PhD. They have supported me when I needed it, have pushed me when required and have overall kept my curiosity for science burning even stronger than when I started. Thus, I will forever value their wisdom and guidance. I would also like to thank my committee members Dr. Davalos, Dr. Zheng, and Dr. Lee for agreeing to serve on my committee and for providing me with valuable feedback during the course of my time here. I am immensely grateful to the administrative and support stuff at both ICTAS and at the Mechanical Engineering offices at Randolph and Goodwin, in particular Erin, Shelley, Kim, Cathy and Diana. Without your help, my projects would not have moved as smoothly as they did. I want to acknowledge my colleagues in both STEP Lab and MicroN Base Lab: Abinash, Aniket, Jugroop, Eric, Ying, Puja, Alex, Christian, Daniel, Aldwin, Lauren, Irene, Hajar, Alvin, Maria-Fe, Chris, Zhou, Carmen, Carolyn. It has been a true pleasure working with and interacting with each of you. I couldn't have done any of this without you. I want to specially acknowledge three colleagues. Abinash, and Aniket – your unbreakable friendship, laughs and support during these years I will never forget. Lauren – the great conversations we had about science and the world kept me ever motivated.

Finally, none of this would have been possible without the unconditional love and support from my parents Ashesh and Nandita, my brother Soham and my girlfriend Yanel. To have you all in my life is a blessing I count every single day. Thank you for everything.

Attribution

Chapter 4:

Megan Brown (MS Student, Department of Human Nutrition, Foods and Exercise, Virginia Tech, United States) helped with the cell culturing of the MOSE lines and some of the protrusion analysis.

Daniel Zhang (MS Student, Department of Mechanical Engineering, Virginia Tech, United States) helped with the analysis of the FNE and FNLE cells.

Chapter 5:

Hooi Ting Hu, Tamako Nishimura, and Kyoko Hanawa-Suetsugu (graduate students in the lab of Dr. Shiro Suetsugu, Division of Biological Science and Data Science Center, Nara Institute of Science and Technology, Japan), helped design the IRSp53 reconstituted cell lines.

Dr. Shiro Suetsugu (Professor, Division of Biological Science and Data Science Center, Nara Institute of Science and Technology, Japan) conducted the speckled actin flow experiments.

Jonathan Ron (Postdoctoral fellow in the lab of Dr. Nir Gov, Department of Chemical and Biological Physics, Weizmann Institute of Science, Israel) developed the migration model.

Table of Contents

List of Abbreviations

AFM: Atomic Force Microscopy

ANOVA: Analysis of Variance

BAR: Bin/amphiphysin/Rvs

DMEM: Dulbecco's Modified Eagle's Medium

ECM: Extracellular Matrix

FBS: Fetal Bovine Serum

FCS: Fetal Calf Serum

IRSp53: Insulin Receptor tyrosine kinase Substrate protein of 53 kDa

MOSE cancer model: Mouse Ovarian Surface Epithelial cancer model

nN: nanoNewton

PBS: Phosphate Buffered Saline

PS: Polystyrene

STEP: Spinneret based Tunable Engineered Parameters

TACS: Tumor Associated Collagen Signature

List of Figures

image shows a fused fiber junction. Scale bar is 2 µm. The fluorescent image shows actin filaments in red, nucleus in blue and focal adhesion protein paxillin clustering in yellow. Scale bar is 20 µm. NFM establishes force vectors that originate from focal adhesion clusters and are directed along the actin stress fibers. An inverse finite element model minimizes the error between computational and experimental fiber deflections. (B) Representative fluorescence microscopy images of (i) WT (top) and KO (bottom) cells with actin stained in red and (ii) quantification of the stress fiber angles for both cell types on 135 and 500 nm diameter fibers. Scale bars are 10 µm. Dotted white lines in the fluorescent images depict the stress fiber angles. n values are 25 and 25 for the KO cells and 25 and 27 for WT cells on 135 nm and 500 nm diameter fibers respectively. (C) Representative phase images of (i) WT (top) and KO (bottom) cells exerting forces by pulling on suspended fibers with scale bars of 50 µm and (ii) quantification of the forces exerted for both cell types on 135 and 500 nm diameter fibers. n values are 25 for both cell types on each of the two fiber diameters investigated. (D.i) Representative heat maps in arbitrary units of the actin stress fiber distributions for the two cell types with scale bars of 10 µm. (ii) Representative confocal images of WT and KO nucleus cross-section (yz plane) with scale bar of 5 µm, and (iii) quantification of the nucleus thickness. (E.i) Representative heat maps in arbitrary units of the actin stress fiber distributions for the two cell types attached to single fibers in spindle shapes with scale bars of 10 µm, (ii) Representative confocal images of WT and KO nucleus cross-section (yz plane) with scale bar of 5 µm, and (iii) quantification of the nucleus invagination aspect ratio (AR). The schematic in E.ii shows how AR was measured. In the confocal images, the nucleus is in blue, the nuclear envelope is in cyan and the cross-section of the suspended fibers is in red shown using yellow arrowheads. n values are 18 for the nucleus thickness measurements in (D) and 25 for the invagination AR measurements in (E) for both cell types on each of the two fiber diameters

and (ii) KO cells. All scale bars are 50 µm. (B) Representative area, perimeter and circularity profiles for (i-iii) WT cells and (iv-vi) KO cells on 500 nm diameter suspended fibers. Quantification of the (vii) average change in area, (viii) average change in perimeter, and (ix) average change in the circularity of WT and KO cells on both 500 nm diameter suspended fibers and flat, 2D surfaces. n values are 35 for both cell types on the 500 nm diameter suspended fiber and 30 for both cell types on the flat surface respectively. All error bars shown represent standard error of mean……………………………………………………………………………**102**

Supplementary Figure 5.S9: Speckle microscopy of actin flow. Fluorescence speckled microscopy images of both WT and IRSp53 KO cells on both 2D glass substrate (left panel) and suspended fiber networks (right panel)………………........…………………………………**103**

Figure 6.1: U-251 glioblastoma cell exhibiting *coiling* in the collagen matrix. The collagen concentration used here was 1 mg/ml. Scale bar is 10 µm……………………………….**106**

Chapter 1: Overview

Research Objectives:

While decades of work has focused on investigating how cancer cells migrate through the fibrous tumor microenvironment, relatively little has been elucidated about how cancer cells at the tumor-stroma interface initially sense their fibrous environment by utilizing protrusions, extensions from the cell body, prior to detaching and migrating. Although some studies have previously attempted to characterize protrusion structure and dynamics, they are primarily conducted on flat, 2D platforms which are unable to recapitulate the complex fibrous nature of the extracellular matrix (ECM) *in vivo*. Given that the ECM fiber dimensions and network architecture have proven to be crucial drivers of the metastatic cascade, understanding single cell-fiber interactions, especially in the context of cancer cell protrusions becomes imperative. Armed with this knowledge, we can begin to unravel what type of fiber size, orientation and architecture either promote or hinder cancer metastasis.

The overarching goal of this work was to investigate how single cancer cells sensed ECM-mimicking suspended fibers. To this end, we used the previously reported non-electrospinning Spinneret based Tunable Engineered Parameters (STEP) technique to manufacture suspended nanofiber matrices. In comparison to other fiber manufacturing techniques, the STEP technique allows exquisite control over fiber diameter and network architecture. Here, we report, for the first time to our knowledge, that cancer cells sense fibers by wrapping around the fiber axis at the tip of the protrusion, a phenomenon we term as *coiling*. We investigated how the fiber properties influenced *coiling* morphodynamics and further enquired whether this novel biophysical metric could be used towards the development of a genetic-marker independent predictor of metastatic capacity. Finally, we explored the role played by key membrane curvature sensing proteins in

translating the protrusive activity at the cell membrane to the underlying cytoskeleton in order to establish contractility and ultimately mediate cell migration.

Organization of the Document:

This document provides a comprehensive outline of the studies performed using the STEP technique to interrogate how single cancer cells sense suspended fibers mimicking *in vivo* ECM dimensions. Chapter 2 provides a detailed background of how the biophysical cues provided by the fibrous tumor microenvironment aid in the metastatic cascade and therefore builds the case for the development of an *in vitro* fibrous platform that allows for repeatable, systematic investigation of single cell-fiber interactions. Chapter 3 describes the *coiling* mechanism observed at the tip of the protrusion used by cancer cells to sense suspended fibers. It proposes that the occurrence of *coiling* is intrinsically linked with the extension of cell protrusions and both the fiber diameter and cancer cell aggressiveness can modulate *coiling* activity. Chapter 4 focuses on harnessing the capacity of *coiling* as a predictive tool for developing a genetic marker independent, biophysical metastatic index in a syngeneic ovarian cancer progression model. It proposes that *coiling* can be used in conjunction with other key biophysical metrics such as the protrusive and migration dynamics and forces exerted by single cells to predict the metastatic capacity of cancer cells in a fast, repeatable and reliable manner. Chapter 5 explores the role played by Insulin Receptor tyrosine kinase Substrate protein of 53 kDa (IRpP53) , a key membrane curvature sensing protein in both mediating protrusive and *coiling* activity and translating the activity at the cell membrane to the underlying cytoskeleton to establish contractility and promote efficient migration. This chapter suggests that in the absence of IRSp53, both protrusive and *coiling* dynamics are severely hindered which ultimately leads to an impairment in the cell contractility, an effect that is only captured on the suspended fibers and not on the flat, 2D surface. Furthermore, in this chapter, we

describe how the absence of IRSp53 slows down cell migration dynamics and causes a partial decoupling of the nucleus from the cytoplasm, a previously unreported behavior. Finally, Chapter 6 suggests the potential impact of the findings from this study and offers future avenues to be pursued.

Chapter 2: Introduction

Fibrous Tumor Micro-Environment Aids in Cancer Metastasis:

In 2021, approximately 1.9 million people are projected to be diagnosed with cancer in the United States alone leading to ~600,000 deaths, which translates to almost 1,640 deaths every single day[1]. In fact, cancer is widely reported to be the second most common cause of death in the United States, exceeded only by heart related complications. 90% of cancer related deaths are due to metastasis, i.e. the dissemination of cancer cells from the primary tumor site to secondary and tertiary sites in the body where they can recolonize[2]. The metastatic process is a complex series of events that involves interrelated steps and is often referred to as the "invasion-metastasis cascade"[3]. This cascade begins with cancer cells evading the normal cell-cell junctions and undergoing a transition from epithelial cells with minimal migratory capability to mesenchymal cells that are capable of migration and invasion through the surrounding extracellular matrix (ECM) referred to as the epithelial-to-mesenchymal transition (EMT)[4,5]. Subsequently, the migratory cells that have escaped the cell-cell junctions (leader cells) secrete matrix metalloproteinases (MMPs) that help to cleave the surrounding extracellular matrix (ECM) and thus allow the population of migrating tumor cells to invade through the basement membrane and migrate towards the surrounding blood and/or lymphatic vessels[6–10]. The migrating cancer cells can then intravasate into the vessels and travel to distant sites via the circulatory system[11]. Finally, the cells adhere to the endothelial layer of capillaries at the target organ site and subsequently extravasate into and colonize the surrounding basement membrane[12,13].

While previous studies have focused on the accumulation of genetic alterations in cells as the driving force behind the acquisition of metastatic capacity[14] it has recently been recognized that the ECM surrounding a primary tumor, referred to as the tumor microenvironment (TME) also

plays a crucial role in facilitating metastasis[3,15–17]. The ECM is a complex three-dimensional fibrous biopolymer network embedded in a viscous macromolecular gel which can further be categorized into major types: the fibrous connective interstitial[18] matrix and the densely packed basement membrane pericellular matrix[19]. In the context of the fibrous ECM, collagen and elastin have been identified as the key structural components[20]. These fibrous proteins are supplemented by a macromolecular network of hydrophilic and acidic components like proteoglycans, hyaluronic acid, etc., which are capable of sequestering water and forming a viscous gel around the fibrous network[21]. *In vivo* imaging of the ECM using second harmonic generation (SHG), third harmonic generation (THG), multiphoton microscopy and electron microscopy has revealed a complex hierarchical network of fibers, which is comprised of individual fibers (30 - 70nm diameter) that can form bundles (100 nm-microns in diameter)[18,20,22–26]. Specifically in the context of cancer metastasis, the ECM can facilitate the metastatic cascade by providing tumor cells a combination of biochemical and biophysical cues while in turn, the tumor cells can actively remodel the fibrous network, thus establishing a dynamic reciprocity[27,28].

Role of Biophysical Cues in Cancer Metastasis

The accelerated post-translational modification of the ECM via elevated protein deposition, fiber cross-linking, and MMP-mediated collagen remodeling, can lead to significant changes to the ECM architecture surrounding the tumor[29]. A particularly striking result of the constant ECM remodeling in the tumor microenvironment is the increasing linearization of collagen fibers adjacent to developing tumors as revealed by recent developments in SHG and multiphoton microscpy[30]. The aligned fiber networks are expected to provide the leader cells an efficient pathway for migration through the tumor stroma. In fact, biopsy samples from breast cancer patients reveal clear patterns of aligned collagen fibers (perpendicular to the tumor

periphery) with tumor progression, termed as "tumor associated collagen signatures" (TACS). During the initial stages, tumors exhibit a localized increase in the collagen deposition adjacent to the tumor boundary (termed as TACS-1). As the tumor increases in size, the collagen fibers that were initially aligned parallel to the tumor boundary continue to straighten (TACS-2) until they are finally bundled and aligned perpendicular to the tumor boundary (TACS-3). The alignment of ECM fibers perpendicular to the tumor boundary in TACS-3 is significant since recent studies have demonstrated that the mammary tumor colonies are able to coordinate and assemble long, aligned collagen lines which subsequently led to an accelerated transition to invasive phenotypes[31]. Furthermore, aligned collagen fibers as shown in TACS-3 have also been correlated with threefold increased risk of relapse or death for patients[32–35]. Other studies have focused on characterizing the speed of the cells after their emergence onto the aligned fibers as well as highlighting the different degrees of interaction between metastatic and non-metastatic cancer cells. For instance, one study found that in the non-metastatic MT3 tumors there were very rare interactions with single cells and the collagen fibers. In contrast, in metastatic MTLn3 tumors, individual cells frequently made contact with the radially aligned fibers and proceeded to move in a linear fashion along the fiber length[36,37]. The relationship between *in vivo* fiber alignment and cancer metastasis is not limited to TACS in breast cancer however. Previous studies in the context of the brain cancer microenvironment have also demonstrated that glioblastoma cells can align themselves and ultimately migrate along axon bundles in the central nervous system[38]. These bundles are partly comprised of fibers that can range from 400 nm to 7μm in diameter and much like the TACS-3 condition in the breast tumor microenvironment, act as potential "highways" to expedite the metastatic cascade[39,40].

Cancer Cells Use Protrusions to Sense the Tumor Microenvironment:

In addition to the fiber alignment discussed above, ECM fibers adjacent to the tumor provide a myriad of other biophysical cues to the tumor boundary cells manifesting in the form of fiber diameter, inter-fiber spacing, fiber network stiffness, and even single vs bundles of fibers. Cells at the tumor boundary constantly probe the fibers by extending lateral protrusions, i.e. projections from the cell cytoplasm (**Figure 2.1.A,B**). *In vivo* imaging using intravital confocal microscopy has indeed shown cells at the boundary of human head and neck (HEp3) tumors tend to preferentially extend protrusions perpendicular to the tumor boundary and sense the adjacent collagen fibers[41]. Over time, these protrusions grow in length, and the tumor boundary cells are able to detach from the primary tumor and start migrating through the TME in the form of single
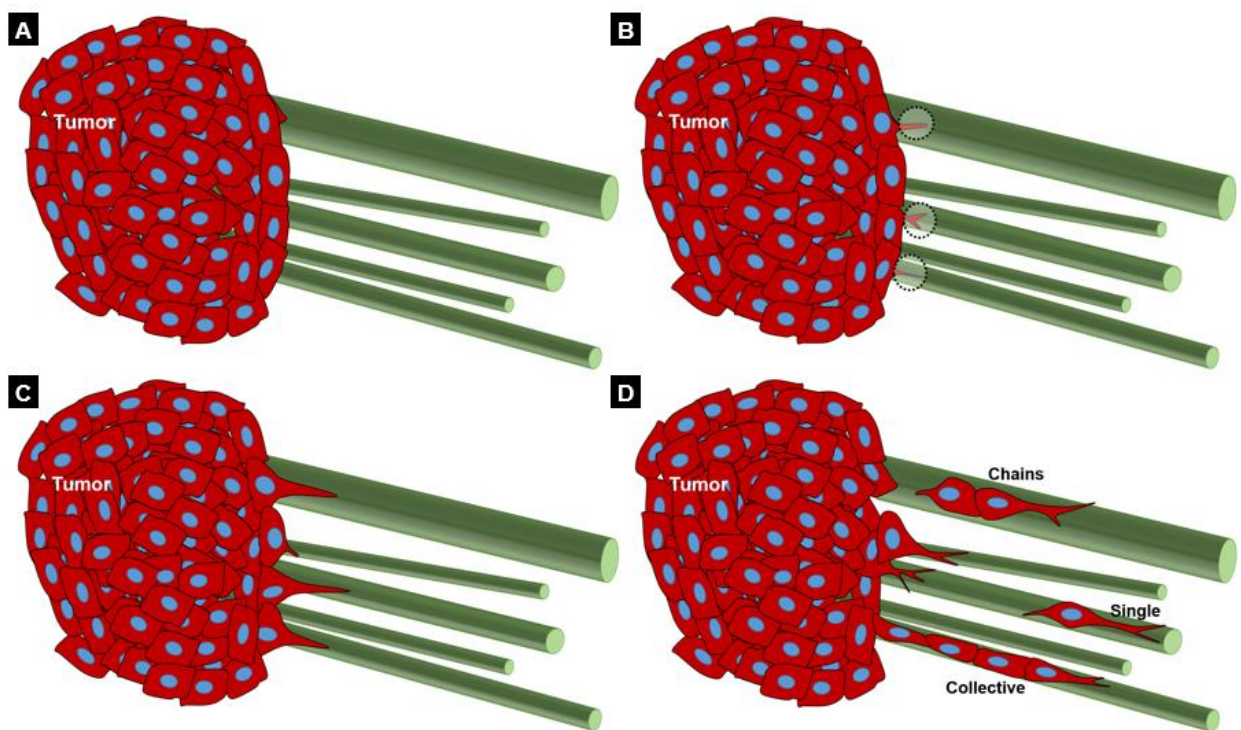
Figure 2.1: Schematic showing how tumor boundary cells detach from the primary tumor and start migrating through the fibrous tumor microenvironment. (A, B) Tumor boundary cells extend lateral protrusions to probe the fibrous surrounding. **(C)** As these protrusions increase in length, the boundary cells detach from the tumor and start migrating through the tumor microenvironment as **(D)** single cells, chains of few cells or collective streams of cells.

cells, chains of multiple cells or even collective groups of cells (**Figure 2.1C, D**). These different

modes of tumor cell migration following the detachment from the primary tumor have been studied

previously in great detail[42]. Single cell migration can be further divided into mesenchymal versus

amoeboid migration depending on the migration mechanism used[43–45]. Mesenchymal migration

typically incorporates a tightly controlled and regulated cascade of events beginning with the

extension of a protrusion through which the cell then develops focal adhesions that helps the cell

to attach to the surrounding matrix via the transmembrane integrin proteins. Subsequently, a

combination of the dissolution of focal adhesions at the cell rear and acto-myosin mediated

contractility forces help propel the cell forward as it begins this cycle again[46]. In contrast to

mesenchymal cells, amoeboid cells, such as lymphoma, small-cell lung carcinoma, and small-cell

prostrate cancer cells exhibit a significantly faster, propulsive mode of migration that is not heavily

reliant on cell-matrix adhesions[47,48]. Chain migration, commonly observed in melanomas, occur

when cells stream out one after another resembling a "strand" of cells. Interestingly, during chain

migration, cells are able to maintain cell-cell adhesion which is hypothesized to facilitate in

intercellular communication[49,50]. Finally, collective cell migration involves the movement of

aggregated cells as a single functional unit rather than as individual cells or groups of cells.

Collective cell migration is typically characterized by "leader" cells at the invasion front that

generate the pathway for the "follower" cells via active matrix remodeling[51,52]. Despite the wealth

of knowledge regarding the various modes of migration of tumor cells post-detachment from the

primary tumor, our knowledge of how the tumor boundary cells initially sense the fibers

surrounding the tumor through the extension of protrusions remains in infancy. Understanding this

is crucial since protrusions are widely considered as pre-cursors of and requisite for cell

migration[42]. Thus, a detailed description of how cells deploy protrusions to sense the fibrous ECM

in the tumor microenvironment could ultimately pave the path towards discerning what type of fiber architectures either aid or hinder the metastatic cascade during the very nascent stages before the cancer cells have even started migrating through the stroma.

Fundamentals of Cellular Protrusions Studied on 2D Surfaces:

Cell protrusions that initiate ECM recognition have most commonly been studied on flat, 2D surfaces. Protrusions are generated through the polymerization of actin filaments in response to the activation by signaling cascades at the plasma membrane[53]. On the flat surface, two major types of protrusions have been identified – lamellipodia and filopodia[54,55]. The lamellipodium is a broad, "sheet-like" projection that is ~2-4 μm wide and is composed of branched actin networks[56]. In contrast, filopodia are short, "finger-like" projections, ~0.1-0.3 μm wide and ~3-10 μm in length that are located anterior to the lamellipodia and are composed of parallel bundles of tightly packed actin filaments[56]. In terms of function, the lamellipodia plays a key role in establishing focal adhesion linkages with the underlying substrate while the filopodia is widely envisioned as a cellular "sensor" constantly exploring the surrounding matrix and detecting soluble cues[57–59]. In addition to the differences in composition and function, the lamellipodia and filopodia are regulated by different batteries of protein scaffolds that connect the RhoGTPase signaling molecules to the growing actin filaments. In the case of the lamellipodium, the signaling proteins Cdc42 and Rac1 play a key role in first activating the Wiskott-Aldrich Syndrome Proteins (WASP) complex and cortactin by inducing conformational changes[60]. These complexes then in turn help to activate the Arp 2/3 complex which itself is comprised of 7 different proteins[61]. Finally, the Arp 2/3 complex initiates nucleation from the side of the mother filament, typically at an angle of ~70 degrees[56]. In the case of the filopodia, while there remains some debate over the nucleation mechanism, the most widely accepted current model posits that the actin filaments first form the

typical branched networks as seen in the lamellipodium mediated by the Arp 2/3 complex but are subsequently elongated by formin and Vasodilator-stimulated phosphoprotein (VASP) into parallel bundles[62,63]. The proteins formin and profilin also play important roles in the nucleation process of the actin network in the filopodia once the parallel bundles have been arranged. Formin in its default state exists in an auto-inhibited conformation[60]. On activation by Rho GTPases, it acts as a "leaky capper" thus inhibiting the growth of the actin network[64]. However, in the presence of profilin, it is transformed from a "leaky capper" to a strong nucleation promoter[64,65].

BAR Domain Proteins Play a Key Role in Protrusive Activity:

In the context of protrusive activity, the crescent-shaped Bin/amphiphysin/Rvs (BAR) domain proteins play a crucial role in both generating and sensing membrane curvature at the cell boundary [66–68]. These proteins can generate membrane curvature by binding to the cell membrane and sometimes by inserting amino acids on their membrane-binding surface into the membrane while they can sense membrane curvature by binding to specific membrane sites that fit their curved structure at their low concentration[67].

The BAR domain family can be broadly subdivided into three categories on the basis of their amino-acid sequence conservation. The canonical BAR and F-BAR domains possess an intrinsically curved concave surface and are typically involved in the formation of membrane invaginations including clathrin-coated pits, caveolae, and transverse tubules. In contrast, the I-BAR
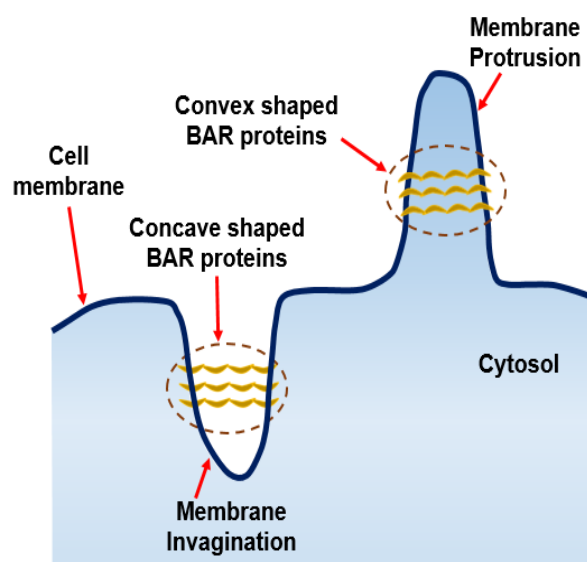
Figure 2.2: Schematic showing the different types of BAR proteins and the resulting membrane deformations.

domains possess an intrinsically curved convex surface and are involved in the extension of cell protrusions such as the filopodia or lamellipodia which were discussed earlier[59,69] (**Figure 2.2**).

In addition to their role in mediating protrusive activity at the cell membrane, these proteins constitute a functional platform at the interface between the plasma membrane and the actin cytoskeleton facilitating the bidirectional signal transduction between the cell boundary and key cytoskeletal regulating proteins[59,70].

Protrusion Studies in Higher Dimensions Lack a Tunable Fibrous Component:

In contrast to studying protrusions on flat 2D surfaces as described in detail above, several recent studies have attempted to elucidate the protrusive structure and dynamics in ~2.5D Boyden chamber derivative assays. These studies have revealed that cells plated on the top of a gel surface can extend protrusions into the gel matrix by degrading the matrix. These protrusions have been alternatively been referred to as either invadopodia in the context of cancer cells or podosomes in the context of non-cancer cell lines[71–73]. Further studies have demonstrated that invadopodia are composed of an actin-rich core surrounded by a chorus of scaffolding proteins including WASP, Arp2/3 complex, cortactin and Tks5 and are capable of recruiting matrix metalloproteases (MMPs) to facilitate the ECM degradation[74,75]. In support of these *in vitro* results, several studies have identified invadopodia in *in vivo* settings, especially during the intravasation and extravasation steps in the context of metastatic breast cancer cells[76].

Finally, protrusive behavior has also been interrogated in 3D, gel-based matrices. Cells seeded in 3D gels typically extended branched protrusions that are thinner than the lamellipodia and longer than the filopodia observed in 2D environments[77]. These actin-rich, dendritic protrusions are typically termed pseudopodia. In the context of 3D gels, pseudopodia, similar to

invadopodia and podosomes described earlier, can play a significant role in remodeling and degrading the gel, allowing for pathways for cell migration through the gel[78]. In contrast to these branched protrusions, other studies have also identified blunt, cylindrical protrusions termed as lobopodia which are driven primarily by cytoplasmic flow rather than actin filament polymerization[79]. **Table 2.1** summarizes the different types of protrusions that have been previously studied on 2D, 2.5D and 3D environments.

While these assays have provided a wealth of information regarding the structure and dynamics of cell protrusions that are extended to sense the surrounding matrix, they crucially lack the fibrous component observed in the *in vivo* ECM thus offering limited physiological relevance

Category	Protrusions in 2D		Protrusions in ~2.5D		Protrusions in 3D	
	Lamellipodia	Filopodia	Podosome	Invadopodia	Pseudopodia	Lobopodia
Structure	Broad, "sheet-like" projection	Short, "finger-like" projection	Actin-rich core, surrounded by signaling proteins		Long, "finger-like" projections; typically seen in 3D gels	Blunt, cylindrical projection; typically seen in 3D gels
Location	Leading edge of the cell	Anterior to the lamellipodia	Ventral surface; behind the leading edge	Ventral surface, clustered under nucleus	Leading edge of the cell	Leading edge of the cell
Dimension	Width: ~2-4 µm	Width: 0.1-0.3 µm Length: 3-10 µm	Width: 0.5-2 µm Length: 0.5-2 µm	Width: 0.5-2 µm Length: 0.5-2 µm	Thinner than lamellipodia; Length: >5 µm	~5-8 µm
Actin Arrangement	Crosslinked and Branched	Parallel bundles	Branched and Unbranched	Branched and Unbranched	Crosslinked and Branched	N/A
Key Nucleation Factors	CDC 42, Rac1, Cortactin	CDC 42, Rac1, Cortactin	RhoA, CDC 42, Cortactin	RhoA, CDC 42, Cortactin	CDC 42, Rac1, Cortactin	RhoA, ROCK
Duration	Minutes	Minutes	Minutes	Hours	Minutes-Hour	N/A
ECM Degradation	Minimal	No	Yes (potentially through the recruitment of metalloproteases)		Yes	No

Table 2.1: Key characteristics and hallmarks of different types of protrusive structures.

in their scope. These assays are unable to recapitulate and investigate the initial sensing of the fibers adjacent to the primary tumor by the tumor boundary cells prior to their detachment and subsequent migration. Thus, there is a critically unmet need for fibrous platforms with a high degree of repeatability and control to systematically interrogate the initial probing of their surroundings by cancer cells.

Current Methods for Manufacturing Fibrous In Vitro Assays: Features and Drawbacks:

Arguably the most common method used for manufacturing fiber based *in vitro* platforms till date is electrospinning which allows for the production of fibers ranging from tens of nanometer to few microns in diameter[80–83]. Briefly, this method involves the pumping of a polymer solution through a syringe into a needle exposed to an electrical charge which ultimately leads to the extrusion of the polymer fibers onto a target. With the realization that electrospinning could produce fibers with diameters on the order of those in native tissue, the bioengineering community has seen rapid growth in the use and improvement of electrospinning technique to achieve higher degree of alignment and spatial organization. However, due to the inherent electric instabilities of the electrospinning process, a high degree of parallelism, control on diameter, and the spacing between fibers is difficult to control in multiple layers, which restrict the scope to which cell-fiber interactions can be investigated using electrospinning methods.[84–89] Furthermore, since the jet path of the extruded filament is influenced by the externally applied electric field, the use of multiple nozzles in the same setup has been limited due to mutual Coulombic interactions, resulting in non-uniform, non-woven mats[90–97]. Some of the recent advancements in this respect include far-field electrospinning (FFES) and near-field electrospinning (NFES)[98–111]. In FFES, aligned fibers are generated by using a high-speed rotating drum acting as a collector in place of a stationary target[107], wheel-like bobbin collector[109,110], and patterned electrodes[108] or by modifications to the electric

13

source including using biased AC potentials or an auxiliary counter electrode[100,111]. On the other hand, NFES has demonstrated improved fiber patterning through reduction of applied voltage and the source-to-target distance[102,112].

In order to achieve higher consistency and control in fiber diameter and alignment, Brown et al. (2011) introduced the direct write melt electrospinning approach, where instead of electrospinning polymer solutions as performed in conventional electrospinning techniques, polymer melts at elevated temperatures (~70-90 $^{\circ}$C) were electrospun[113]. In addition, a significantly lower tip-to collector distance was used to ensure minimal spread of the extruded polymer fibers. While this approach is able to produce 3D fibrous matrices in various hierarchical architectures with a good degree of fiber alignment, the reported fiber diameters are large (typical fiber diameter ~ 20 µm), and extension to nanofibers remains to be demonstrated.

Since decreasing voltage enhances fiber deposition capabilities, several approaches have removed the electric component entirely. For instance, Badrossamay et al. (2010) demonstrated the rotary jet spinning approach, where, instead of an electric source, centrifugal forces associated with the rotation of a perforated polymer solution reservoir were utilized to extrude polymer nanofibers[114,115]. Continuous, bead-free nanofibers were obtained at very high rotational speeds (~12,000 RPM) of the perforated reservoir. Pull spinning is another very recent technique demonstrated by Deravi et al., in which devoid of any electric source is able to achieve moderate success in aligning fibers but still lacks control in inter-fiber spacing[116,117]. Similar to rotary jet spinning, this approach also utilizes a rotating component for fiber generation. However, instead of an entire rotating perforated reservoir of the polymer solution, a high-speed rotating bristle pulls a polymer droplet into a nanofiber, mainly by the action of the axial stretching forces associated with the bristle rotation.

STEP Method Allows Repeatable Investigation of Cell-Fiber Interaction:

While some of the aforementioned fiber spinning techniques have demonstrated the ability to fabricate fiber networks with a fair degree of control on fiber alignment, they are still unable to finely control and tune the fiber dimensions mimicking a wide range of diameters as observed in the native ECM (sub 100 nm – microns) and spatial architectures which are key to interrogating single-cell protrusive behavior in a repeatable manner.

In this regard, Nain, *et al.*, have pioneered the Spinneret based Tunable Engineered Parameters (STEP) technique (**Figure 2.3**) for the deposition of suspended fiber networks[118,119]. In contrast to traditional electrospinning, this technique does not require the use of an electric source in the fiber manufacturing process; rather it is based on the physical pull of a single fiber filament from the extruded polymer solution droplet from a spinneret. A rotating substrate
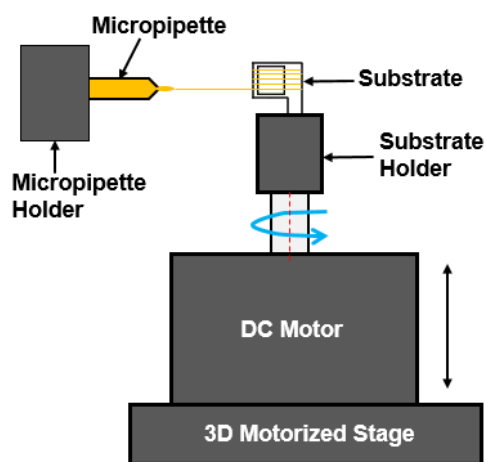
Figure 2.3: Schematic of the non-electrospinning, Spinneret based Tunable Engineered Parameters method.

contacts the droplet and pulls out solution filaments, which after solvent evaporation and solidification are collected on the substrate in parallel configurations at desired spacing[120]. By depositing fibers on top of each other in multiple layers, hierarchical assemblies of fiber networks with tunable unit-cell dimensions can be created. Fiber spinning is achieved through a delicate balance of processing parameters (rotating speed, humidity, temperature, etc.) and material parameters (polymer solution concentration, polymer molecular weight, solvent properties), which have direct effects on fiber diameter and morphology[118].

Overall, the STEP technique provides robust control on fiber diameter, alignment and architecture, thus allowing us to investigate single-cell protrusion dynamics on ECM-mimicking suspended nanofibers in a repeatable manner[23,121,122]. Understanding how cells sense these fibrous networks is crucial since protrusions are widely considered to be pre-cursors of and requisite for subsequent cell migration. Thus, a detailed description of how cells deploy protrusions to sense the fibrous ECM in the tumor microenvironment could ultimately pave the way towards discerning which fiber architectures either aid or hinder the metastatic cascade during its very nascent stages before the cancer cells have even started migrating through the tumor stroma. In the long run, targeted therapeutics could be developed that cause a synthetic remodeling of the fibrous architecture surrounding primary tumors in order to significantly slow down the metastatic cascade allowing physicians significantly longer time to develop overall treatment strategies. For instance, lysyl oxidase (LOX) has been shown to play an integral role in the process of collagen fiber crosslinking and subsequent linearization in the tumor microenvironment[30]. Consequently, strategies have focused on the inhibition of LOX through pharmacological inhibitors and LOX neutralizing antibodies[30,123]. In a recent example, it was shown that the use of the anti-lysyl oxidase like 2 (LOXL2) antibody significantly alters the alignment of the collagen fiber network which subsequently resulted in a decrease in both the velocity and invasion capacity of tumor cells[124].

Summary:

The fibrous tumor microenvironment plays a crucial role in facilitating the metastatic cascade by providing biophysical cues in the form of aligned fibers of different diameters and spatial architectures. Cells at the tumor boundary extend protrusions to probe the surrounding fibers before detaching from the tumor and migrating through the surrounding stroma. While there has been a lot of work focused on characterizing the different modes of migration of cancer cells

through fibrous matrices, how cancer cells initially sense the surrounding fibers prior to making a decision to migrate along the fibers remains poorly understood. Most current studies that have attempted to investigate protrusive dynamics are typically carried out on 2D surfaces or 3D gels which do not recapitulate the fibrous nature of *in vivo* microenvironment and therefore are unable to probe single cell protrusion-fiber interactions in a systematical and repeatable manner. In this regard, the STEP platform allows for the fabrication of suspended fiber networks with a high degree of control over the fiber diameter and network architecture. Using this platform, we can begin to unravel the mechanistic process through which single cancer cells sense individual fibers by extending protrusions. In doing so, we can establish the groundwork for understanding which types of fiber configurations ultimately promote or hinder cancer metastasis.

In order to address the above question, the proposed work in this thesis has been divided into three main components. Firstly, we fabricate tunable fiber networks of contrasting fiber diameters in order to isolate and investigate individual protrusive events. Here, we find that cancer cells sense suspended fibers by *coiling* (i.e. by wrapping around the fiber axis) at the protrusion tip, a previously unreported behavior. Furthermore, we find that the fiber curvature plays a key role in modulating *coiling* dynamics. Prompted by these results, we next investigate whether the protrusive and *coiling* activity can be used as part of a comprehensive suite of biophysical metrics that could serve as potential, genetic-marker independent predictors of the metastatic capacity of cancer cells. Here, we find that *coiling* dynamics at the protrusion tip in conjunction with migration dynamics of the whole cell body serve as useful biophysical indicators of cancer aggression. Finally, we investigate the role of the BAR domain proteins described earlier in linking the protrusive activity at the cell membrane to the underlying cytoskeletal contractility, nucleus shape and ultimately, the migration cycle of cells on suspended fibers. Here, we identify that knocking

out Insulin Receptor tyrosine kinase Substrate protein of 53 kDa (IRSp53), a key BAR member protein results in impaired protrusive and *coiling* activity which translate to reduced cytoskeletal contractility and ultimately, hindered migration dynamics. The findings from this work will add novel insights to our current knowledge of how cancer cells sense and interact continuously with their fibrous surroundings, thus potentially contributing to a better understanding of the metastatic cascade.

Chapter 3: Cancer Cells Sense Fibers by Coiling on Them in a Curvature Dependent Manner

Introduction:[1]

Protrusions are extensions from the cell body that are diverse in shape, molecular structure and location relative to the cell body and play an important role in cell migration and extracellular matrix (ECM) degradation [125–129]. The importance of protrusions as the precursor to migration[130–132], in the presence of biophysical[133,134] and biochemical cues[135–138] is widely documented. In context of cancer, specialized protrusive structures are known to break down the surrounding extracellular milieu[75,139,140].

The ECM through which cells navigate is a complex fibrous network that is composed of a wide range of fiber diameters (tens of nanometers to micrometers[20,141]). *In-vitro* assays, by us and others, have shown that the fiber diameter can have a significant impact on cell behavior by inducing changes in morphology and redistribution of focal adhesion arrangements[142,143]. Using 3D gel assays, recent studies have reported that protrusions can remodel collagen fibers in the matrix in a "hand-over-hand" cycle at the leading edge[144,145] or lateral to cell body[71], and aligned fibers in the gel limit formation of lateral protrusions, thus promoting cell persistence[78,146]. It has also been shown that cells seeded in 3D gels form multiple protrusions simultaneously to "probe" the surrounding matrix fibers before extending a single, stable protrusion to define a front-rear axis[15]. While these investigations have yielded valuable information on the nature of protrusions, our current understanding of how cells biophysically sense ECM fibers remains in infancy.

---

[1] This chapter was published previously by the author: Mukherjee, A., Behkam, B., & Nain, A.S., "Cancer cells sense suspended fibers by coiling on them in a curvature dependent manner", *iScience*, 2019

Using suspended network of fibers of contrasting curvatures (*protrusive* assay) that decouples bulk cell body migration from protrusive dynamics, we have previously shown that normal breast epithelial cells MCF 10A form shorter protrusions compared to the highly metastatic breast adenocarcinoma MDA-MB-231 on fibers of varying diameters. [129]. Briefly, our method allows us to constrain the cell body on large diameter (≥ 2 µm) *base fibers*, while orthogonally deposited smaller diameter *protrusive fibers* elicit protrusive events. Using this platform, here, we report that migratory cells *coil* (wrap-around) on fibers of varying curvature differentially. *Coiling* at the tip of protrusions occurs in bursts during growth phase of protrusions, which synchronizes with endogenous translocation of lipid granules inside protrusions along linear tracks in a persistent super-diffusive manner. Interestingly, depositing a bundle of densely packed small diameter fibers recovers *coiling* dynamics of single large diameter fibers. We also quantitate *coiling* by migrating cells in spindle shapes on single suspended fibers (*migration assay).* We report notable differences in *coiling* behavior between *protrusive* and *migration* assay on large diameter fibers. For the breast cancer model used in this study, we report that non-metastatic MCF 10A exhibit diminished *coiling* in low numbers compared to their metastatic counterparts (MDA-MB-231 and BT-549). Altogether, our results using ECM mimicking fibers lay the groundwork to link biophysical cell sensing with biological signaling to define pro and anti-invasive fibrous environments.

Materials and Methods:

Non-electrospinning STEP Protrusion Platform: The previously reported STEP method[118] was used to spin a crosshatch network of large diameter, "strut-like" base fibers orthogonal to which were deposited the smaller diameter *protrusive* fibers. The networks were then fused at fiber intersections. The base fibers were fabricated to be at least 2 µm whereas 5 different *protrusive*

fiber diameters were used: ~135 nm, ~270 nm, ~450 nm, ~600 nm, and ~1000 nm. Polystyrene (PS, Scientific Polymer Products, Ontario, NY, MW = 2 x 10^6 g mol^{-1}) of ~2x10^6 g/mol molecular weight was dissolved in *p-xylene* (Fischer Scientific, Pittsburgh, PA) at 7, 8, 10, 12 and 14% (w/w) to prepare the polymer solutions prior to spinning the ~135 nm, ~270 nm, ~450 nm, ~600 nm and ~1000 nm diameter fibers respectively. To prepare the ~2000 nm diameter *base fibers*, polystyrene of ~2x10^6 g/mol molecular weight was dissolved in a 1:1 xylene:dimethylformamide solution at a 10% (w/w) concentration. To prepare the ~4000 nm diameter fibers for the migration assay, polystyrene of ~15x10^6 g/mol molecular weight was dissolved in p-xylene at a 6% (w/w) concentration. The interfiber spacing was tuned to be ~200 μm between the *base fibers* and ~75 μm between the *protrusive fibers*.

Cell culture, Seeding: MDA-MB-231 mammary ductal adenocarcinoma cells were cultured in Leibovitz's L-15 media (Thermo Fisher Scientific, Waltham, MA) supplemented with 10% Fetal Bovine Serum (Thermo Fisher Scientific, Waltham, MA). The culture was maintained in an incubator without CO_2 at 37 °C. BT-549 mammary ductal carcinoma cells were cultured in RPMI media (Thermo Fisher Scientific, Waltham, MA) supplemented with 10% Fetal Bovine Serum. MCF 10A non-tumorigenic breast epithelial cells were cultured using the MEGM growth kit (Lonza, Walkersville, MD). HT1080 fibrosarcoma cells were cultured in DMEM media (Thermo Fisher Scientific, Waltham, MA) supplemented with 10% Fetal Bovine Serum. Hras1 thyroid cancer cells were obtained from an Hras^{G12V}/Pten KO murine thyroid tumor[147] and were cultured in F12 media (Thermo Fisher Scientific, Waltham, MA) supplemented with 10% Fetal Bovine Serum. NIH/3T3 fibroblasts were cultured in DMEM (Thermo Fisher Scientific, Waltham, MA) supplemented with 10% Fetal Calf Serum (ATCC, Manassas, VA). The BT-549, MCF 10A, HT1080, Hras1 and NIH 3T3 cultures were maintained in an incubator with CO_2 at 37 °C. To

prepare for imaging the scaffolds were first glued down to the glass bottom of 6-well dishes (MatTek Corp., Ashland, MA) using sterile high-vacuum grease (Dow Corning, Midland, MI). The scaffolds were sterilized using a 70% ethanol wash followed by two PBS rinses (Thermo Fisher Scientific). Subsequently, the fibers were coated with 4 µg/ml Fibronectin (Invitrogen, Carsbad, CA) for ~2 hours prior to cell seeding. At ~80% confluence, the cell culture was trypsinized using 0.25% Trypsin-EDTA (ATCC, Manassas, VA) and the cells were then re-suspended and diluted in culture medium. Cells were seeded with a density of ~300,000 cells/ml on the scaffolds and were allowed to attach to the fibers for ~3 hours. Finally, once cell attachment to the fibers was confirmed, each well was filled with 3 ml of media.

Oil Red O Staining: In order to prepare for Oil Red O staining, the cells on the protrusion assay were fixed in 4% paraformaldehyde for 15 minutes followed by two PBS rinses. 0.5% Oil Red O (Sigma Aldrich, St. Louis, MO) solution was prepared in ≥99.9% isopropanol. A working solution was prepared by diluting the Oil Red O solution in DI water in a 3:2 ratio. Before using the working solution, it was passed through a 0.2 µm syringe filter. 3 ml of the working solution was then added to each well of the fixed cells and kept in the wells for 15 minutes. Subsequently, the working solution was washed off by four DI water rinses.

Pharmacological Inhibitors: In order to inhibit kinesin-5 activity, 100 µm Monastrol (Millipore Sigma, St. Louis, Missouri) was used with an incubation period of 3 hours. In order to impair myosin X localization by inhibiting PIP$_3$ activity, 20 µm LY294002 (Millipore Sigma, St. Louis, Missouri) was used with an incubation period of 3 hours. In both cases, washout was performed by aspirating the media and washing the wells twice with PBS followed by addition of regular media.

Microscopy and Imaging: The cells were imaged using the AxioObserver Z.1 (with mRm camera) microscope (Carl Zeiss, Germany) at 63x (water based immersion) magnification with 1 second time imaging interval. Care was taken to ensure that only cells which were not interacting with other cells were imaged. The obtained videos were analyzed using ImageJ (National Institutes of Health, Bethesda, MD). Granules were tracked manually using ImageJ.

Statistical Analysis: Statistical analysis of the data was performed using RStudio (RStudio, Boston, MA) software. Shapiro-Wilks normality test was performed to test for the normality of the data. Analysis of variance (ANOVA) test was used to test for statistical significance between different data sets. The following symbols are used throughout the paper to represent significance levels: * <0.05, ** <0.01, and *** <0.001. If there is no comparison shown between any data sets it implies that they are not significant. All error bars represent standard error of mean.

Results:

We used the non-electrospinning Spinneret based Tunable Engineered Parameters (STEP) platform[118,119] to quantitate protrusion *coiling* behavior and the dynamics of endogenous granule transport into the protrusions as a function of *protrusive* fiber diameter at high spatiotemporal resolutions (sub-micron and 1 s). To study individual protrusions perpendicular to cell body direction, we used mismatch of fiber diameters with the *base* fiber at least 2 μm in

Figure 3.1: Morphodynamic metrics used to quantify protrusive behavior and *coiling* dynamics. (A) Schematic showing the STEP protrusion platform (large diameter *base* fibers deposited orthogonally onto smaller diameter *protrusive* fibers) along with metrics used to quantitate protrusive cycle and protrusion *coiling*. On left is data showing control on *protrusive* fiber diameter using STEP platform (n= 71, 51, 36, 30 and 40 for 135, 270, 450, 600 and 1000 nm respectively). (B) Representative transient *protrusive cycle* showing protrusion growth and retraction to cell body. (C) Representative images of protrusion *coiling* on the different fiber diameter categories studied. Left panels shows scanning electron microscopy (SEM) images of base-protrusive fiber combinations. (D) Temporal evolution of protrusion *coiling* on a 600 nm diameter fiber. (E) Schematic showing the growth of the protrusion during a *coiling* cycle. All scale bars are 5 μm.

diameter while five different *protrusive* fiber diameters (**Figure 1A**) were selected to be: 135 ± 3 nm (n = 71), 269 ± 3 nm (n = 51), 453 ± 4 nm (n = 36), 597 ± 8 nm (n = 30), and 1013 ± 19 nm (n = 40). We use two morphodynamic metrics, the protrusion length (L) and eccentricity (E), to quantitate protrusion formation, growth, and retraction to the main cell body (*protrusive cycle*) (**Figure 3.1A, B**) [129]. From optical microscopy images, acquired at 63× and 1 second interval, we

observed that the protrusion tip *coils* (wraps-around the suspended fiber axis; **Figure 3.1C**) such that a *coiling* cycle is characterized by an increase in the width of the *coil* till a maximum width is reached followed by a subsequent decrease (**Figure 3.1D, E**).

Timing of coiling is regulated by fiber diameter

To develop the framework to study details of the *coiling* behavior on fibers of varying diameters, we defined additional metrics: maximum *coil-width* occurring during one *coiling* cycle (**Figure 1E**), *coil* growth rate, and the time taken to reach maximum *coil-width*. We observed that *coiling* occurred in "spurts" at the onset of protrusion growth (**Figure 3.2A**) where the protrusion
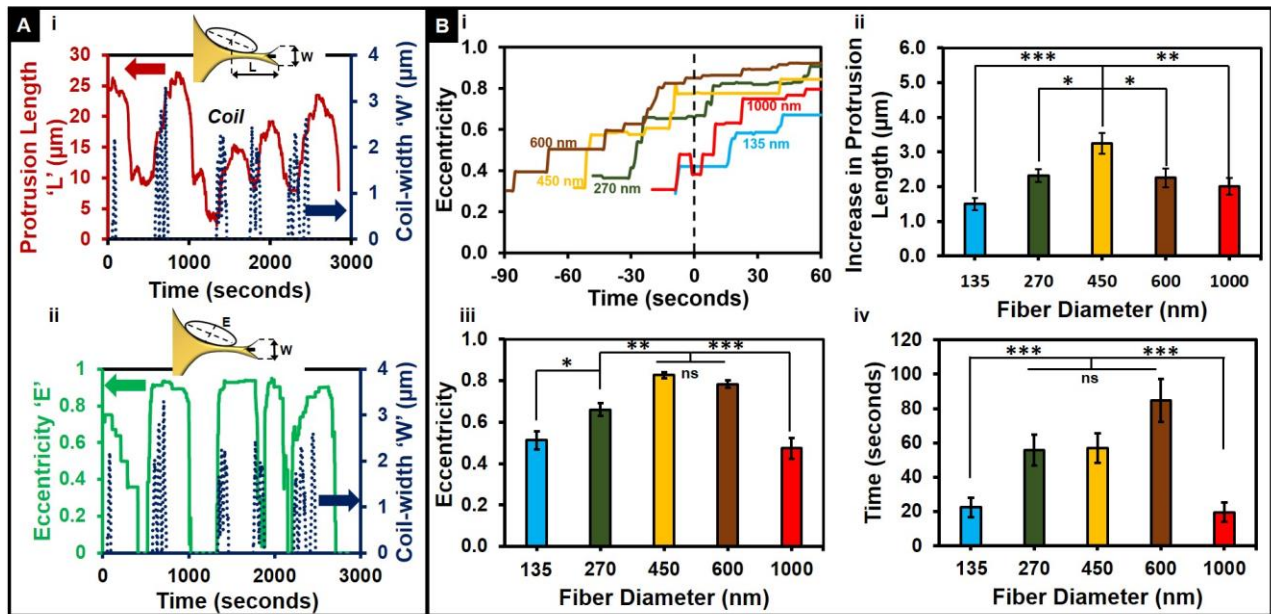
Figure 3.2: Protrusion *coiling* behavior intrinsically linked to the *protrusive cycle*. (A. i) *Coiling* behavior (blue dashed curve) occurs in bursts and takes place primarily during protrusion length increase (red curve). (A. ii) Typically, eccentricity (green curve) increase precedes *coiling* behavior. Both (A. i) and (A. ii) are representative profiles for a 450 nm diameter *protrusive fiber* case. (B. i) Representative profiles showing the temporal evolution of eccentricity, with $t = 0$ representing the onset of *coiling*. (B. ii) Increase in protrusion length during *coiling*. n = 61, 64, 81, 76 and 45 for 135, 270, 450, 600 and 1000 nm respectively. (B. iii) Average eccentricity at the initiation of protrusion *coiling* demonstrating that for the intermediate fiber diameters, a high eccentricity value is required prior to *coil* initiation. (B. iv) Time at which *coiling* occurs on fibers of different diameters demonstrating that 135 and 1000 nm diameter fibers induce faster *coiling* at lower eccentricities. $n = 21, 21, 23, 20, 20$ *for the diameters* 135, 270, 450, 600 and 1000 nm respectively. See Methods section for a discussion of the statistical significance parameters.

growth phase is quantitatively represented by a concomitant increase in both protrusion length and eccentricity (**Figure 3.2A (i, ii),** more representative profiles are included in **Supplementary Figure 3.S1**). Next, we wanted to determine the relationship between protrusion eccentricity (broadening of protrusion base) and *coiling*. Given the dynamic, fluctuating nature of protrusions, we conducted a transient analysis of the evolution of eccentricity before and after *coiling* initiation (**Figure 3.2B (i)**, with *coiling* initiation shown by t=0). We observed that for the intermediate *protrusive* fiber categories (~270 nm to ~600 nm), growth in eccentricity occurred prior to the initiation of *coiling*. However, for the fiber diameters on either end of the spectrum (~135 nm and ~1000 nm), we observed that *coiling* started independent of the broadening in the protrusion base. During the *coiling* process, protrusions were found to elongate (elongation shown schematically in **Figure 3.1E**) in a biphasic diameter dependent fashion (**Figure 3.2B (ii)**), and the protrusions continued to increase in length even after the termination of the *coiling* behavior. To quantify eccentricity-*coiling* relationship, we looked at the average eccentricity value at the initiation of *coiling* as a function of fiber diameter, and found that for the intermediate fiber diameter (~270, ~450 and ~600 nm) categories, the average eccentricity at the onset of *coiling* was at least 0.76 ± 0.02, while for the ~135 and ~1000 nm cases it averaged 0.51 ± 0.04 and 0.47 ± 0.05, respectively (**Figure 3.2B (iii)**). We quantitated the time taken to initiate *coiling* (total time taken from the initial increase in protrusion eccentricity to the initiation of *coiling*), and consistent with average eccentricity values, found that on the small and large diameter fibers it took less time to initiate *coiling* (**Figure 3.2B (iv)**). Interestingly, we did not observe significance in total length of protrusion at *coiling* initiation or the number of *coiling* events occurring in an hour (**Supplementary Figure 3.S2**). Overall, we found that the average eccentricity at *coiling* initiation

and its timing exhibited a biphasic response with increase in diameter followed by drop at ~1000 nm.

Individual Coiling Dynamics are Fiber Diameter Dependent
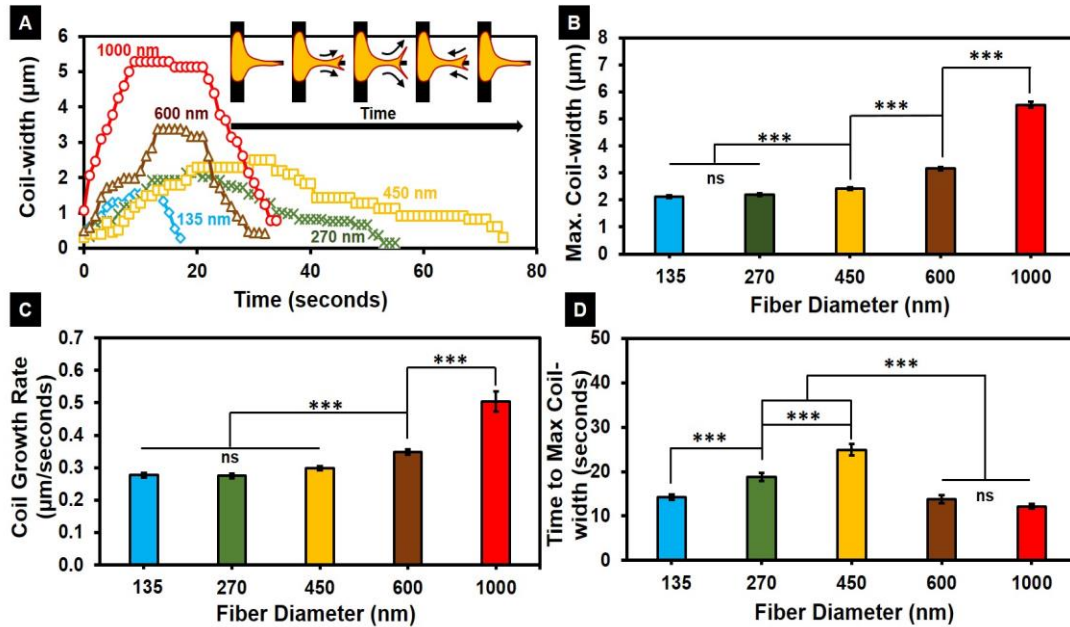
Figure 3.3: Individual *coiling* dynamics are fiber diameter dependent. (A) Representative *coiling* profiles show fiber diameter dependent dynamics of *coiling*. (B) Maximum *coil* width and (C) Average *coil* growth rate increase as a function of *protrusive fiber* diameter in a non-linear manner. (D) A biphasic relationship is observed between the time to maximum width and *protrusive fiber* diameter. In the case of all 3 parameters (maximum *coil* width, *coil* growth rate, and time to maximum width), n values are as follows: 135 nm – 117, 270 nm – 75, 450 nm – 113, 600 nm – 111, 1000 nm – 77. See Methods section for a discussion of the statistical significance parameters.

Having quantitated the interplay between increase in protrusion length during *coiling*, eccentricity and *coiling* initiation, we next wanted to analyze the kinetics of *coil* growth. Observing *coiling* profiles on different fiber diameters (representative profiles in **Figure 3A**), we found that the maximum width of the *coil*, the rate at which the *coil* grows, and the time taken to reach the maximum width are regulated by fiber diameter. For both maximum width and the growth rate, we observed no significant differences between the two smallest diameter categories (~135 nm and ~270 nm). However, with further increase in diameter, we found both parameters to increase

in a non-linear manner (**Figure 3.3B, C**), whereas the time taken to reach the maximum width displayed a biphasic relationship (**Figure 3.3D**). Combined with our findings in **Figure 3.2**, we conclude that ~1000 nm diameter fibers support widest *coils* that initiate independent of protrusion broadening, and do so at the fastest *coil* growth rate.

Granule translocation occurs in a fiber diameter dependent manner and coincides with both the protrusion growth and coiling cycle

In conjunction with the protrusions *coiling*, we observed that individual granules entered the protrusions persistently at high speeds (**Figure 3.4A**). The granule translocation dynamics showed a near-stationary particle exhibiting fast travel through the protrusion and coming to a near-stationary state again within the protrusion. Thus, we inquired if their translocation correlated with the kinetics of *coiling*.

Near-stationary granules (likely lipid particles, **Supplementary Figure 3.S3**) acting as endogenous 'tracer particles' were observed to enter the protrusion during the growth phase of the *protrusive cycle* in ~ 80% of the cases with the remaining particles translocating either in a non-growing protrusion or, rarely, in a retracting protrusion (**Supplementary Figure 3.S4**). Of the cases of particle translocation during the protrusion growth phase, we found that 69% of them coincided with the *coiling cycle* (**Supplementary Figure 3.S5**). Thus, we inquired if the granule dynamics were being regulated by the fiber diameter. In order to quantitate the dynamics of granules entering the protrusion, we analyzed granule speed and persistence (defined as the ratio of the displacement of the granule to the distance covered by the granule during its journey through the protrusion). We found that for granules entering a protrusion, the speed and persistence both increased with fiber diameter (**Figures 3.4B (ii, iii)**). Granule speeds of up to 1.3 ± 0.2 μm/s at high persistence of 0.89 ± 0.03 were achieved for the ~1000 nm *protrusive* fiber diameters

representing a ~2.3 times increase over the speed (0.57 ± 0.06 μm/s) and a ~1.5 times increase

over the persistence (0.58 ± 0.03) recorded for the ~135-450 nm *protrusive* fiber diameter cases

combined. Interestingly, in cases where multiple granules entered the same protrusion at different
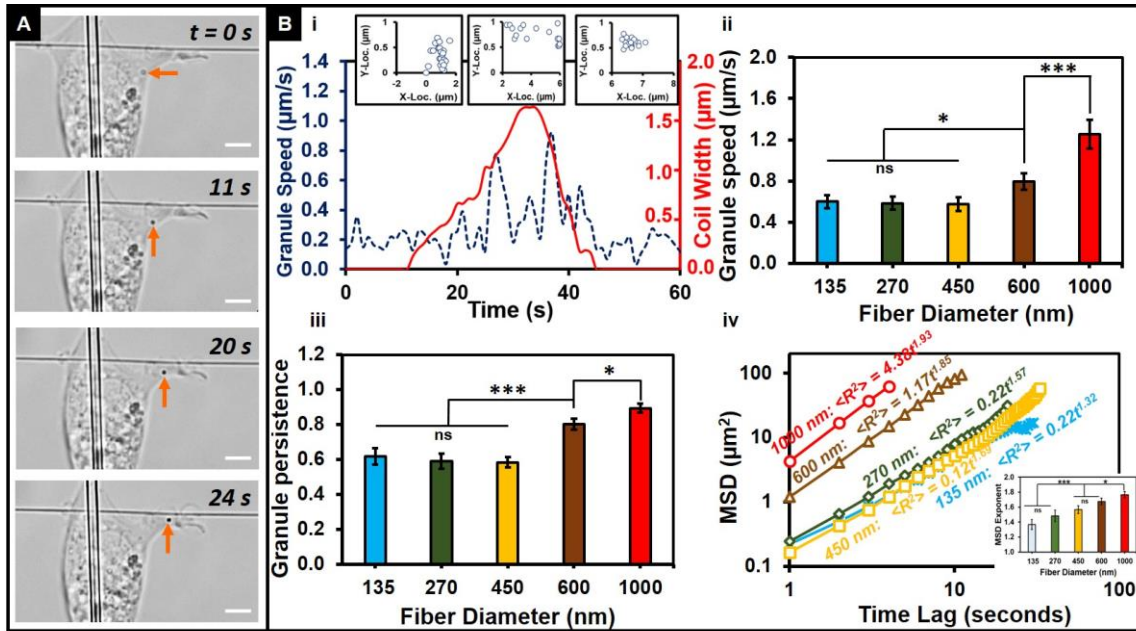
Figure 3.4: Dynamics of granules entering protrusions (A) Representative time-lapse images of a single granule (shown by orange arrow) entering a protrusion. Scale bar is 5 μm. (B) (i) Representative transient profile showing granule speed (dashed blue line) increases with *coil-width* (solid red line). Inset plots of granule position show near-stationary granules translocate persistently at high speeds during *coiling* cycle, following which they become near-stationary again. (ii, iii) Speed and persistence of the granules increase with increasing *protrusive* fiber diameter. (iv) Representative MSD vs time profiles and their calculated MSD for granules on different *protrusive* fiber diameters show that on all tested diameters, the granules enter the protrusions in a superdiffusive manner (exponent of the scaling law fit >1). Inset, MSD exponent as a function of *protrusive* fiber diameter shows an increase (on average) with increasing diameter. n values are as follows: 135 nm – 19, 270 nm – 17, 450 nm – 12, 600 nm – 21, 1000 nm – 20. See Methods section for a discussion of the statistical significance parameters.

times, we observed them to follow a narrow spatial set of paths analogous to *highways*

(**Supplementary Figure 3.S6** shows representative cases on different fiber diameters).

Since granules were translocating at high speeds in a persistent fashion into the protrusions,

we inquired if the process of translocating could be described by mean square displacement (MSD)

method used commonly to describe intracellular granule transport.[148,149] Endogenous granule translocation studied using MSD analysis has been previously shown to range from subdiffusion to superdiffusion regimes indicating random to ballistic transport, respectively. [150–155] The MSD for random diffusion of a particle through an unobstructed medium in "d" dimensions is given by $<R^2> = 2dDt$ where "R" represents the MSD, "D" is the diffusion coefficient and "t" is the lag time.[150] However, given the densely packed nature of the cell cytoplasm and the presence of molecular motors to assist cargo transport, intracellular transport is better characterized by anomalous diffusion exhibiting a non-linear power-law behavior $<R^2> = 2dDt^{\alpha}$ where $\alpha = 1$ reverts back to the standard diffusion case.[154,156] For $\alpha<1$, the translocation is termed as subdiffusive, whereas for $\alpha>1$ the translocation is termed as superdiffusive, and values of $\alpha \sim 2$ represent "ballistic" motion. Our analysis (**Figure 3.4B (iv)**) shows that translocation of granules within protrusions occurs in a superdiffusive manner across all the fiber diameter categories studied, and approaches a near-ballistic transport process occurring in protrusions on ~1000 nm diameter fibers.

Finally, given the superdiffusive nature of the granule dynamics, we investigated if molecular motors might play a potential role in the transport of granules in the protrusions. Previously, we have shown that the localization of cytoskeletal components inside individual protrusions is dictated by the protrusion morphology[129]. Specifically, while f-actin and microtubules are present in protrusions of all sizes, the intermediate filament vimentin localized only in mature protrusions (eccentricity ~0.8 and higher). Thus, we investigated the effect of pharmacological inhibitors Monastrol (100 µM) to inhibit kinesin-5 (a microtubule associated motor protein) and LY249002 (20 µM) to hinder localization of myosin X (an actin filament associated motor protein) to the cell leading edge by inhibiting phosphatidylinositol (3,4,5)-trisphosphate (PIP_3) activity (PIP_3 plays a critical role in myosin X recruitment). In both cases

(representative cells treated with both drugs shown in **Supplementary Figure 3.S7**), we observed a change in the protrusive behavior highlighted by an increase in the proportion of relatively short protrusions (<5 μm in length compared to the average protrusion length of 19 μm ± 0.3 μm; **Supplementary Figure 3.S8**). In both cases, washing the drug out recovered the original protrusive behavior. Intriguingly, we found that in both drug cases, there was also a decrease in the proportion of protrusions in which a granule translocation was observed. Analysis of the granule dynamics showed that speed and persistence were unaffected in case of the Monastrol addition, whereas a significant decrease in both speed and persistence was observed with addition of LY249002. Washing out the drugs resulted in recovery of original speed and persistence in both cases. Combined, these results suggest that while both kinesin-5 and myosin X motor reduce the instances of granule translocation, myosin X significantly impacts the dynamics of granule translocation.

Discussion:

Native fibrous environment surrounding the breast tumor is a complex architecture of fibers of varying diameters, spacing, and orientations (schematic **Figure 3.5A**), that collectively make up for pro and anti-invasive biophysical conditions. Invasion along fibers from the edge of the tumor requires cells to first biophysically sense fibers through formation of rod like protrusions that can mature into broad structures in a fiber diameter dependent manner.[129] In our study, we quantitate at single protrusion resolution, the biophysical probing/recognition of curvature of fibers over a wide range of fiber diameters mimicking the surrounding fibrous environment at the tumor periphery (shown by dashed oval in **Figure 3.5A**). We show that fiber diameter regulates the dynamics of the protrusion *coiling* (size, rate and time of occurrence). Our findings show that for intermediate diameter fibers (~270 nm – 600 nm), an increase in eccentricity precedes *coiling*

initiation whereas for the two ends of the diameter spectrum tested (~135 nm and ~1000 nm) *coiling* occurs independent of protrusion widening (increase in eccentricity, **Figure 3.2**). However, the *coil-width* and its rate of increase positively correlate with diameter (**Figure 3.3**). The similarities in time taken to reach maximum *coiling* width observed across fibers on either end of tested diameters can be explained by minimal adhesion-driven contractility on high curvature 135 nm diameter fibers, and conversely low curvature 1000 nm diameter fibers providing adequate surface area for adhesion sites to mature and increase in number. Indeed, supporting this hypothesis are our previous findings that show cells attached to (i) small diameter nanoscale fibers are unable to spread and remain rounded while actively probing the fiber curvature [129] and (ii) large diameter fibers have increased spatial distribution of focal adhesion sites resulting in larger forces.[157] However, the adhesion-based contractility on intermediate fiber diameters remains unclear as the time to reach maximum *coil-width* peaks at 450 nm diameter (transient profiles in **Figure 3.3A** and data in **Figure 3.3D**). Interestingly, substituting single larger diameter fibers with a bundle of smaller diameter fibers recovers *coil-width* dynamics on larger diameter fibers (**Figure 3.5B**), thus suggesting the role of both mechanical properties and available surface area in biophysical sensing. To determine if *coiling* was also exhibited by another breast cancer cell line, we repeated the study with a highly metastatic cancer line BT-549 (**Supplementary Figure 3.S9**). Our data shows similarities in *coiling* dynamics between the two metastatic cancer cell lines.

After extending protrusions to sense the fibrous environment at the tumor interface, breast cancer cells can detach from the primary tumor and begin migrating along linearized collagen fibers towards the circulatory system for subsequent dissemination to secondary sites[158]. Given that protrusion tip *coiling* is observed during protrusion extension, we further enquired if *coiling*

also occurred during bulk cell body migration on aligned, single suspended fibers (**Figure 3.5C**)
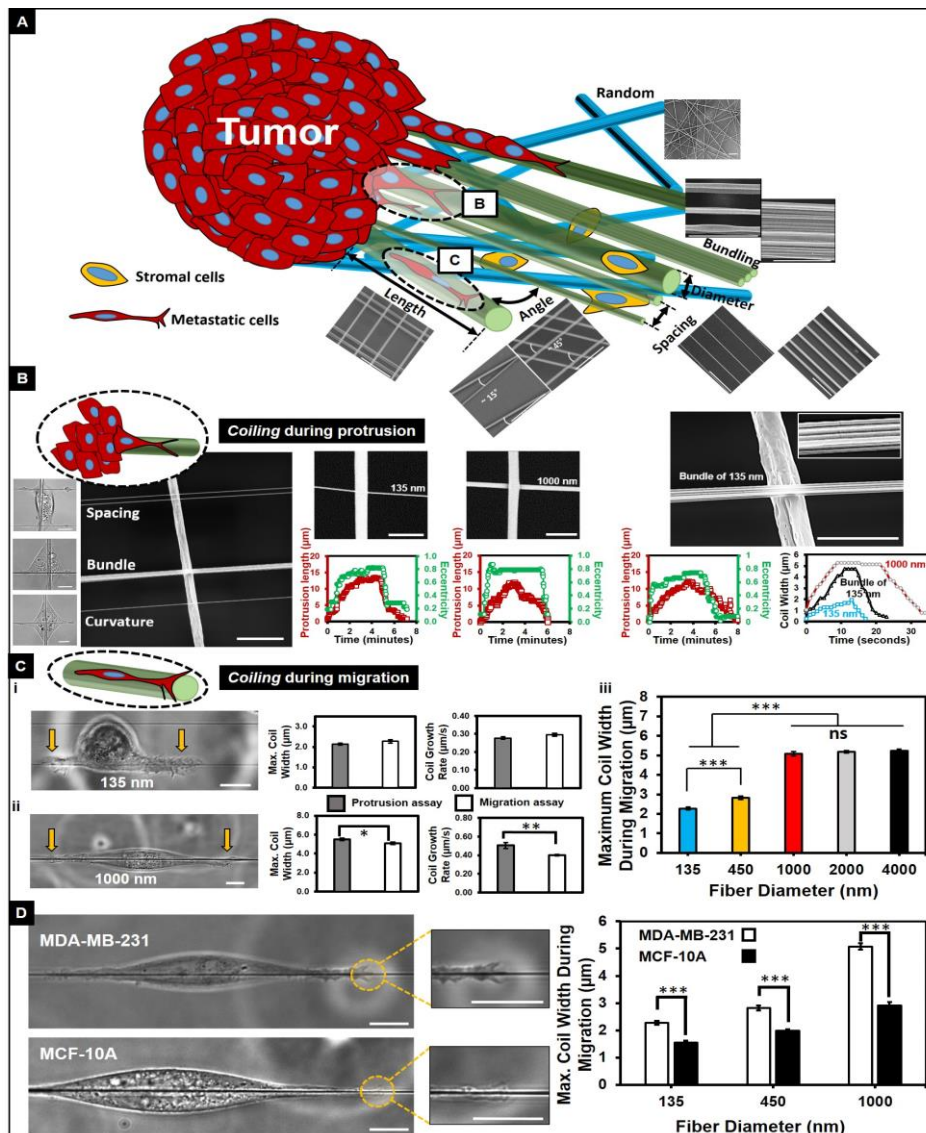
Figure 3.5: *Coiling* **in recapitulated** *in vivo* **environments.** (A) Schematic showing the heterogeneity observed in environments neighboring breast tumors. Fibers of varied diameters, lengths, orientations and architectures are interfaced with stromal cells that combined together induce pro and anti-invasive cell behavior. Inset shows SEM images of fibers deposited in varying configurations[119] that mimic the native environments including random and aligned configurations. All scale bars are 10 µm (B) Cell migration starts with first cells sensing the native environments. Biophysical sensing of fibers can be studied by providing controlled and repeatable fiber architectures (spacing, bundles and individual fibers of varying curvature). On left are representative phase images of cells on controlled fiber networks (scale bars: 10 µm). Bundling of small diameter fibers can recover *coil-width* kinetics as that of a single large diameter. (C) *Coiling* during cell migration along fibers. Representative images showing "balled-up" cell morphology during migration on (i) 135 nm diameter fiber and elongated,

33

"spindle" morphology during migration on (ii) ~1000 nm diameter fiber. Scale bars are 5 μm. Yellow arrows show simultaneous *coiling* on both sides of the cell. Comparison between *coiling* dynamics on a protrusion assay and migration assay for ~135 nm diameter and ~1000 nm diameter fiber cases. Sample size for the protrusion assay are as follows: 135 nm – 117, 1000 nm – 77, and for the migration assay are: 135 nm – 65, 1000 nm – 63. (iii) Maximum *coil* width during migration as a function of the fiber diameter. Sample size is as follows: 135 nm – 65, 450 nm – 50, 1000 nm – 63, 2000 nm – 61, 4000 nm – 66. (D) Representative phase images of *coiling* dynamics exhibited by non-metastatic MCF-10A and metastatic MDA-MB-231 show diminished *coiling* in non-metastatic cell lines. Scale bar 10 μm. Sample size for MDA-MB-231 is as follows: 135 nm – 65, 450 nm – 50, 1000 nm – 63. Sample size for MCF 10A is as follows: 135 nm – 23, 450 nm – 36, 1000 nm – 20.

of different diameters ranging from ~135 nm to ~4000 nm (hereafter referred to as "migration assay"). On the smallest diameter tested (~135 nm), cell spreading was hindered as evidenced by

frequent "balling-up" of the cell and blebbing. In contrast, on relatively larger diameters (~450 nm and higher) tested, cells adopted a spread "spindle" morphology (**Figure 3.5C (i, ii)**). Spindle cells on larger diameter fibers, had reduced blebbing consistent with our previous findings that cell blebbing inversely correlates with cell spread area[23]. Interestingly, cells displayed *coiling* to occur at both ends of the cell body on the ~135 and ~1000 nm diameter fibers (**Figure 3.5C (i, ii)** shown by yellow arrows), thus suggesting concurrent sensing at opposite poles of rounded and stretched cells. Next, we quantified the dynamics of *coiling* at the tip of cells in-line with direction of migration and compared them to *coiling* quantitated on the protrusion assay (perpendicular to the direction of migration) on ~135, ~450 and ~1000 nm diameter fibers. We found that the *coiling* behavior followed the trends obtained using protrusion assay, whereby the width and rate of *coiling* increases in a diameter dependent manner, and the *coiling* cycle time is the slowest for ~450 nm diameter fibers (**Supplementary Figure 3.S10**). Interestingly, we found that on ~1000 nm diameter fibers that favor cells to form elongated spindle shapes, *coils* were significantly smaller in widths and grew at slower rates compared to the protrusion assay (**Figure 3.5C (i,ii)**).

Furthermore, the maximum *coil* width in-line with migration direction did not change on subsequent larger diameters (~2000 and ~4000 nm, **Figure 3.5C (iii)**). Overall, the similarity in *coiling* on high curvature fibers (~135 and ~450 nm) and differential response on low curvature fibers (~1000 nm and above) suggests a possible biophysical adaptation from a sensory to a deterministic migratory response with increase in diameter. How these two responses are utilized by cells to establish adhesion based contractile machinery in single protrusions or at the two poles of a rounded or stretched cell where *coiling* occurs concurrently remains unclear.

Breast cancer has a well-known predilection for metastasizing to the bone[159,160]. Following the attachment of previously circulating breast cancer cells to the vascular endothelia of the bone, their subsequent extravasation into the bone marrow compartment is promoted by bone and marrow derived chemotactic factors[161]. On entering the bone marrow, cancer cells encounter a complex array of stromal cells and growth factors embedded in a highly mineralized extracellular matrix which provide a combination of biophysical and biochemical cues that assist in the colonization of the bone[161–163]. While the role played by the biochemical cues has been investigated in detail, the influence of the mineralization of the collagen fibers unique to the bone, is still unclear. A recent study has shown that MDA-MB-231 breast cancer cells exhibited more rounded morphology on mineralized collagen fibers compared to non-mineralized fibers[164]. It is unclear if cancer cells could be employing *coiling* as a physical mechanism to aid invasion. Thus, we were intrigued if non-metastatic breast cells also displayed *coiling* on fibers of various diameters. Interestingly, we found that not only did non-metastatic cancer cells (MCF 10A) exhibit *coiling* in only ~50% of the cases, but also the *coiling* was diminished compared to their metastatic counterpart (**Figure 3.5D**). Guided by the *coiling* behavior observed in the breast model, we inquired if *coiling* was observed in other cell types, and found other cancer models (fibrosarcoma

HT1080 and thyroid Hras1) along with migratory NIH 3T3 fibroblasts to also exhibit *coiling*. Collectively, our data demonstrates that migratory cells advance on fibers by *coiling,* and the extent of *coiling* is regulated by fiber curvature. However, how *coiling* is utilized in pro- and anti-migratory environments remains unknown.

Summary:

In conclusion, using the non-electrospinning STEP platform, we quantitate the biophysical sensing of fibers through *coiling* by cancer cells. We envision that future studies capable of integrating biophysical quantitation presented in this manuscript with membrane tension, curvature sensing F-BAR proteins, family of GTPases, and integrin-driven establishment of contractility will link the biophysical *coiling* with biological timing and signaling. Additionally, by increasing the complexity of the fibrous environment in a repeatable manner, the investigation of cell morphology (elongated cells on single or multiple fibers [165]) driven *coiling* dynamics could help elucidate the potential role of morphology in cancer cell invasion. Through these future studies, we aim to quantitatively describe the migratory cell decision steps in pro and anti-invasive fibrous environments.
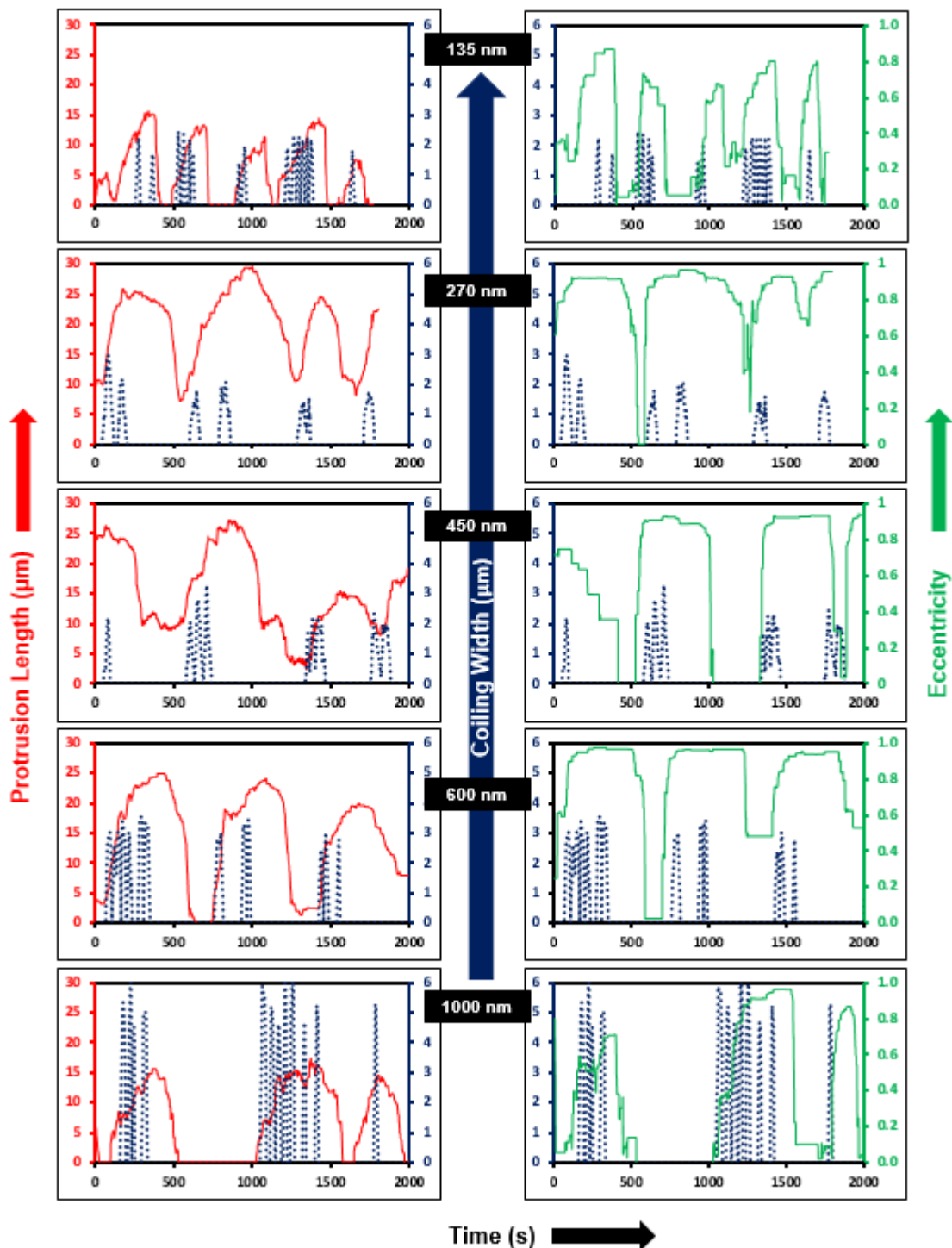
Supplementary Figure 3.S1. Representative protrusive profiles for the different *protrusive fiber* **diameters studied.** The mechanism of *coiling* behavior occurring in spurts during the protrusion growth is conserved across fiber diameters. Each row of plots is for the same fiber diameter.
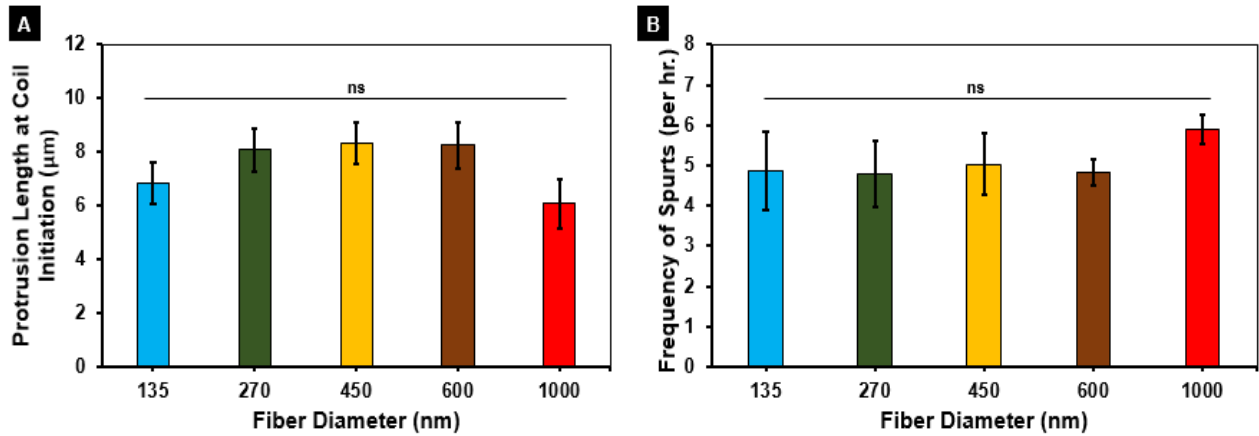
Supplementary Figure 3.S2: Average protrusion length at the initiation of coiling and subsequent *coiling* **frequency as a function of fiber diameter.** Both the (A) average protrusion length at the onset of *coiling* and (B) frequency of *coiling* spurts are independent of fiber diameter. n values for (A) are as follows: 135 nm – 20, 270 nm – 21, 450 nm – 23, 600 nm – 20, 1000 nm – 20. n values for (B) are 10 for each fiber diameter. See Methods section for a discussion of the statistical significance parameters.
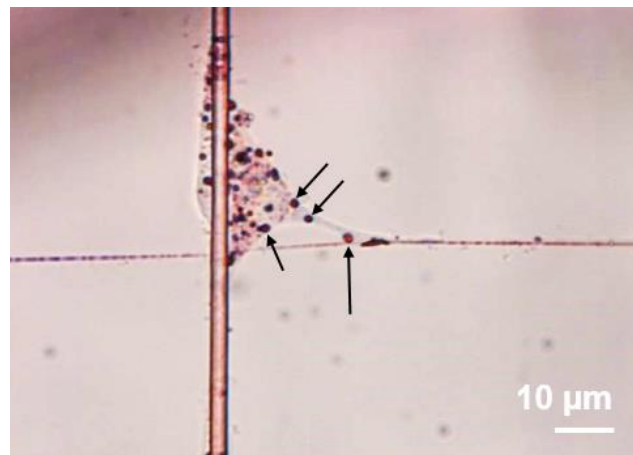
Supplementary Figure 3.S3: Oil Red O Staining Image. Representative cell after Oil Red O staining
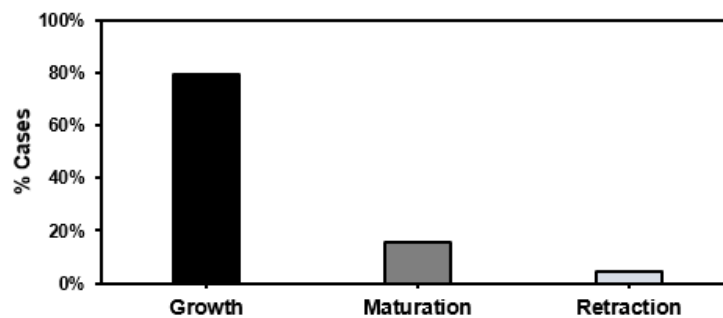
Supplementary Figure 3.S4: Linking granule transport to the protrusive cycle. % of total granule transport cases which occurred during the different stages of the *protrusive cycle*. n = 89 granules.
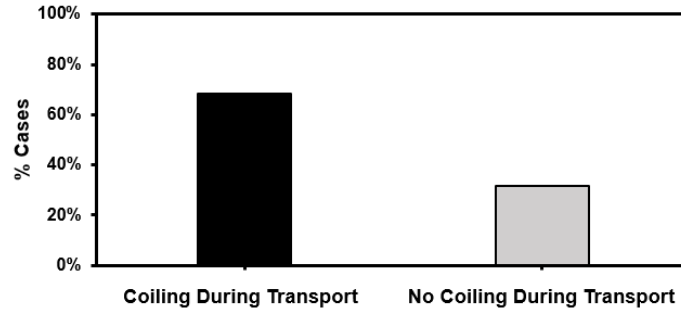
Supplementary Figure 3.S5: Linking granule transport to the coiling cycle. Percentage of total granule transport cases during protrusion growth which coincide with tip *coiling*. n = 71
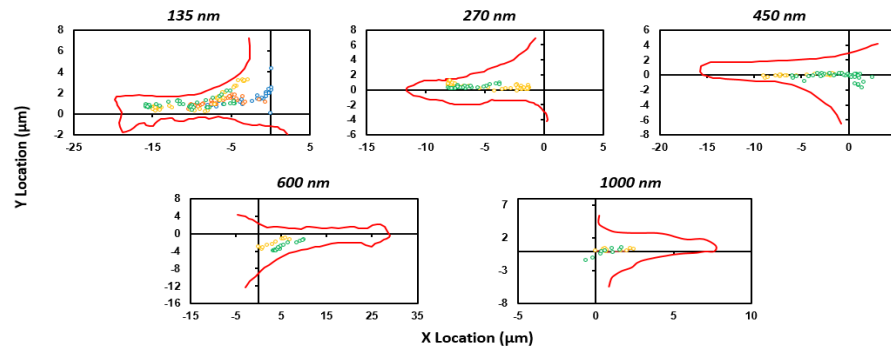
Supplementary Figure 3.S6: Representative profiles showing that granules enter protrusions along a tightly defined set of routes. Representative protrusion profiles (in red) and granule trajectories (circles) for the different fiber diameters are shown.
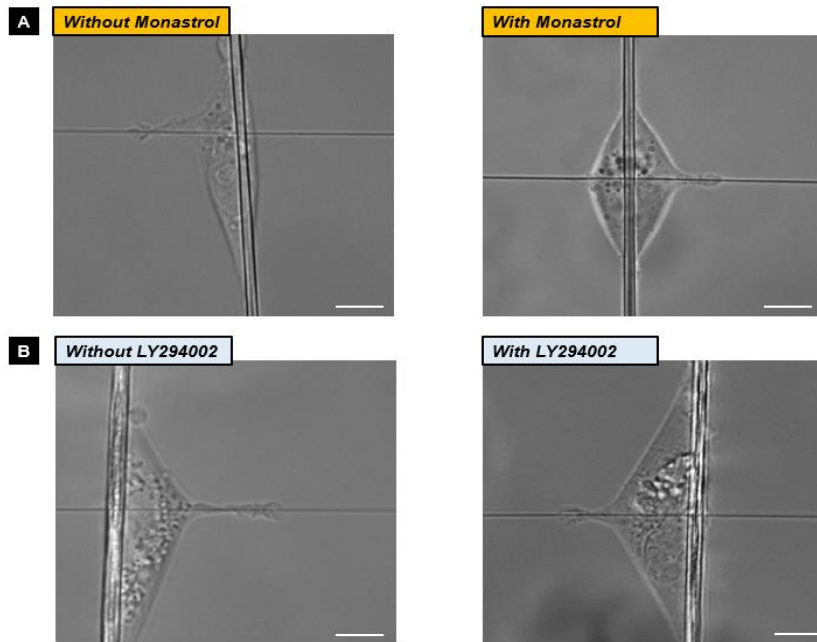
Supplementary Figure 3.S7: Representative images of MDA-MB-231 cells before and after drug treatment. (A) Treatment with 100 µm Monastrol and (B) Treatment with 20 µm LY294002.
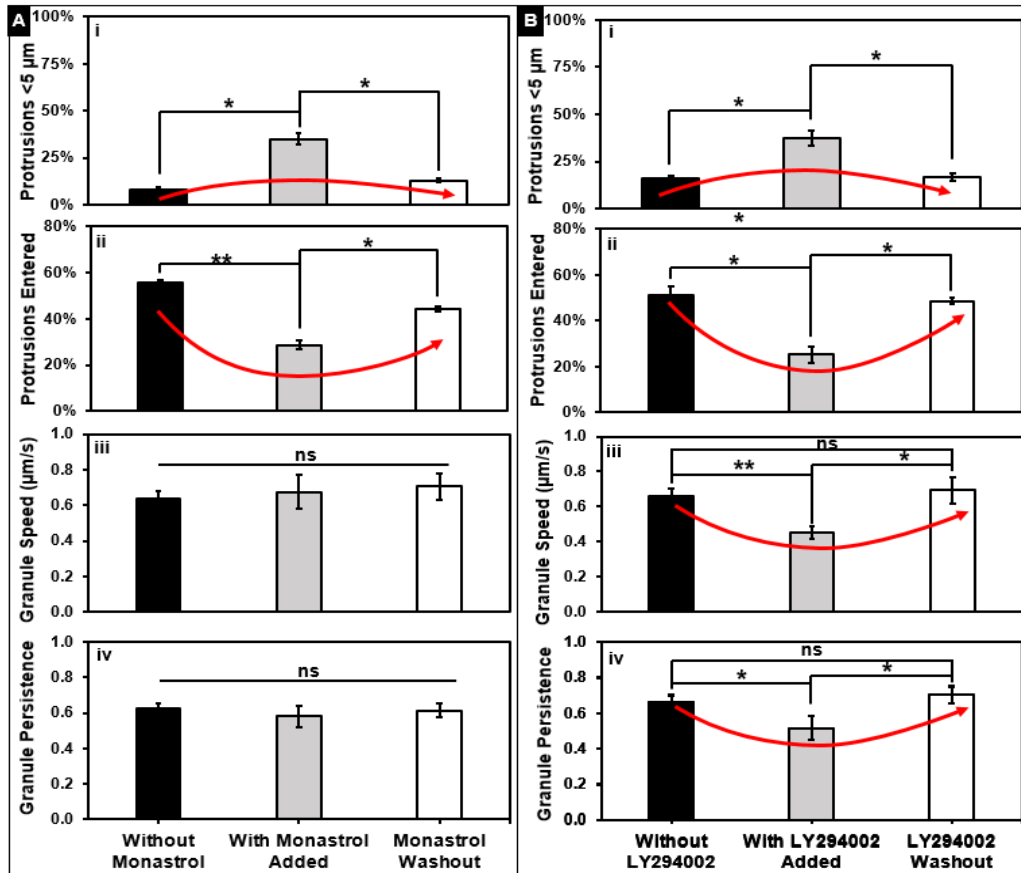
Supplementary Figure 3.S8: Pharmacological inhibition of cytoskeletal motors. Here panel (A) represents the results using Monastrol while panel (B) represents the results using LY294002. In both cases, we recorded (i) the percentage of protrusions lower than 5 μm in length, (ii) the percentage of protrusions in which granule translocation was observed, (iii) granule speed and (iv) granule persistence for the control case (without drugs added), with the drug added and finally, after drug washout. n values for the Monastrol study are as follows: 64, 43, and 70 protrusions recorded for the without Monastrol, with Monastrol and Monastrol washout cases respectively. 33, 8, and 27 granule translocation cases observed in the without Monastrol, with Monastrol and washout cases respectively. n values for the LY294002 study are as follows: 55, 60, and 52 protrusions recorded for the without LY294002, with LY294002 and washout cases respectively. 24, 9 and 21 granule translocation cases observed in the without LY294002, with LY294002 and washout cases respectively. For the % protrusions entered, only the protrusions >5 μm were considered. See Methods section for a discussion of the statistical significance parameters.
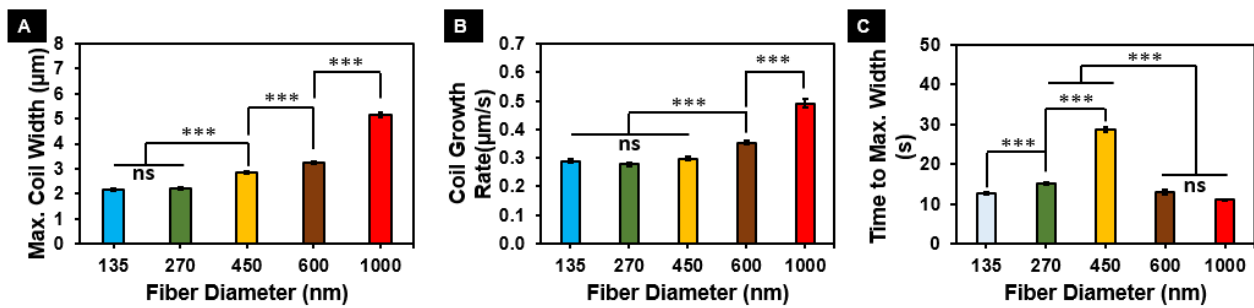
Supplementary Figure 3.S9: Quantifying *coiling* dynamics for BT-549 cells. (A) Maximum *coil* width, (B) *Coil* growth rate and (C) Time to maximum *coil* width as a function of fiber diameter. n values are as follows: 135 nm – 65, 270 nm – 63, 450 nm – 61, 600 nm – 61, 1000 nm – 60.
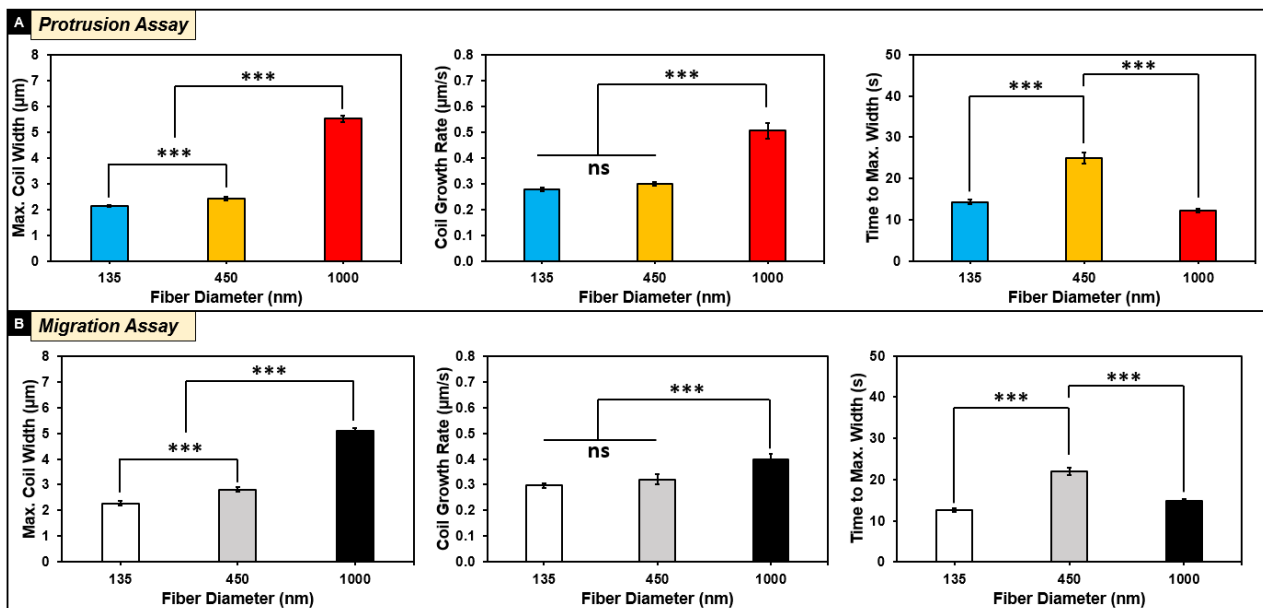
Supplementary Figure 3.S10: *Coiling* dynamics on both protrusion and migration assays exhibit the same trend. Quantification of *coiling* dynamics for MDA-MB-231 cells on (A) protrusion assay and (B) migration assay as a function of fiber diameter. n values for the protrusion assay are: ~135 nm – 117, ~450 nm – 113, and ~1000 nm – 77. n values for the migration assay are: ~135 nm – 65, ~450 nm – 50, and ~1000 nm – 63.

Chapter 4: Quantitative Biophysical Metrics for Rapid Evaluation of Ovarian Cancer Progression

Introduction:

Ovarian cancer is the fifth leading cause of cancer-related deaths in women. It presents the highest mortality rate of any other gynecological cancer, with ~54% of patients dying from the initial or recurrent diagnosis [16,166]. Due to the lack of early detection capabilities, only ~30% of patients are diagnosed when the cancer is limited to the ovaries (Stage I), presenting the highest chance of cure [167,168]. The chances of survival reduce dramatically with ovarian cancer progression, including metastasis to the pelvic organs (Stage II), the peritoneal organs (Stage III), or beyond the peritoneal cavity (Stage IV) [169,170]. Despite recent developments in early-stage screening and diagnostic technologies for other types of cancer, the diagnostic tools for ovarian cancer remain primarily limited to biannual pelvic examinations, transvaginal ultrasounds, or cancer antigen (CA) 125 blood tests [171–175]. Furthermore, the diagnostic tools of ovarian cancer may not be able to detect early stages of the disease, distinguish between disease stages and metastatic potential, or are not routinely performed. Genetic profiling of biopsies, circulating tumor cells or bodily fluids are used to screen for specific mutations or secreted proteins, however, often the genetic or protein markers are only applicable to a subset of patients due to the inherent heterogeneity of tumors[176], or do not include epigenetic changes, miRNA, circular RNA, exosomes or stimuli from other cells in the tumor microenvironment that all can contribute to disease progression[177]. Thus, there exists a currently unmet critical need for the development of diagnostic tools that can determine the disease stage in a timely and reliable manner and consequently improve the likelihood of patient recovery.

The metastatic cascade in ovarian cancer progression begins with the exfoliation of the cancer cells from the primary site, such as the ovary or the fallopian tubes [178]. Subsequently, the cancer cells are circulated in the peritoneal cavity by the peritoneal serous fluid or ascites flow and adhere to secondary sites such as the omentum and other peritoneal organs, including the liver, diaphragm, and intestines that are lined with a protective layer of mesothelial cells [16,179,180]. The adherent ovarian cancer cells then begin invading through the mesothelial cell monolayers into the sub-mesothelial connective tissue stroma, which is a fibrous network predominantly composed of collagen fibers [181]. Invasion of the ovarian cancer cells through the mesothelial monolayer occurs by either pushing the mesothelial cells aside by exerting physical forces [182,183], by cleaving the mesothelial monolayer via matrix metalloproteinases [184,185], or by apoptosis [186], thus, creating a pathway to the underlying fibrous ECM.

Cell invasion is a highly orchestrated sequence of events that is initiated with the extension of protrusions from the main cell body first to sense the surrounding fibrous environment and establish polarity [187]. Subsequently, cells can form integrin-mediated stable focal adhesions necessary to generate actomyosin contractility-based forces [188,189] and invade through the sub-mesothelial ECM [190–192]. Not surprisingly, a combination of *in vitro* and *in vivo* studies have thus explored the potential of characterizing protrusion dynamics, migration, and force transmission by cancer cells as alternative biophysical indicators of their metastatic potential complementary to genetic modifications [41,72,74,193–196]. Biophysical metrics have been used to characterize a variety of cells including breast cancer [197], liver cancer [198], brain cancer [198], chondrosarcoma [199] and fibroblasts [200], using a range of technologies that include magnetic resonance elastography, ultrasound elastography, cell-based sensors, atomic force microscopy, optical tweezers, and microfluidic platforms[201]. However, most of the *in vitro* measurements are performed on flat, 2D

surfaces that only partially recapitulate the complex, fibrous architecture of the sub-mesothelial ECM. Three-dimensional gels are more analogous to the *in vivo* environments, but their inherent spatial heterogeneity can hinder the quantitation of biophysical metrics as metastatic indicators in a repeatable manner.

In this study, we used the non-electrospinning, spinneret-based tunable engineered parameters (STEP [119,202,203]) platform to construct controlled and suspended nanofiber networks that mimic fibrous features of the sub-mesothelial ECM[204,205]. We utilized multiple fibrous architectures to inquire if protrusions, migration, and forces can be used as markers of metastatic potential in our previously reported mouse ovarian surface epithelial (MOSE) cell model [206–208] which allows us to eliminate the inter-individual differences that are inherently associated with using cells from different patient samples or origin sites. The MOSE model is representative of the disease progression from early to late stages of human serous ovarian cancer and comprises of the benign MOSE-E, the tumorigenic, slow-developing disease MOSE-L (lethal disease achieved in ~100 days after injection of 1×10^6 cells), and the tumorigenic, fast-developing disease representing MOSE-L$_{TICv}$ cell lines (lethal disease achieved in 23 days after injection of 1×10^4 cells). Furthermore, since the MOSE lines express fallopian tube markers they likely represent serous ovarian cancer that can originate from the fallopian tubes and thus, we used the human syngeneic benign (FNE) and malignant (FNLE) fallopian tube cell lines to confirm our data in a human model [209]. Our high throughput biophysical measurements using both the MOSE model and the human syngeneic pairwise cells, all capable of being quantified in a matter of few hours, quantitate biophysical sensitivity to disease progression, thus providing both new and complementary investigative tools for early diagnosis of ovarian cancer.

Methods:

Fiber Network Manufacturing Using the STEP Platform: The previously reported non-electrospinning Spinneret based Tunable Engineered Parameters (STEP) method [118] was used to fabricate the suspended fiber scaffolds used in this study (Figure 1). Briefly, polystyrene (PS, Scientific Polymer Products, Ontario, NY) of $\sim 2 \times 10^6$ g/mol molecular weight was dissolved in a 1:1 xylene:dimethylformamide (Fischer Scientific, Pittsburgh, PA) solution at 10% (w/w) concentration to prepare the polymer solution for spinning the ~ 2 μm base fibers for both the protrusion and force studies. To spin the ~ 500 nm diameter fibers for the migration and protrusion studies a 10% (w/w) concentration solution of $\sim 2 \times 10^6$ g/mol molecular weight polystyrene dissolved in xylene was used. Finally, to spin the ~ 220 nm diameter fibers for the force studies, a 7% (w/w) concentration solution of $\sim 2 \times 10^6$ g/mol molecular weight polystyrene dissolved in xylene was used. The solutions were prepared at least 2 weeks prior to spinning the fibers.

Scanning Electron Microscopy: Environmental Scanning Electron Microscope (ESEM) was used to take images of the suspended fibers in order to confirm the fiber diameter. Prior to imaging the scaffolds, they were coated with a 7 nm thick layer of Platinum-Palladium using a Leica sputter coater (Leica, Wetzlar, Germany). The images were taken at an electron beam voltage of 10 kV and a spot size of 3.5 using the ETD detector. The working distance was maintained at ~ 11 mm. Appropriate magnification was used depending on the application.

Cell Culture: Mouse ovarian surface epithelial (MOSE) cell lines representing benign (MOSE-E), slow-developing (MOSE-L), and fast-developing disease (MOSE-L$_{TICv}$) of ovarian cancer generated from C57BL/6 mice have been extensively characterized previously [206,207,210,211]. MOSE cells were cultured in high glucose DMEM (Sigma Aldrich) supplemented with 4% fetal bovine serum (Atlanta Biological), 3.7 g/l sodium bicarbonate, 10 ml/l of penicillin-streptomycin solution

with a pH of 7.4 at 37°C in 5% CO_2 in humidified conditions. The human syngeneic benign (FNE) and malignant (FNLE) fallopian tube cell lines were both obtained from the Miami Sylvester Comprehensive Cancer Center. These cells were cultured in Primaria tissue culture flasks (Becton Dickinson) with FOMI medium (Sylvester Cancer Center) supplemented with 25ng/ml cholera toxin (Sigma) as described [209].

Cell Seeding and Experiment: To prepare for the experiments, the scaffolds were first fixed to glass bottom of 6-well dishes (MatTek Corp., Ashland, MA) using sterile, high-vacuum grease (Dow Corning, Midland, MI). Next, each well was filled with 2 ml of 70% ethanol in order to disinfect the scaffolds followed by two phosphate buffered saline (PBS) rinses (Thermo Fisher Scientific). Subsequently, the fibers were coated with 4 µg/ml Fibronectin (Invitrogen, Carsbad, CA) for 2 hours prior to cell seeding to aid cell attachment to the fibers. Once the cell culture reached ~80% confluency, 0.25% Trypsin (ATCC, Manassas, VA) was added and the culture was incubated for ~ 1 minute. Following the incubation, 5 ml of fresh cell media was added to dilute the effect of the trypsin. Finally, cells were seeded at a density of ~300,000 cells/ml on the scaffolds and were allowed to attach to the fibers for ~ 3 hours. Once the cells had attached to the fibers, 3 ml of media was added to each well.

Microscopy and Imaging: The cells were imaged using the AxioObserver Z.1 (with mRm camera) microscope (Carl Zeiss, Germany) at 20× magnification for the protrusion, migration, and force studies and at 63× (water immersion objective) magnification for the *coiling* studies. The cells were imaged at intervals of four minutes for the migration studies, three minutes for the force studies, two minutes for the protrusion studies, and one second for the *coiling* studies. All the videos were analyzed using ImageJ (National Institutes of Health, Bethesda, MD).

Analysis of Biophysical Metrics: For the protrusion analysis, the maximum protrusion length was calculated as previously described [129]. Briefly, first the distance from the base fiber to the protrusion tip was measured (L_b). Next, the largest possible ellipse was fit along the curvature of the protrusion such that one end of the ellipse was located on the protrusion at a distance of $0.8 \times$ L_b from the base fiber. Finally, the protrusion length (L) was measured as the distance from the tip of the protrusion to the projection of the intersection of the major and minor axes of this ellipse with the protrusive fiber. The eccentricity of the protrusion (E) was calculated as follows:

$$Eccentricity = \frac{\sqrt{a^2 - b^2}}{a}$$

where a and b are half of the length of the major and minor axis respectively of the ellipse fit to the protrusion as described in Figure 2A.

The *coiling* dynamics at the tip of the protrusion was calculated as previously described [212]. Briefly, the maximum *coil* width (Figure 3A) was calculated as the largest *coil* width during a *coiling* cycle. The time taken to reach maximum *coil* width was calculated as the total time taken from the initiation of a *coiling* cycle till the maximum *coil* width was reached.

For the migration analysis, cells were manually tracked using ImageJ and the x,y location of the cell centroid was recorded for every third frame (*i.e.*, every twelve minutes). The instantaneous speed was then calculated as follows (in µm/hr):

$$Instantaneous\ Speed = \frac{\sqrt{(y_t - y_{t-1})^2 + (x_t - x_{t-1})^2} \times 60}{12}$$

where (x_{t-1}, y_{t-1}) are the coordinates of the centroid of a cell at any given frame in µm while (x_t, y_t) are the coordinates of the centroid of the same cell three frames (*i.e.*, twelve minutes) later.

The overall average speed of the cell was then calculated as the average of all the instantaneous speed values. The persistence of migration was calculated as follows:

$$Persistence = \frac{\sqrt{\left(y_{final} - y_{initial}\right)^2 + \left(x_{final} - x_{initial}\right)^2}}{\sum_{t=1}^{t=n}\sqrt{(y_t - y_{t-1})^2 + (x_t - x_{t-1})^2}}$$

where (x_{final}, y_{final}) are the coordinates of the centroid of a cell at the last frame (n[th] frame) tracked in μm while $(x_{initial}, y_{initial})$ are the coordinates of the centroid of the same cell at the first frame tracked. The denominator is defined similar as above for the instantaneous speed.

The circularity of the cell during migration was defined as follows:

$$Circularity = \frac{4 \times \pi \times Cell\ Area}{(Cell\ Perimeter)^2}$$

The value for circularity ranges from 0-1 wherein a value closer to 1 indicates a circular shape while a value closer to 0 indicates a more "straight-line" shape. To quantify the average circularity and average spread area of the cell during migration, three random frames were chosen and both these metrics were averaged over these three frames.

For the analysis, cells that were in contact with another cell or dividing during the imaging window were not considered.

Force Model for Nanonet Force Microscopy: In order to calculate the forces from the fiber deflections, the fiber deflection was tracked for three randomly selected, consecutive frames and was analyzed in MATLAB (2017a) using our previously reported methods [157,213]. Briefly, the ~220 nm diameter, horizontal force fibers were modeled as beams with fixed-fixed boundary conditions since they were fused to the larger diameter ~2 μm, vertical base fibers at both ends. A finite

element model was used to obtain the fiber deflection profile from an arbitrary initial force input and the error between the model fiber profile and the experimentally tracked profile was minimized by using an optimization framework while simultaneously updating the force values iteratively (Figure 5A). The average force was finally calculated as the average of the three consecutive frames selected.

Immunostaining: Cells were fixed in 4% paraformaldehyde (Santa Cruz Biotechnology, Dallas, Texas) dissolved in PBS for 15 minutes, and rinsed in PBS twice. The cells were then permeabilized with 300 µl permeabilization solution (0.1% Triton-X-100 in PBS). After 15 minutes, the cells were blocked by 10% goat serum in PBS for 30 minutes, and incubated with the anti-paxillin antibody (Invitrogen, Carlsbad, CA) in antibody dilution buffer (0.3% Triton-X-100 and 1% BSA in PBS) at a ratio of 1:100 overnight at 4 °C. The secondary antibody Alexa Fluor 488 goat anti-rabbit (Invitrogen) and the rhodamine- or FITC-conjugated phalloidin were diluted in the antibody dilution buffer at the ratio of 1:100 and 1:80 respectively and added to the wells. The sample was then stored in a dark place for 45 minutes followed by three PBS washes. Finally, the nuclei were counterstained with 300 nM of DAPI (Invitrogen) for 15 minutes. The scaffolds were kept hydrated in 2 ml of PBS and imaged using a 63× (water-based immersion) magnification.

Statistics: Statistical analysis of the data was conducted using RStudio (RStudio, Boston, MA) software. The Shapiro-Wilks normality tested was used to check the normality of the data sets. Analysis of variance (ANOVA) was used to test for the statistical significance between different data sets. The following symbols are used to represent the statistical significance levels: *<0.05, **<0.01 and ***<0.001. If there is no comparison shown between any data sets, it implies that

there is no statistically significant difference between them. All the error bars represent standard error of mean.

Results:

Design of fiber networks to quantify biophysical metrics in ovarian cancer

We used the non-electrospinning STEP technique to fabricate suspended fiber networks (**Figure 4.1**) for quantifying protrusion, *coiling,* migration dynamics, and the forces exerted by the three MOSE phenotypes representing the various stages of ovarian cancer progression.
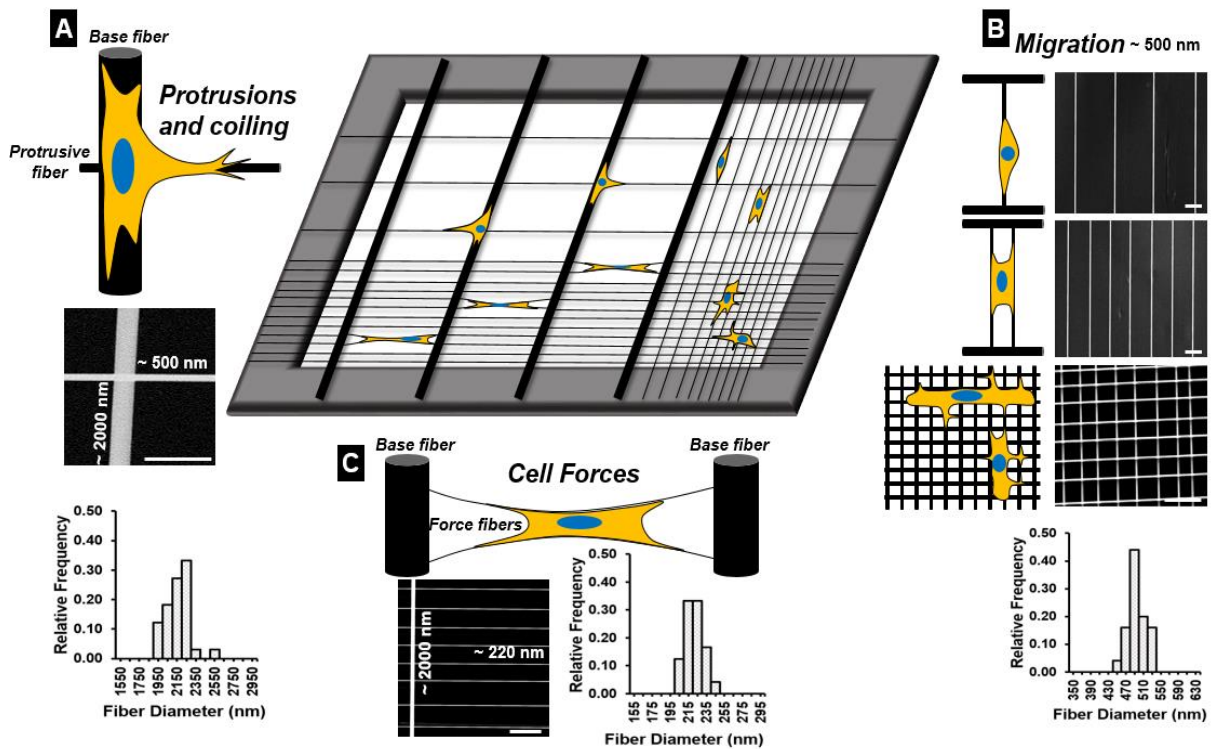
Figure 4.1: Overview of the STEP suspended fiber networks used to quantify biophysical metrics. (Center) Schematic showing an overview of the suspended fiber networks with precisely tunable network architecture. Schematic and corresponding SEM images of the specific fiber networks used to quantify (A) protrusion and *coiling* dynamics, (B) migration dynamics on single fiber, two fiber and crosshatch networks, and (C) forces exerted during migration. Histograms show the fiber diameter distribution for the ~2 μm "base fibers" used in the protrusion and force networks, ~500 nm diameter fibers used in the protrusion and migration networks and ~220 nm diameter fibers used in the force networks. Scale bars in all SEM images are 10 μm.

To quantify protrusion dynamics and *coiling* occurring at the tip of the protrusion, we use an orthogonal network of fibers with mismatched fiber diameters. The larger diameter (~2000 nm) "base fibers" constrain cell migration, while orthogonally deposited smaller diameter (~500 nm) "protrusive fibers" allow the study of individual protrusions[214].

To investigate cell migration, we designed fiber geometries that recapitulate the cell morphology observed *in vivo* in the complex, fibrous sub-mesothelium. Transmission electron micrograph images taken in separate studies have shown stromal cells adopting a distinctly polarized and elongated morphology while interacting with collagen fibers in the sub-mesothelium [204,205]. Since these shapes are typically associated with persistent migration in cancer invasion, we used our previously described strategies of parallel networks of fibers [23,165,215] and crosshatch network of fibers [216] to achieve shape-dependent persistent migration. Specifically, modulating the spacing between adjacent aligned fibers allowed us to study cell migration in elongated shapes on "single fibers" (~25 μm inter-fiber spacing), on "two fibers" (~15 μm inter-fiber spacing), and on crosshatch network of fibers with a ~6 μm × ~6 μm grid size.

Cells migrating in fibrous environments tug on individual fibers causing them to deform. To estimate the tugging forces, we have developed the Nanonet Force Microscopy (NFM) technique[157,213,217,218]. Briefly, NFM nanonets comprise of strut-like, large diameter (~ 2000 nm) "base fibers" orthogonal to which are deposited smaller diameter (~220 nm) "force fibers" (**Figure 4.1C**). NFM estimates forces from deflection of fibers and by establishing force vectors that originate from focal adhesion clustering (FAC) occurring at poles of cells and directed along the dominant tension bearing f-actin stress fibers.

All measurements described in this study were conducted in hours using metric-specific fiber networks and can be combined in a single scaffold for high throughput and high content screening (schematic in Figure 4.1).

Protrusion length is the longest in the most aggressive MOSE phenotype

Cells extend protrusions to probe and sense the surrounding environment continuously. We wanted to inquire if *in vitro* fibrous environments can identify the metastatic potential of cancer cells through protrusion dynamics. We defined two metrics of eccentricity (E) and protrusion length (L) (**Figure 4.2A.i**) to quantify protrusion dynamics [212,214]. The eccentricity metric represents the shape of a protrusion, with low eccentricity (E< ~0.6), signifying a "rod-like" protrusion, while high eccentricity (E> ~0.8) signify a "kite-shaped" broad protrusion. The
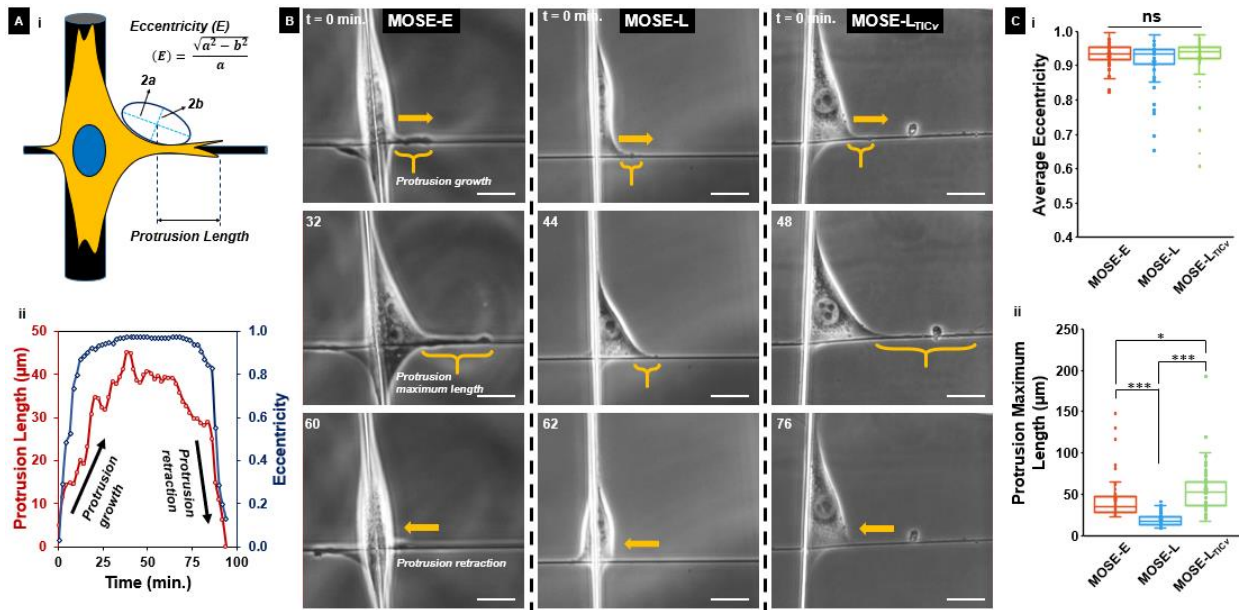
Figure 4.2: Protrusion dynamics show significant differences across the MOSE model. (A.i) Schematic showing measurements for protrusion length ("L") and eccentricity ("E"). (A.ii) Representative "protrusion cycle" plot for a MOSE-E cell. (B) Representative phase images for all three MOSE phenotypes showing typical protrusion cycles. Yellow parentheses indicate the protrusions in each image. Scale bars are all 20 μm. (C) Comparing the (i) maximum average eccentricity and (ii) maximum protrusion length for the MOSE-E, MOSE-L and MOSE-L$_{TICv}$ cells. n-values for the MOSE-E, MOSE-L and MOSE-L$_{TICv}$ cells are 50 (23 cells), 55 (25 cells) and 64 (28 cells), respectively.

combination of two metrics defines a "protrusion cycle," which typically lasted less than two hours for each phenotype. The cycle started with the broadening of the protrusion (increase in E), followed by an increase in the length, and ended with protrusion retraction to the main cell body (**Figure 4.2A.ii**). Phase images depicting a typical protrusion cycle for each MOSE phenotype are shown in **Figure 4.2B,** while representative plots for protrusion cycles for all three phenotypes are shown in **Supplementary Figure 4.S1**. We quantified both the maximum eccentricity and the maximum protrusion length for the three MOSE phenotypes (MOSE-E, MOSE-L, and MOSE-L_{TICv}). We found that there was no significant difference in the average maximum eccentricity (**Figure 4.2C.i**). However, the maximum protrusion length was lowest in the MOSE-L cells (19.2 ± 1.0 μm) while the most aggressive phenotype, the MOSE-L_{TICv} cells formed the longest protrusions (average length of 54.1 ± 3.4 μm, **Figure 4.2C.ii**). Overall, our results indicate that the most aggressive cancer phenotype in the model correlates with the most extended protrusions.

Coiling at the tip of protrusions correlates with an increasingly aggressive MOSE phenotype

While extending protrusions, cancer cells sense the fiber curvature by *coiling* (wrapping-around the fiber axis) at the tip of the protrusion [212]. We wanted to inquire if *coiling* dynamics (**Figure 4.3A**) could be used as a measure of the disease progression in the MOSE model. From the *coiling* cycles for the three MOSE phenotypes (**Figure 4.3B**), we found that the maximum *coil* width increased with increasing aggressiveness of the MOSE model, with the MOSE-L_{TICv} cells showing a maximum *coil* width of 3.4 ± 0.1 μm, representing a 48% increase over the maximum *coil* width of 2.3 ± 0.1 μm displayed by the benign MOSE-E cells (**Figure 4.3C.i**). Furthermore, we found that the time taken to reach the maximum width increased with the aggressive phenotype (**Figure 4.3C.ii**). Thus, our data of *coiling* at the tip of the protrusion shows stark differences across

the MOSE model and suggests its potential use as a useful biophysical metric to determine metastatic capacity.
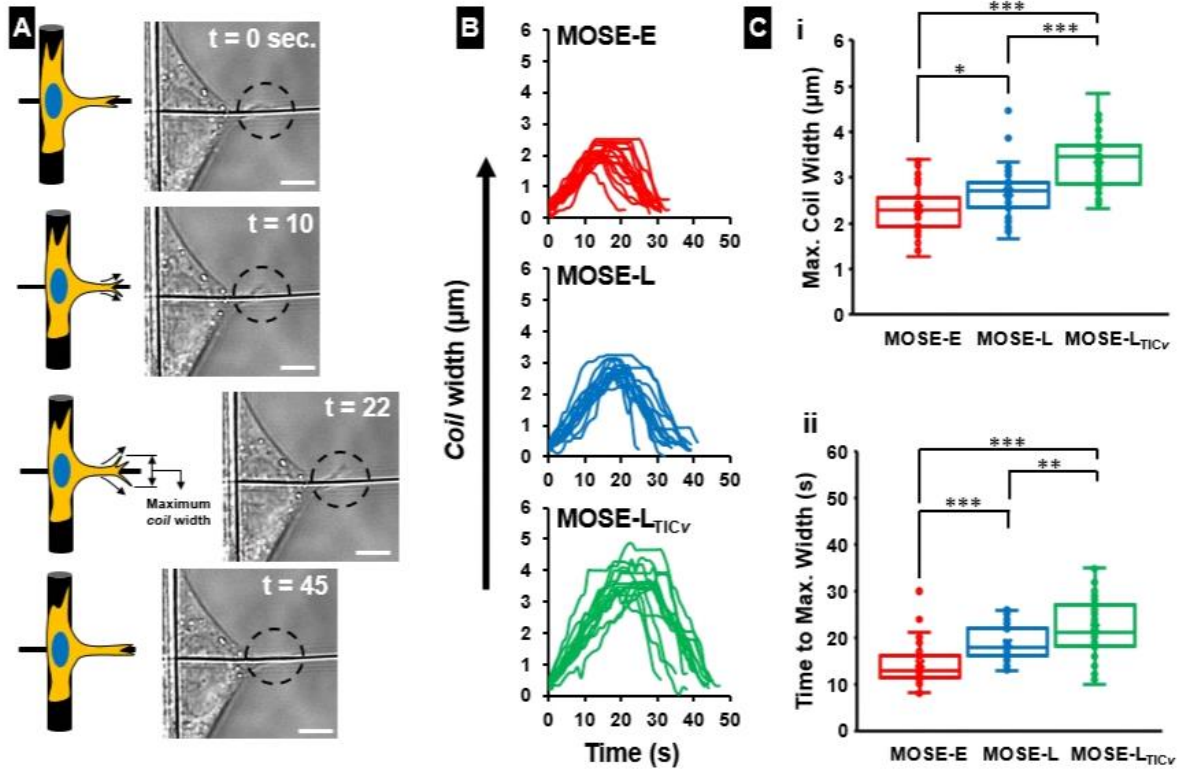
Figure 4.3: *Coiling* **dynamics at the tip of the protrusion are influenced by disease progression in the MOSE model.** (A) Schematic and phase images depicting a typical *coiling* cycle for a MOSE-L cell. Black dotted circles indicate the *coiling* structures. Scale bars are all 5 μm. (B) Comparing the coiling cycle between the MOSE-E, MOSE-L and MOSE-L$_{TICv}$ phenotypes. Sixteen *coiling* cycle profiles are shown for each case. (C) Comparing the (i) maximum *coil* width and (ii) time taken to reach the maximum *coil* width across the MOSE model. n = 40 for each category.

Migration speed of polarized cells depends on cell shape and disease stage

Given that protrusive activity is widely considered a precursor to cell migration [41,187], we interrogated whether the differences in protrusive dynamics and *coiling* behavior translated to differences in migration dynamics on suspended fibers across the MOSE model. To this end, we investigated polarized single-cell migration on anisotropic ("single fiber" and "two fibers") and low interfiber spacing dense orthogonal ("crosshatch network") networks (**Figure 4.4A.i-iv**). We

used cell migration on the flat, 2D glass surface as a control. Before quantifying the migration rate, we enquired whether the cell morphology was different across the MOSE phenotypes on the different substrates as both the spread area [219] and the degree of polarization [196] have previously been linked with influencing migration dynamics. Thus, we quantified both the cell spread area and circularity (a circularity value close to 1 indicates a perfect circle). We found that the benign MOSE-E cells were largest in the spread area, and the area decreased with an increase in invasiveness (**Figure 4.4B.i-iv**). Circularity, on the other hand, was the highest on flat 2D, indicating cells to be broad in shape (**Figure 4.4C. i-iv**). The low values of circularity indicating elongated shapes for cells on the single and two-fiber systems was expected. However, for cells attached to single fibers (spindle-shaped cells), the intermediate phenotype (MOSE-L) unexpectedly had the lowest area and highest circularity, indicating a rounded spindle morphology. Overall, our analysis across all substrates showed that the benign cells have the most extensive areas, whereas the circularity measure was not able to distinguish shape-based differences.

Having quantified the cell morphology, we next investigated their migration dynamics. First, we found that MOSE cells, regardless of the phenotype, migrated faster on suspended fibers compared to flat 2D (**Supplementary Figure 4.S2**). Next, we wanted to interrogate whether the faster migration rate correlated with disease progression. We found that the migration rate increased with the invasiveness of MOSE cells, except for intermediate MOSE-L cells migrating faster on single fibers (**Figure 4.4D.i-iv**). Specifically, the migration speed for the most aggressive MOSE-L$_{TICv}$ cells increased by 124%, 149%, and 126% over that of the benign MOSE-E cells on the two-fiber, crosshatch network, and flat substrates, respectively. Finally, we enquired if the faster migration rates observed on fibers were driven by differences in the persistence of motion for the cells. We found that on all the fiber categories, all phenotypes had higher persistence values

compared with flat 2D cells. Generally, the most aggressive phenotype did exhibit the highest persistence on each fiber substrate, although there was no statistical difference observed on either the single fiber or the two-fiber networks (**Figure 4.4E.i-iv**). Altogether, our data show that the most aggressive phenotype in the MOSE model has the lowest area but migrates the fastest with the highest persistence.
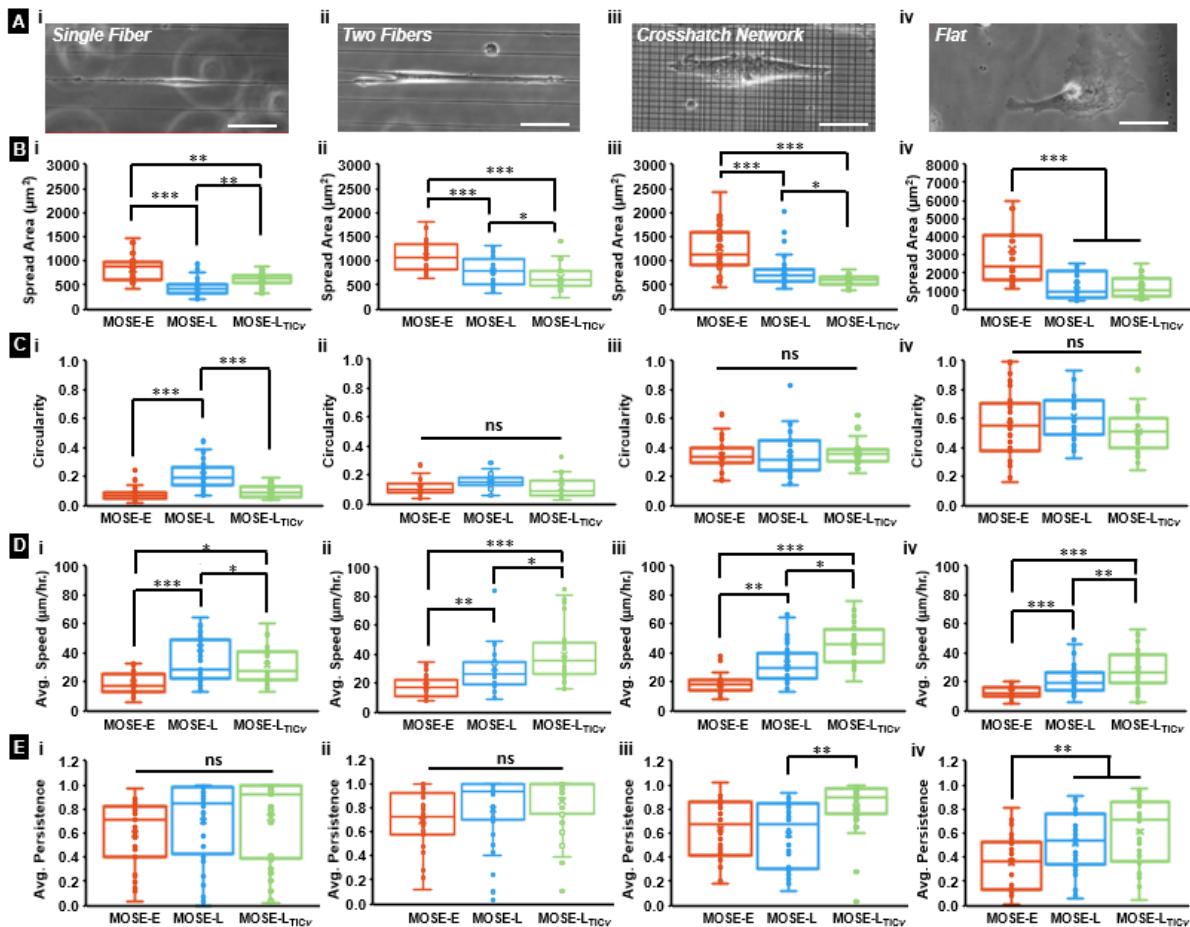
Figure 4.4: Migration of MOSE cells on suspended fiber substrates shows disease progression dependency. (A) Representative phase microscopy images showing MOSE-E cells on (i) a single fiber migration assay (cell interacting with only one fiber), (ii) a two-fiber migration assay (cell interacting with two fibers), (iii) a crosshatch network migration assay (cell interacting with an orthogonal fiber network) and (iv) on a flat, 2D surface (control). All the scale bars are 50 μm. Comparison of the cell spread area (B), Circularity (C), Average migration speed (D), and Average persistence (E) across the MOSE model on the (i) single fiber, (ii) two fibers, (iii) crosshatch network and (iv) flat substrates. n = 35 for all the single fiber substrates (MOSE-E, MOSE-L and MOSE-L$_{TICv}$), 30 for all the two fiber substrates, 32 for the crosshatch network and 25 for the flat surface.

MOSE force-disease biphasic relationship exhibits f-actin network dependence

During the migration process, cells continuously generate actomyosin contractility-driven forces that act on the surrounding substrate[220]. Given that the actin cytoskeleton undergoes significant reorganization during the disease progression in the MOSE model [211], we enquired if this correlated with the forces exerted by single cells. We have previously shown that on 2D flat substrates, the benign MOSE-E cells exhibit distinct actin cables in contrast to the cancerous MOSE-L, which exhibit a dense, mesh-like network lacking in prominent stress fibers [211]. We used nanonet force microscopy (NFM) (**Figure 4.5A**) to quantify the forces by establishing force vectors that originate at focal adhesion clusters (FAC) and are directed along the f-actin stress fibers. Using fluorescent images of filamentous actin (**Figure 4.5B.i**), we found that the average stress fiber angle of 10.2 ± 0.5 degrees in benign MOSE-E cells was significantly lower than both the MOSE-L (16.1 ± 1.4) and MOSE-L$_{TICv}$ (15.5 ± 0.9) cell lines. Using these average f-actin stress fiber angle values in our finite element model, we computed the forces exerted by single cells. We found that MOSE-E cells exerted the highest force of 305 ± 24 nN, which was 189% and 75% higher than the force exerted by the intermediate MOSE-L (106 ± 9 nN) and aggressive MOSE-L$_{TICv}$ (174 ± 10 nN) cells, respectively (**Figure 4.5B.ii**). The highest force being exerted by the MOSE-E cells is not surprising due to these cells having prominent actin stress fibers compared to the other two aggressive cell types. This result is also consistent with the lowest migration speed of these cells (Figure 4D.ii). The lower forces exerted by intermediate phenotype (MOSE-L) is presumably due to the reduction of well-defined actin networks (**Figure 4.5C**), and the wider distribution of angles formed by f-actin stress fibers, thus causing a large variability in force values. The increase in forces in the aggressive (MOSE-L$_{TICv}$) phenotype is attributed to the re-assembly of f-actin networks (Figure 5C). Taken together, our results suggest that with disease progression,
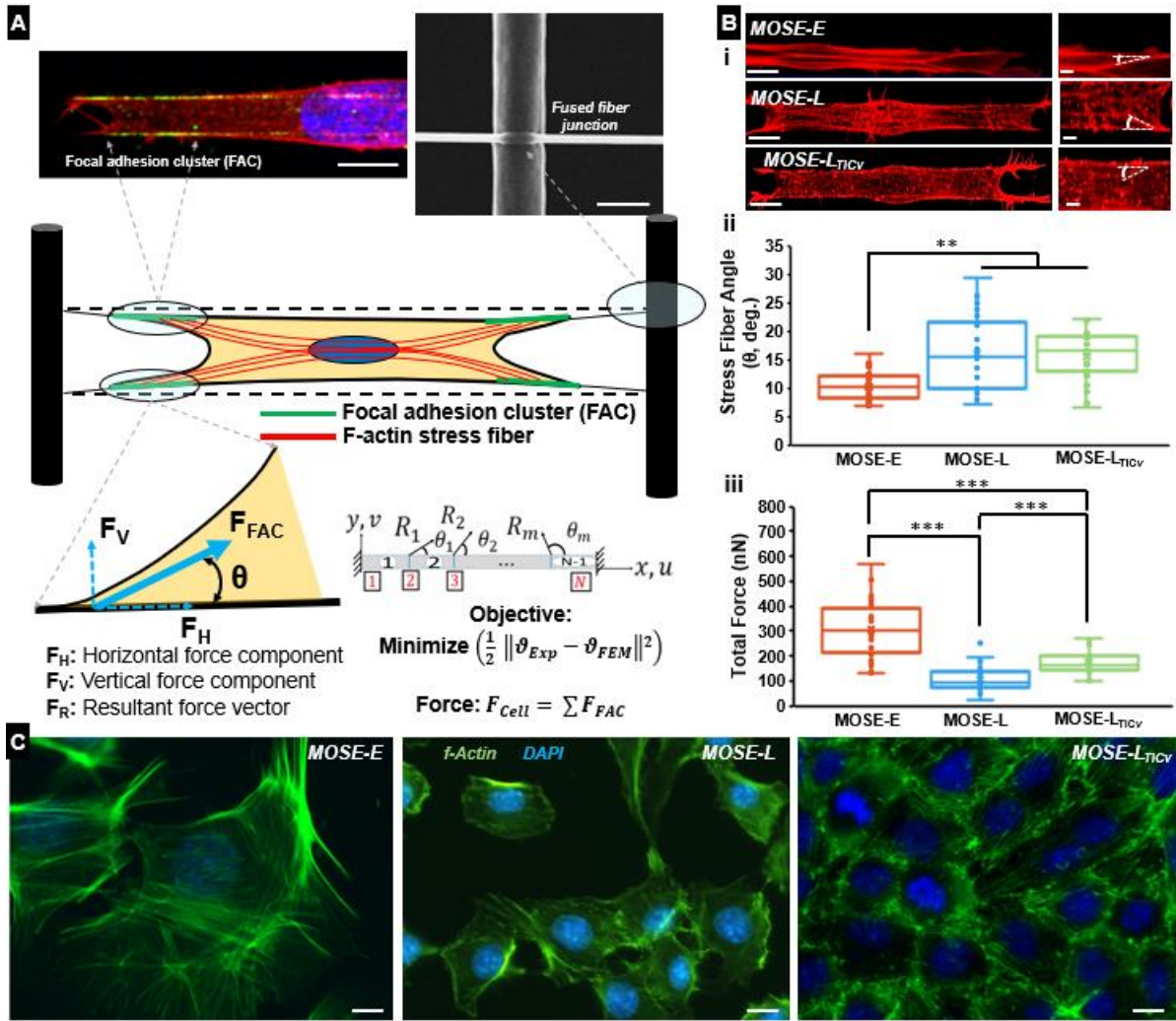
Figure 4.5: Quantifying forces exerted by the MOSE model using Nanonet Force Microscopy (NFM). (A) Schematic providing an overview of how forces are calculated using NFM. The fluorescent image on the top left shows actin filaments in red, nucleus in blue and paxillin in green. The SEM image shows a fused fiber junction. Scale bar is 10 μm in the fluorescent image and 2 μm in the SEM image. (B) Representative fluorescence microscopy images of (i) MOSE-E, MOSE-L and MOSE-L$_{TICv}$ cells with f-actin stained in red. To the right of each image is a zoomed in region highlighting the stress fiber angle (the angle is shown by the white dotted lines). The scale bars are 10 μm and 5 μm for the fluorescent images and their corresponding enlarged images, respectively. Quantifying the (ii) average stress fiber angle and (iii) force exerted across the MOSE cell lines. n = 27, 22 and 23 for the stress fiber angle measurements for the MOSE-E, MOSE-L and MOSE-L$_{TICv}$ cells, respectively. n = 24, 30, and 27 for the force measurements for the MOSE-E, MOSE-L and MOSE-L$_{TICv}$ cells, respectively. (C) Representative immunofluorescence images of stress fiber networks in cells on flat showing well organized actin cables in benign cells, loss and partial recovery of f-actin structures in intermediate and aggressive phenotypes, respectively. Scale bars 10 μm.

cancer cells exert lower forces compared to benign cells, which is influenced by the network of f-

actin stress fibers.

Human ovarian cancer cell pair shows similar biophysical trends as the MOSE Model

We next wanted to confirm that the biophysical metrics for the MOSE cells, a model for serous ovarian cancer, were not limited to a mouse cell model but could be extended to human cancer cell lines. To this end, we repeated key protrusion, *coiling*, force and migration measurements for a benign (FNE) and malignant (FNLE) syngeneic human fallopian tube cancer cells. Overall, we found that the FNE/FNLE cell pair followed the same trend as observed between the MOSE-E (benign) and MOSE-L (slow developing disease) cells in the MOSE model. Specifically, the FNE cells exhibited longer protrusion length (**Figure 4.6A.i**) and lower maximum *coil* width compared to the metastatic FNLE counterparts (**Figure 4.6A.ii**). Furthermore, on using NFM to quantify the forces exerted by single cells, we found that the FNE cells exerted significantly larger forces on the suspended fibers compared to the FNLE cells, that may be correlated to their extensive actin stress fibers (**Supplementary Figure 4.S4**) and the lower stress fiber angle indicating a more contractile morphology (**Figure 4.6B.i-ii**). Finally, quantification of the migration dynamics on single fiber networks, two fiber networks and on flat (which served as the control) revealed that the FNLE cells migrated faster on all the substrates compared to the FNE cells (**Figure 4.6C**), similar to the trend observed between the MOSE-L cells as compared to the MOSE-E cells in the mouse model. The higher speed observed for the FNLE cells was driven by a higher persistence on both fiber networks and the flat surface (**Figure 4.6D**). Taken together, these results indicate that the biophysical metrics described in this study are comparable to the differences between benign MOSE-E and malignant MOSE-L cells. While there is no direct comparison of tumorigenicity, FNLE cell appear to have lower tumor forming capacities but higher metastatic potential than transformed ovarian surface epithelium [209] which appears to be similar to the MOSE-L cells [206]. Further, our previous studies show similar mitochondrial

59
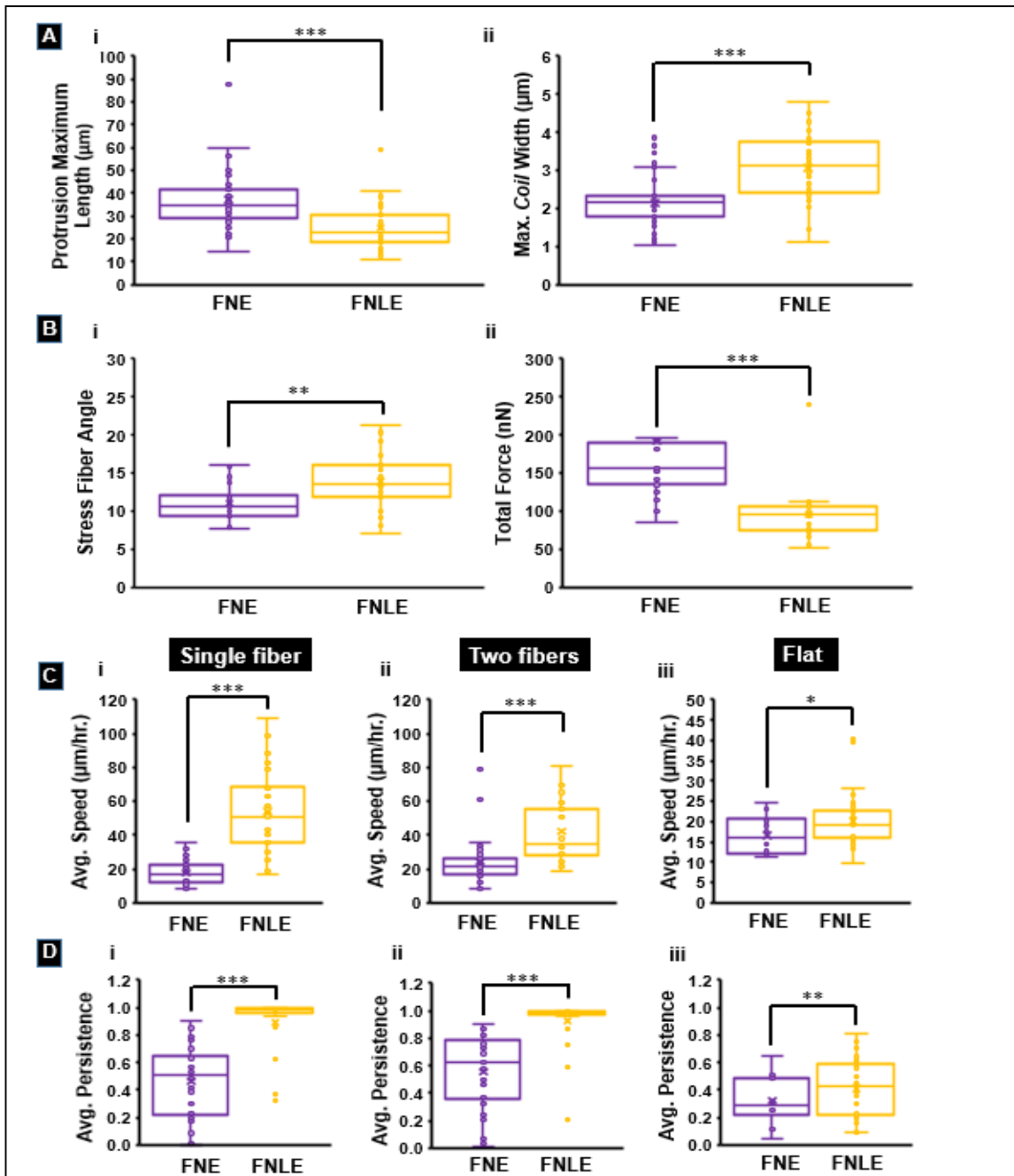
Figure 4.6: Quantification of key biophysical metrics between benign (FNE) and metastatic (FNLE) human ovarian cancer cell pair. (A) Quantification of the (i) maximum protrusion length and (ii) maximum *coil* width between the FNE and FNLE cells. n value is 52 for the protrusion measurements and 40 for the *coil* width measurements for each category. (B) Quantification of the (i) average stress fiber angle exhibited and (ii) the total force exerted by FNE and FNLE cells. n value is 28 for the stress fiber measurements and 20 for the force measurements for each cell category. Quantification of (C) migration speed and (D) persistence for both cell types on (i) single fibers (ii) two fibers and (iii) flat surface. n value is 30 and 25 for the FNE and FNLE cells respectively on all the substrates considered.

morphology and function of the MOSE-L and FNLE cells that are different from the MOSE-L$_{TICv}$

221,222. Thus, biophysical metrics could be applied to the distinction of human benign and ovarian cancer and tissues.

Discussion:

Despite metastasis being the leading contributor to cancer-related deaths, there is currently no clear indicator for predicting the metastatic potential of a tumor in a patient [223]. Clinical oncologists primarily depend on a combination of pathology results [224,225] and gene expression or mutational signatures as a predictive tool for accurate cancer prognosis [226–229]. However, genetic profiling can be a time-limiting step which is further compounded with heterogeneity in tumor populations [230,231] and non-mutational regulatory factors that combine to determine the metastatic capacities of the cells usefully. In addition to characterizing individual genetic modifications, biophysical metrics can serve as complementary clinical indicators of metastatic potential[188].

The biophysical metrics implicated in invasion (protrusions, migration, and exertion of force) are specifically contextual in ovarian cancer metastasis, due to the ability of ovarian cancer cells to physically invade through both the mesothelial layer lining the peritoneal organs and subsequently the complex fibrous sub-mesothelium for successful dissemination to distal sites and further colonization [232]. In this study, our goal was to use suspended ECM-mimicking nanofiber networks to quantify, within a timespan of hours, relevant biophysical metrics in a progressive ovarian cancer model (MOSE), to discern disease progression.

We quantitated protrusion dynamics (length and eccentricity) for the MOSE model (Figure 4.2) and found that the most aggressive cancer cells (MOSE-L$_{TICv}$) formed the longest protrusions. Our findings are in agreement with our previous study that demonstrated that the highly metastatic breast adenocarcinoma MDA-MB-231 cells exhibit significantly longer protrusion lengths

compared to the non-tumorigenic breast epithelial MCF-10A cells[214]. Our findings are also in agreement with other studies using a combination of both flat 2D assays and gel-based 3D assays demonstrating that protrusions of squamous cell carcinoma, glioblastoma, bladder cancer, and breast cancer can be correlated to metastatic capacity [223,233,234]. However, our finding that intermediate aggressive MOSE-L phenotype extends shorter protrusions compared to the benign MOSE-E cells is unexpected. We inquired if the cell area played a role in the formation of shorter protrusions. We estimated the area of MOSE-L cells attached to the main *base* fiber in protrusion assay was smaller compared to MOSE-E cells. Normalizing the protrusion length to the cell spread area did not show differences in the protrusion lengths between the benign and intermediate cells in the MOSE model (**Supplementary Figure 4.S3**). Areal normalization of the MOSE model suggests that protrusion length may not be a sufficient standalone metric capable of differentiating between benign and tumorigenic phenotypes.

Next, since *coiling* occurs at the tip of protrusions, we found that the *coil* size increased with increasing aggressiveness of the MOSE cells independent of the cell area (Figure 4.3). Our findings concur with our earlier study wherein we demonstrated that the metastatic breast cancer cells exhibit significantly larger *coil* sizes compared to their non-tumorigenic counterparts across a range of fiber diameters from ~135 nm to ~1000 nm [212]. Altogether, our results indicate that *coiling* behavior that is unique to fiber networks correlates robustly with ovarian cancer disease progression, thus functioning as a more deterministic metric in identifying the metastatic potential of single cancer cells.

In addition to protrusion and *coiling*, we investigated cell migration as another potential biophysical marker. We designed our fiber networks to achieve *in vivo* resembling elongated cell morphologies that led cells of all phenotypes to move persistently compared to flat surfaces. We

found that on both two-fiber and crosshatch fiber geometries, the migration rate of the polarized ovarian cancer cells positively correlated with increasing aggressive phenotype. In contrast, only in the case of the single fiber geometry, the intermediate MOSE-L cells exhibited the highest migration rate, which is consistent with their smaller size and rounded spindle morphology (Figure 4.4). Our migration findings are in agreement with reported studies that show increasing invasive potential of cancer cells correlates with increasing migration rate across a range of cell types, including breast and thyroid cancer cells [235–237]. Additionally, *in vivo,* human epidermoid cancer cells with lower invasive capacity are shown to have an approximately four-fold reduction in migration rate compared to their more invasive counterparts [193]. Thus, altogether, we suggest that migration and persistence of migration can be suitable predictors of invasive potential.

Finally, we used the Nanonet Force Microscopy (NFM) platform to quantify the forces exerted by the MOSE cells and found a biphasic relationship between the force exerted with disease progression such that the benign MOSE-E cells exerted the highest forces (Figure 4.5). While the relationship between higher migration rates and lower force exertion by aggressive cancer cells seems reasonable, previously reported studies using traction force microscopy had shown both similar and contrasting results. Our findings are in agreement with Indra, *et al.*, who quantified a decrease in traction forces exerted by four murine breast cancer cell lines derived from the same primary tumor but with increasing metastatic capacity [195]. They attributed the loss in forces to a reduction in the number of focal adhesions suggesting a less adhesion-dependent migratory mode with disease progression. In contrast, Rösel *et al.* found that metastatic A3 sarcoma cells exert five times higher traction forces compared to less metastatic K2 counterparts due to an upregulation of ROCK protein, which promotes cytoskeletal contractility[238]. Similarly, Kraning-Rush, *et al.* quantified traction forces using an isogenic cell model, which represents the

full spectrum of neoplastic progression in breast cancer and found that forces increased with disease progression [188]. In our case, we suggest that the drop in forces with disease progression is due to the disorganization and transition of long and distinct f-actin fibers in the benign MOSE-E cells to a mesh-like network in the MOSE-L cells causing them to be softer [211,239,240]. Indeed, the angles formed by actin stress fibers are at a shallower angle in MOSE-E cells, due to which these cells can apply large forces and cause the fibers to deflect more inwards (**Supplementary Figure 4.S5**). However, MOSE-L$_{TICv}$ exhibit partial reassembly of actin cables compared to the MOSE-L and, thus, the exerted forces were higher, but not reaching the levels exerted by the MOSE-E. Our data indicates that while forces are lower in ovarian cancer cells compared to the benign counterparts, the force exertion increases with invasiveness between the two cancer phenotypes. Altogether, our findings suggest that forces can provide insights into the metastatic capacity of cancer cells.

Summary:

In this chapter, we wanted to lay the groundwork for developing a genetic-marker independent, biophysical metastatic index which could provide a complementary tool to cancer diagnostic tools. To this end, we used the STEP technique to manufacture suspended fiber networks which allowed us to quantify the protrusion, *coiling* and migration dynamics and forces exerted by the previously reported MOSE model which represents ovarian cancer disease progression from benign to aggressive phenotypes. Here, we found that the *coiling* dynamics at the tip of the protrusion rather than the protrusion length or breadth strongly correlated with disease progression. Furthermore, migration dynamics for the MOSE (mouse ovarian surface epithelial) model correlated with disease progression on both two fiber and crosshatch network platforms. Finally, we found that while the force exerted was highest for the benign MOSE phenotype, the

force exertion increased with increasing invasiveness between the two cancer phenotypes. Finally, we confirmed our results with a human benign/metastatic ovarian cancer cell pair thus suggesting that the predictive capacity of these biophysical metrics are not limited to a mouse model.

While our results are promising, we caution that biophysical metrics by themselves may not be sufficient to describe the metastatic potential, and they should be complementarily evaluated with current diagnostic assays to understand the mechanical plasticity of cancer cells with disease progression. However, our demonstration of the importance of ECM-mimicking suspended fibers suggests the possibility of their use as natural culture environments post-biopsy, thus minimizing phenotypic shifts. Overall, the ability to quantitate phenotype sensitive biophysical metrics within a short time-span of hours provides new pre-screening tools that open unique opportunities for faster detection of cancer.

Supplementary Figures:
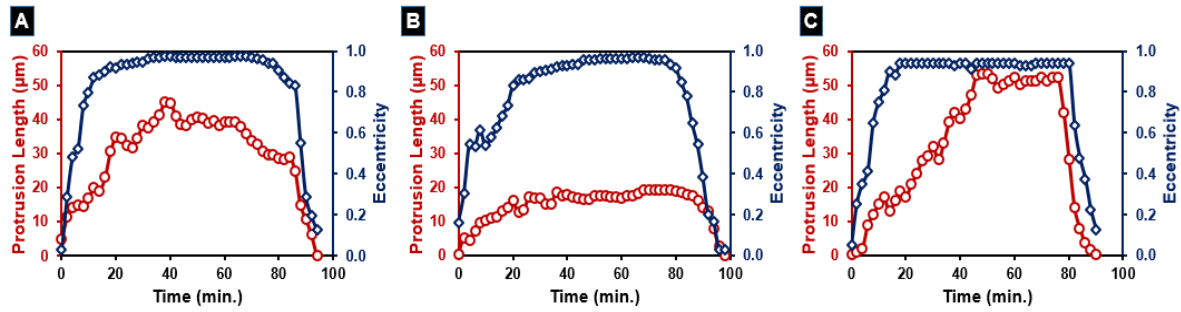
Supplementary Figure 4.S1: Representative protrusive cycles for (A) MOSE-E (B) MOSE-L and (C) MOSE-L$_{TICv}$ cells on a 500 nm diameter protrusive fiber.
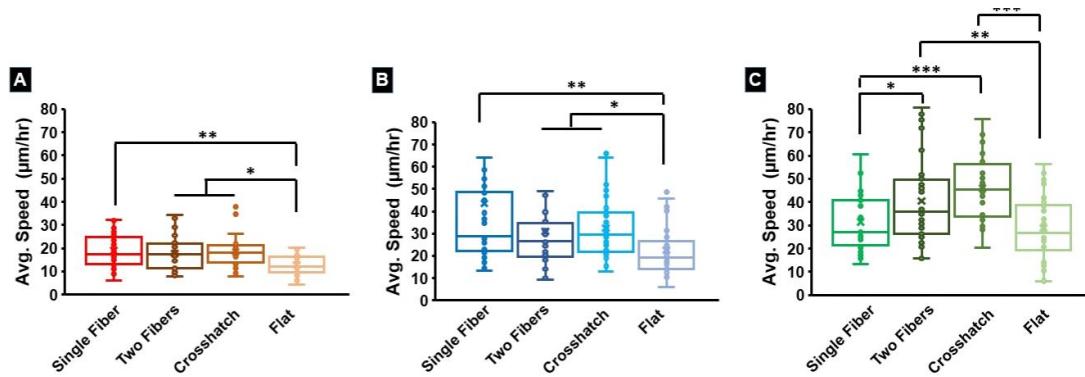
Supplementary Figure 4.S2: Average migration speed for (A) MOSE-E (B) MOSE-L and (C) MOSE-L$_{TICv}$ cells on different fiber network substrates and flat (control). n = 35, 30, 32 and 25 for the single fiber, two fibers, crosshatch and flat substrates respectively for each cell type.
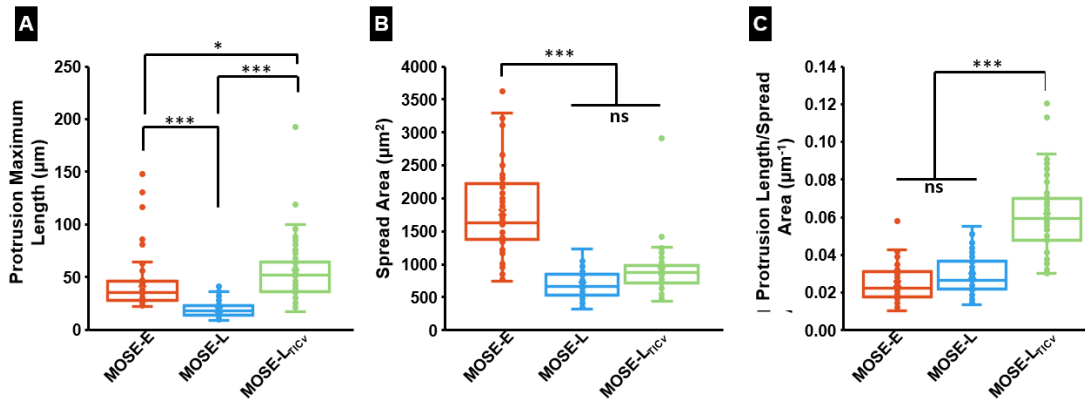
Supplementary Figure 4.S3: Comparing the protrusion length normalized to cell spread area across the MOSE phenotypes. (A) Maximum protrusion length (B) spread area at the maximum length time point and (C) maximum protrusion length per unit spread area for the different MOSE phenotypes. n-values for the MOSE-E, MOSE-L and MOSE-L$_{TICv}$ cells are 50, 55 and 64, respectively.
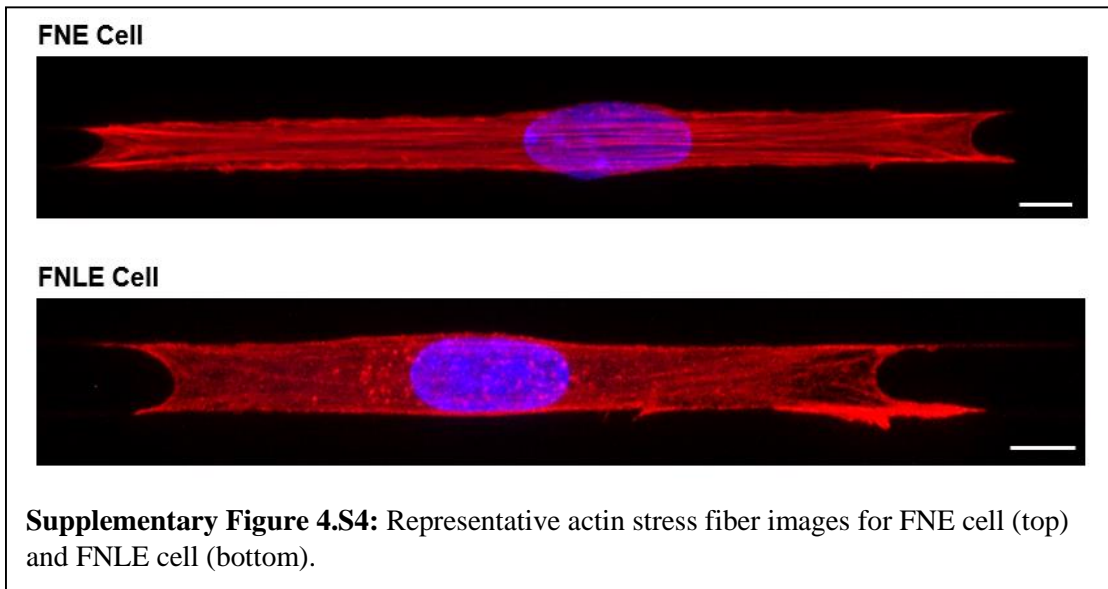
Supplementary Figure 4.S4: Representative actin stress fiber images for FNE cell (top) and FNLE cell (bottom).
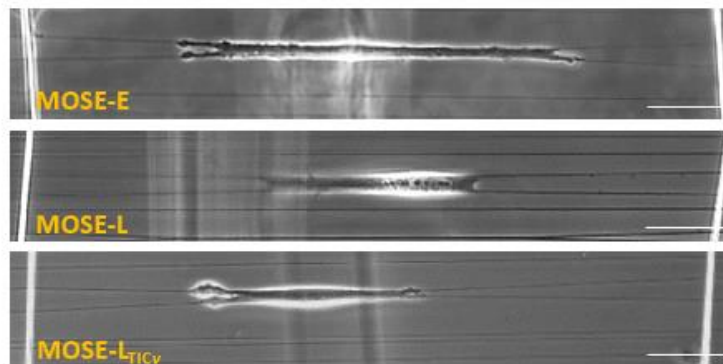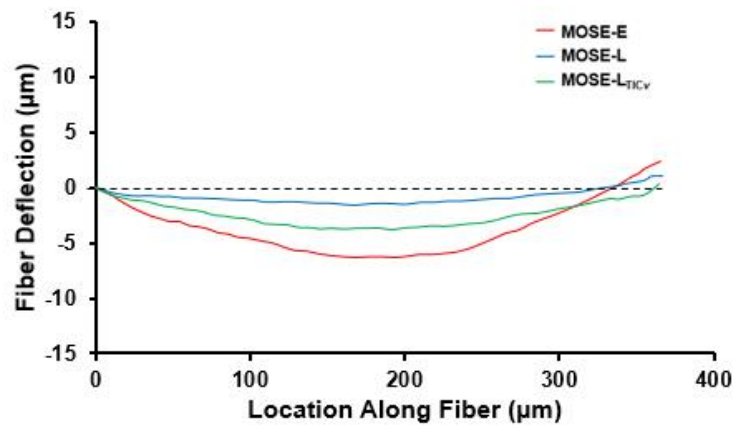
Supplementary Figure 4.S5: Average fiber deflection profiles for the different MOSE phenotypes on the NFM platform and representative phase images showing the fiber deflection for each phenotype. Dotted line represents the undeflected fiber profile. Each profile is an average of 11 different fiber deflection profiles. Scale bars are 20 μm.

Chapter 5: IRSp53 – Tracing IRSp53 Effects Deep Inside the Cell From its Footprints at the Cell Tips

Introduction:

The crescent-shaped Bin/Amphiphysin/Rvs (BAR) domain proteins are crucial regulators of cell membrane curvature. They are linked to essential cellular processes, such as protrusion formation, membrane trafficking, and cell migration, including cancer metastasis [66,67,241–243]. The canonical BAR and F-BAR domains possess an intrinsically curved concave surface that binds to the negatively charged membrane and is typically involved in forming membrane invaginations, including clathrin-coated pits, caveolae, and transverse tubules. In contrast, the I-BAR domains possess an intrinsically curved convex surface and are involved in the extension of cell protrusions such as thin, "finger-like" filopodia and broader, "sheet-like" lamellipodia [69,244,245]. Theoretical studies have also suggested that convex-shaped proteins are involved in forming the cellular protrusions through polymerization of cortical actin [246–249].

Amongst the I-BAR domain of proteins, the Insulin Receptor tyrosine kinase Substrate protein of 53 kDa (IRSp53) has been extensively studied. It links the plasma membrane deformations and associated protrusive activity at the cell boundary to the underlying actin cytoskeleton [244]. Based on the intracellular localization, IRSp53 is supposed to utilize different sets of downstream effectors and upstream regulators to connect the cell membrane to the cytoskeleton. In the filopodia, IRSp53 binds to CDC42, essential actin regulating GTPase for filopodia [250–255]. In contrast, when localized in the lamellipodia, IRSp53 acts as an adapter molecule linking with the Rho GTPase Rac, an essential activator of the WAVE protein complex that activates the Arp2/3 complex, which in turn promotes actin polymerization and protrusion formation at the cell membrane [256–260]. Not surprisingly, studies spanning various cell lines

cultured on flat 2D substrates have demonstrated that the depletion of IRSp53 results in impaired protrusive activity at the cell membrane [69,244,257]. Additionally, IRSp53 inhibition has been shown to thwart cell migration in both transwell migration and wound healing *in vitro* assays and *in vivo* studies using zebrafish primordial germ cells and mice [261–263]. Consequently, IRSp53 is being considered a potential therapeutic target for hindering cancer metastasis [264–266].

In this study, we inquired if IRSp53's role at the cell tips was felt deep inside the cell, particularly in fibrous environments mimicking the native extracellular matrices (ECM), as we have previously shown protrusive and migratory behavior to be sensitive to fiber curvature[143,212,214,267]. Using high and low curvature suspended fibers, we probed the role of IRSp53 in the migration cycle starting from membrane protrusions followed by the establishment of contractility and sculpting of the nucleus. In doing so, we discovered that normal stick-slip migratory phenotype transitioned to a slower sliding phenotype with low cell body-nucleus correlation and retrograde actin flow with IRSp53 depletion. Overall, our experimental and theoretical study in a biologically relevant environment describes IRSp53's role in mechanotransduction, with implications in pathophysiological conditions.

Methods:

Fiber Network Fabrication

The previously reported non-electrospinning Spinneret Based Tunable Engineered Parameters (STEP) method was used to fabricate all the suspended fiber networks used in this study. Briefly, polystyrene (PS, Scientific Polymer Products, Ontario, NY) of $\sim 2\times 10^6$ g/mol molecular weight was dissolved in xylene (Thermo Fischer Scientific, Pittsburgh, PA) at 6% (w/w) concentration and 10% (w/w) concentration to prepare the solutions for spinning the ~135 nm and ~500 nm

diameter fibers respectively. To spin the ~2 μm base fibers for the protrusion, *coiling*, and force studies, a 5% (w/w) concentration solution of polystyrene of ~15×10^6 g/mol molecular weight was used. The solutions were prepared at least 2 weeks prior to spinning the fiber networks.

Scanning Electron Microscopy

Environmental Scanning Electron Microscope (ESEM) was used to take images of the suspended fibers in order to confirm the fiber diameter. Prior to imaging the scaffolds, they were coated with a 7 nm thick layer of Platinum-Palladium using a Leica sputter coater (Leica, Wetzlar, Germany). The images were taken at an electron beam voltage of 10 kV and a spot size of 3.5 using the Everhart-Thornley detector (ETD). The working distance was maintained at ~11 mm. Appropriate magnification factor was used depending on the application.

Cell Culture

U-251 cells were obtained from the Japanese Collection of Research Bioresources Cell Bank. The IRSp53 knockout (KO) were generated by the CRISPR/Cas9 system, as described previously [268]. The guide RNA targeting the first exon of IRSp53 (CCATGGCGATGAAGTTCCGG) was designed using the server http://crispr.mit.edu and inserted into the pX330 vector [268]. After transfection, the cells were cloned by monitoring the GFP fluorescence from the reporter plasmid pCAG-EGxxFP with the IRSp53 genome fragment using a fluorescence activated cell sorter [FACSAria (BD)] [269]. The expression of GFP or GFP-IRSp53 in the IRSp53 knockout cells was performed by the retrovirus-mediated gene transfer, as described previously [269]. All cell lines were cultured in high glucose DMEM (Thermo Fisher Scientific) supplemented with 10% bovine calf serum (Thermo Fischer Scientific) and 1% penicillin-

streptomycin solution (Thermo Fischer Scientific) and stored in an incubator at 37°C in 5% CO_2 and humidified conditions.

Cell Seeding and Experiment

In preparation for the experiments, the scaffolds were first affixed to the glass bottom of 6-well dishes (MatTek Corp., Ashland, MA) using sterile, high-vacuum grease (Dow Corning, Midland, MI). The scaffolds were then soaked in 70% ethanol for disinfection followed by two phosphate buffered saline (PBS) washes (Thermo Fisher Scientific). Subsequently, the fibers were coated with either 4 µg/ml fibronectin (Invitrogen, Carsbad, CA) or 4 µg/ml rhodamine fibronectin (Cytoskeleton Inc., Denver, CO) for 2 hours prior to cell seeding to aid cell attachment to the fibers. Once the cell culture reached ~80% confluency, 0.25% Trypsin (ATCC, Manassas, VA) was added and the culture was incubated for ~ 5 minutes. After the cells detached from the flask surface, 3 ml of fresh cell media was added to dilute the effect of the trypsin. The entire solution was then placed in a centrifuge at 1000 RPM for 5 minutes. Following the centrifugation, the media was aspirated and the cells were resuspended in fresh media. Finally, cells were seeded at a density of ~3000,000 cells/ml on the scaffolds.

Immunostaining

Cells were fixed in 4% paraformaldehyde (Santa Cruz Biotechnology, Dallas, Texas) dissolved in PBS for 15 minutes, and rinsed in PBS twice. 300 µl of permeabilization solution (0.1% Triton-X-100 in PBS) was then added to permeabilize the cells. After 15 minutes, the permeabilization solution was aspirated and the cells were blocked using 10% goat serum in PBS for 30 minutes. Following this, the cells were incubated with either the anti-lamin A/C primary antibody or the anti-paxillin antibody (Abcam, Cambridge, United Kingdom) dissolved in

antibody dilution buffer (0.3% Triton-X-100 and 1% BSA in PBS) at a ratio of either 1:200 (for

lamin) or 1:500 (for paxillin) for either 2 hours at 37°C (for lamin) or 16 hours at 4°C (for paxillin).

After the incubation period, the secondary antibody Alexa Fluor 647 goat anti-mouse (Invitrogen,

Carlsbad, CA) was diluted in the antibody dilution buffer at the ratio of 1:500 and added to the

wells for lamin. For paxilin, the secondary antibody Alexa Fluor 488 goat anti-rabbit (Invitrogen)

was diluted in the antibody dilution buffer at a ratio of 1:350 and added to the wells. For imaging

the filamentous actin for the stress fiber angle measurements, no primary antibody was added to

the well. In this case, after permeabilization, rhodamine phalloidin (Abcam) was dissolved in the

antibody dilution buffer at the ratio of 1:80 and added directly to the well. After immunochemistry,

the samples were stored in a dark place for 45 minutes followed by 3 PBS washes. Finally, the

nuclei were counterstained with 300 nM of DAPI (Invitrogen) for 15 minutes. The scaffolds were

kept hydrated in 2 ml of PBS and imaged using a 63× (water-based immersion) magnification.

Microscopy and Imaging

The cells were imaged using the AxioObserver Z.1 (with mRm camera) microscope (Carl

Zeiss, Germany) at 20× for the protrusion, spreading, force and migration studies and at 63× (water

immersion objective) magnification for the *coiling* studies. The imaging intervals used were 5

minutes for the migration study, 3 minutes for the force and spreading studies, 2 minutes for the

protrusion study and 1 second for the *coiling* study. All the videos were analyzed using ImageJ

(National Institutes of Health, Bethesda, MD).

For confocal microscopy of the immunostained samples, the cells were imaged using the

LSM 880 confocal microscope (Carl Zeiss, Germany) at 63× (water immersion objective). The

slice thickness was set to the 0.36 μm for all the images and appropriate laser powers were selected

for the different lasers.

Analysis of Biophysical Metrics

For the protrusion analysis, the maximum protrusion length was calculated as described previously. Briefly, the distance from the base fiber to the protrusion tip was first measured (L_{base}). Subsequently, the largest possible ellipse was fit along the curvature of the protrusion such that one end of the ellipse coincided with a point on the protrusion that was at a distance of $0.8 \times L_{base}$ from the base fiber. Finally, the protrusion length (L) was measured as the distance from the tip of the protrusion to the projection of the intersection of the major and minor axes of this ellipse with the protrusive fiber. The eccentricity of the protrusion (E) was calculated as follows:

$$Eccentricity = \frac{\sqrt{a^2 - b^2}}{a} \ldots (1)$$

where a and b are half of the length of the major and minor axis respectively of the ellipse fit to the protrusion. The time taken to reach the maximum protrusion length was calculated as the total time taken from the first instance that a protrusion reached a threshold minimum length of 5 μm (this threshold was established in order to discount short-lived membrane spikes and blebs) till the protrusion reached the maximum length. To calculate the average protrusion speed, the protrusion length was recorded for every frame (2 minutes). The instantaneous protrusion speed was first calculated as follows (in μm/hr):

$$Instantaneous\ Protrusion\ Speed = \frac{(L_t - L_{t-1}) \times 60}{2} \ldots (2)$$

where L_{t-1} and L_t is the protrusion length at any given frame and L_{t-1} is the protrusion length in the previous frame. Finally, the average protrusion speed was calculated as the average of all the instantaneous protrusion speeds. To determine the percentage slope changes in the protrusion

length during a protrusion cycle, the number of times the slope of the protrusion cycle changed sign from positive to negative was first recorded. This was then divided by the total number of time points in the protrusion cycle.

The *coiling* dynamics at the tip of the protrusion was calculated as previously described[212]. Briefly, the maximum *coil* width was calculated as the largest *coil* width during a *coiling* cycle

For the spreading analysis, the circularity of the cell was defined as follows:

$$Circularity = \frac{4 \times \pi \times Cell\ Area}{(Cell\ Perimeter)^2} \dots(3)$$

The value for circularity ranges from 0-1 wherein a value closer to 1 indicates a circular shape while a value closer to 0 indicates a more "straight-line" shape. The steady state circularity was determined at ninety minutes after the initial seeding of the cells as there was no significant change in the circularity beyond this time point. The time constant for each circularity profile was calculated from the exponential decay equation shown below:

$$Circularity\ (t) = \ Circularity\ (t = 0) \times e^{\frac{-t}{\tau}} \dots(4)$$

where τ represents the time constant and is calculated as the time at which:

$$Circularity\ (t) = \frac{1}{e} \times Circularity\ (t = 0) \dots(5)$$

In order to generate the actin heat maps, fluorescent images of the actin stress fibers were first converted to grayscale using ImageJ. Subsequently, the greyscale images were imported into MATLAB and the function "colormap" was used to generate heat maps. The invagination ratio for cells suspended on single fibers was quantified from the yz nucleus mid-plane projection obtained from confocal microscopy imaging as shown below:

$$Invagination\ Aspect\ Ratio = \frac{Invagination\ height}{Invagination\ width}\quad...(6)$$

For the migration analysis, cells were manually tracked using ImageJ and the x,y location of the cell centroid was recorded for every second frame (*i.e.*, every ten minutes). The instantaneous speed was then calculated as follows (in µm/hr):

$$Instantaneous\ Speed = \frac{\sqrt{(y_t - y_{t-1})^2 + (x_t - x_{t-1})^2} \times 60}{10}\quad...(7)$$

where (x_{t-1}, y_{t-1}) are the coordinates of the centroid of a cell at any given frame in µm while (x_t, y_t) are the coordinates of the centroid of the same cell three frames (*i.e.*, twelve minutes) later. The overall average speed of the cell was then calculated as the average of all the instantaneous speed values. The persistence of migration was calculated as follows:

$$Persistence = \frac{\sqrt{(y_{final} - y_{initial})^2 + (x_{final} - x_{initial})^2}}{\sum_{t=1}^{t=n} \sqrt{(y_t - y_{t-1})^2 + (x_t - x_{t-1})^2}}\quad...(8)$$

where (x_{final}, y_{final}) are the coordinates of the centroid of a cell at the last frame (n[th] frame) tracked in µm while $(x_{initial}, y_{initial})$ are the coordinates of the centroid of the same cell at the first frame tracked. The denominator is defined similar as above for the instantaneous speed. The correlation factor used for determining nucleus-centroid coupling during migration was calculated as follows:

$$Correlation\ Factor = \frac{Cov(centroid\ distance, nucleus\ distance)}{\sigma_{centroid\ distance}\sigma_{nucleus\ distance}}\quad...(9)$$

where $Cov(centroid\ distance, nucleus\ distance)$ represents the covariance of the centroid distance and nucleus distance and σ represents the standard deviation. The Shapiro-Wilks normality test was used to ensure the normal distribution of data before calculating the correlation

factor. To determine the average change in area during the migration period, the magnitude of the difference in area was calculated between every two frames (i.e. 10 minutes) and the average of all these differences was taken. A similar approach was followed to calculate the average changes in both perimeter and circularity.

Force Model for Nanonet Force Microscopy

In order to quantify the forces from the fiber deflections, the fiber deflection was tracked for three randomly selected, consecutive frames and was analyzed in MATLAB (2017a) using our previously reported methods [157,213,217]. Briefly, the ~135 nm or ~500 nm diameter, horizontal force fibers were modeled as beams with fixed-fixed boundary conditions as they were fused to larger diameter, strut-like, vertical base fibers at either end. A custom finite element model was used to obtain the force fiber deflection profile based on an arbitrary initial force input. Subsequently, the error between the fiber profile predicted by the model and the experimentally tracked fiber profile was minimized using an optimization frame while simultaneously updating the force values iteratively. The average force was finally calculated as the average of the three consecutive frames selected.

Theoretical Model of 1D cell migration

To describe theoretically the migration of a single U251 glioblastoma cell on a linear fiber, the cell was modeled as a dynamic system and described by the following equations[270]:

$$\dot{x}_{f,b} = \frac{1}{\Gamma_{f,b}}\left(\pm\left(\frac{r}{r+r_0}\right)v_{f,b} \mp k\left(x_f - x_b - 1\right)\right)...(10)$$

$$\dot{n}_{f,b} = r\left(1 - n_{f,b}\right) - n_{f,b}\exp\left(\frac{-\left(\frac{r}{r+r_0}\right)v_{f,b}+k\left(x_f-x_b-1\right)}{f_s n_{f,b}}\right)...(11)$$

$$\dot{v}_{f,b} = -\delta\left(v_{f,b} - v_{f,b}^*\right)\dots(12)$$

where the state variables $\dot{x}_{f,b}, \dot{n}_{f,b}, \dot{v}_{f,b}$ represent the position, adhesion concentration, and actin polymerization speed at the front and back edges of the one-dimensional cell, respectively.

The parameter r represents the cell-surface adhesiveness due to the binding and unbinding of adhesions, and the parameter r_0 represents an effective saturated cell-surface adhesiveness. The parameter k represents the cell elasticity (mean cell spring constant). The parameters f_s and κ are associated with the mechanical properties of the adhesions[270]. The parameter δ represents a time scale for changes in the local actin polymerization speed.

The term $\Gamma_{f,b}$ represents the friction term which changes with respect to the direction of motion of the cell's edge, and is given by

$$\Gamma_{f,b} = \begin{cases} \frac{r}{r+r_0} & , \ \pm\dot{x}_{f,b} > 0 \\ n_{f,b}\kappa\left(\frac{\left(\frac{r}{r+r_0}\right)v_{f,b}-k(x_f-x_b-1)}{f_s n_{f,b}}\right), & \pm\dot{x}_{f,b} < 0 \end{cases} \dots(13)$$

such that the top function in (13) applies to edges that extend outwards, while the complex lower function in (13) applies to edges that retract.

The terms $v_{f,b}^*$ represent the steady state polymerization speed at the edges, and are coupled to the level of the polarity cue at the edge $\bar{c}_{f,b}$ by

$$v_{f,b} = \beta\left(\frac{1}{1+\bar{c}_{f,b}}\right)\dots(14)$$

Where β is the maximal actin treadmilling flow, which couples the steady state actin treadmilling flow to the saturated polarity cue at the cell's edge. The exponential functional form of $\bar{c}_{f,b}$ along

the cell length is dominated by an advection-diffusion process along the cell, and is fully discussed in Maiuri, et al. 2015[271].

For the construction of the phase diagram we calculate two bifurcation curves:

(1) The transition between the 'no motility' and the 'smooth motion' phases, calculated by finding a critical coupling strength β_c at which the actin polymerization speed is sufficient for the cell to become polarized. The value of β_c is determined by equating two polarization lengths which are derived from the model [270].

The first is a critical length of polarization due to the advection of the polarity cue

$$l_c = \frac{c}{\sqrt{\frac{c\beta}{D}-1}}\quad...(15)$$

where D is the diffusion coefficient of the polarity cue, and c is a dimensionless quantity which encapsulates the concentration and its saturation properties [270].

The second critical length is derived from the force balance between the actin polymerization and the cell elasticity, and is given by

$$l_p = \frac{\frac{1}{2}(1-c)+\frac{\beta}{2k}\left(\frac{r}{r+r_0}\right)+}{\sqrt{c+\frac{1}{4}\left(1-c+\frac{\beta}{k}\left(\frac{r}{r+r_0}\right)\right)^2}}\quad...(16)$$

The analytical form of β_c as a function of r is given by

$$\beta_c(r) = \frac{d^2r^2+ck(r+r_0)-F(r)+dr\left(2c^2k(r+r_0)+F(r)\right)}{2cdr^2}\quad...(17)$$

$$F(r) = \sqrt{d^2r^2 + 2c(1+2c)dkr(r+r_0) + c^2k^2(r+r_0)^2}\quad...(18)$$

(2) The second transition line between the smooth motion and the stick slip motion is a Hopf bifurcation transition line which is obtained using a continuation method with AUTO07P[272].

To calculate the persistence time we first added noise to the system (Eqs.10-12). The noise is added to the actin polymerization speed in the equations, and its value was chosen to be $\Delta v = 2$ (in dimensionless units, as β) to provide sufficient fluctuations for the cell to change its direction. The formula for the persistence time is given by

$$\tau_{persistence} = \frac{\sum Times\ between\ direction\ changes}{Number\ of\ direction\ changes} \quad ...(19)$$

Throughout the simulations the fixed parameters that were used in the model are: $c = 4$, $D = 4$, $k = 1$, $f_s = 5$, $\kappa = 20$, $r_0 = 1$ and $\delta = 100$, $r = 5$. The values that were used for the maximal actin retrograde flow are: $\beta = 4,8,12,16$.

Actin flow measurements

The Halo-tagged actin was introduced into the cells by retrovirus and the cells were labeled by 5 nM Halo-TMR (Promega) for 1 hr [273]. After replacing the medium and culturing for 4 hrs, the cells were imaged with the confocal microscope (FV1000, Olympus, with High-Sensitivity Detector). To determine the velocity of the retrograde flow, time-lapse image sequences were analyzed by kymographs using ImageJ. Moving actin features were visualized in the kymographs as streak lines. The velocity of the flow was then obtained from the slopes of these lines.

Statistics

Statistical analysis of the data was conducted using RStudio (RStudio, Boston, MA) software. The Shapiro-Wilks normality tested was used to check the normality of the data sets. Analysis of variance (ANOVA) was used to test for the statistical significance between different

data sets. The following symbols are used to represent the statistical significance levels: *<0.05, **<0.01 and ***<0.001. If there is no comparison shown between any data sets, it implies that there is no statistically significant difference between them. All the error bars represent standard error of mean. Data was acquired from multiple, independent sets of experiments.

Results:

IRSp53 depletion alters spreading dynamics on suspended fibers but not on flat 2D

In order to quantitate the role of IRSp53 at the interface of membrane dynamics and cytoskeletal contractility, we generated the IRSp53 knockout (KO) U251 glioblastoma cells (**Supplementary Figure 5.S1**) using a CRISPR/Cas9 system, as described previously [268]. We inquired if IRSp53 depletion caused any effects easily observable under a microscope. We selected a cell-spreading assay composed of suspended fibers of two diameters (high curvature ~135 nm and low curvature ~500nm) spaced at least 20μm apart to achieve spindle cell shapes attached to single fibers (**Fig. 5.1A**). We confirmed the diameters using scanning electron microscopy (SEM) (**Supplementary Figure 5.S2**). Cell spreading experiments on the suspended fibers were timed to capture spreading behavior from a rounded initial state (high circularity) to a more elongated state (low circularity) along fibers (**Fig. 5.1A, B**). We calculated the area of cells as they spread and found that on all subtrates both cell types spread at similar rates, and had smaller areas on suspended fibers (**Supplementary Figure 5.S3**). However, we observed that KO cells took longer times to achieve low circularity values on fibers (longer time constant) than the WT cells on both fiber diameters, while on flat 2D, both cell types maintained high circularities during spreading (**Fig. 5.1C**). Thus, while areal calculations were not able to distinguish differences between the two cell types, circularity metric driven by protrusive activity on fiber networks was able to clearly and quickly distinguish IRSp53 depletion effects.
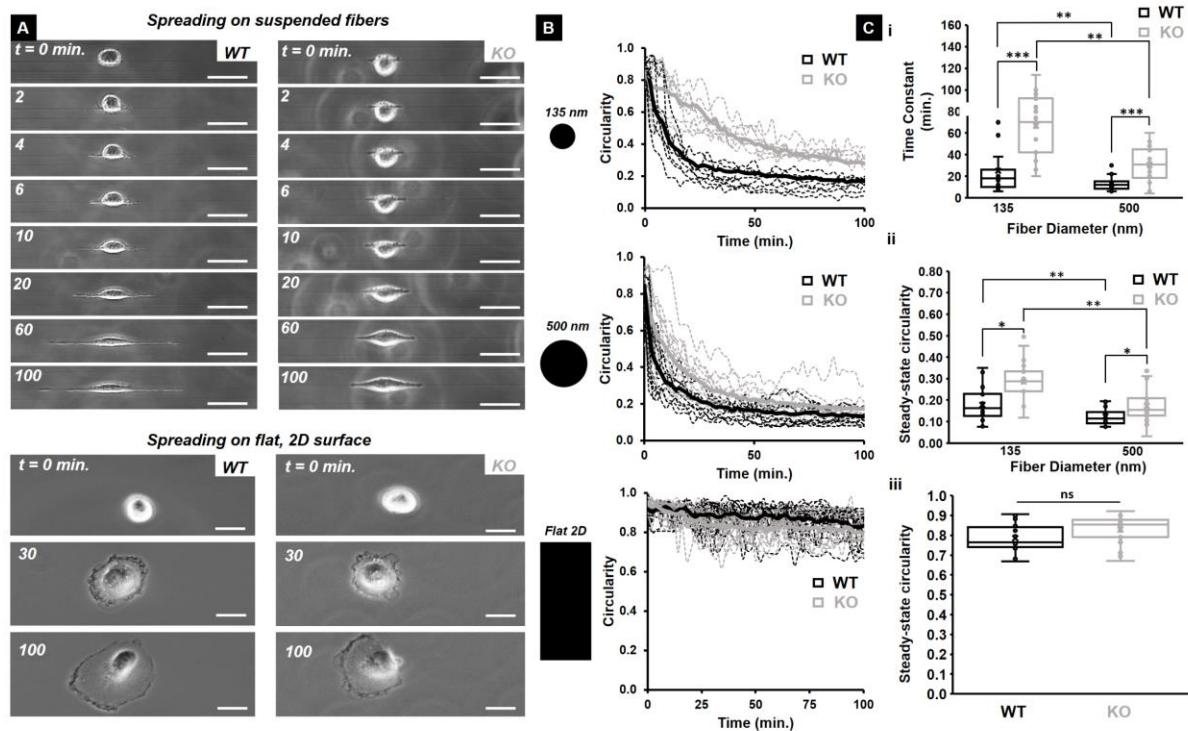
Figure 5.1: IRSp53 KO cells circularity change is slower compared to WT cells on suspended fibers. (A) Sequence of phase images showing WT cells (left panel) and KO cells (right panel) spreading on 135 nm diameter suspended fibers (top) and on flat, 2D surface (bottom). Scale bars are 20 μm. (B) Circularity profiles for both WT and KO cells on 135 nm and 500 nm diameter suspended fibers and on flat, 2D surface. Black and grey dotted lines represent the individual circularity profiles for WT and KO cells respectively while the solid lines represent average profiles. (C) Quantification of the (i) time constant and (ii) steady state circularity on both 135 nm and 500 nm diameter suspended fibers and (iii) steady state circularity on flat, 2D surface for both WT and KO cells. n =20 for all categories on all substrates. All error bars shown represent standard error of mean.

IRSp53 depletion impairs protrusion dynamics and coiling at the tips of protrusions

Since cell spreading is initiated through the extension of protrusions, and IRSp53 KO cells were taking longer times to achieve lower circularities on suspended fibers of both diameters, we inquired if protrusion dynamics were affected by IRSp53 depletion. To quantitate protrusive activity, we used our approach of depositing large diameter (~2 μm), suspended "base fibers"
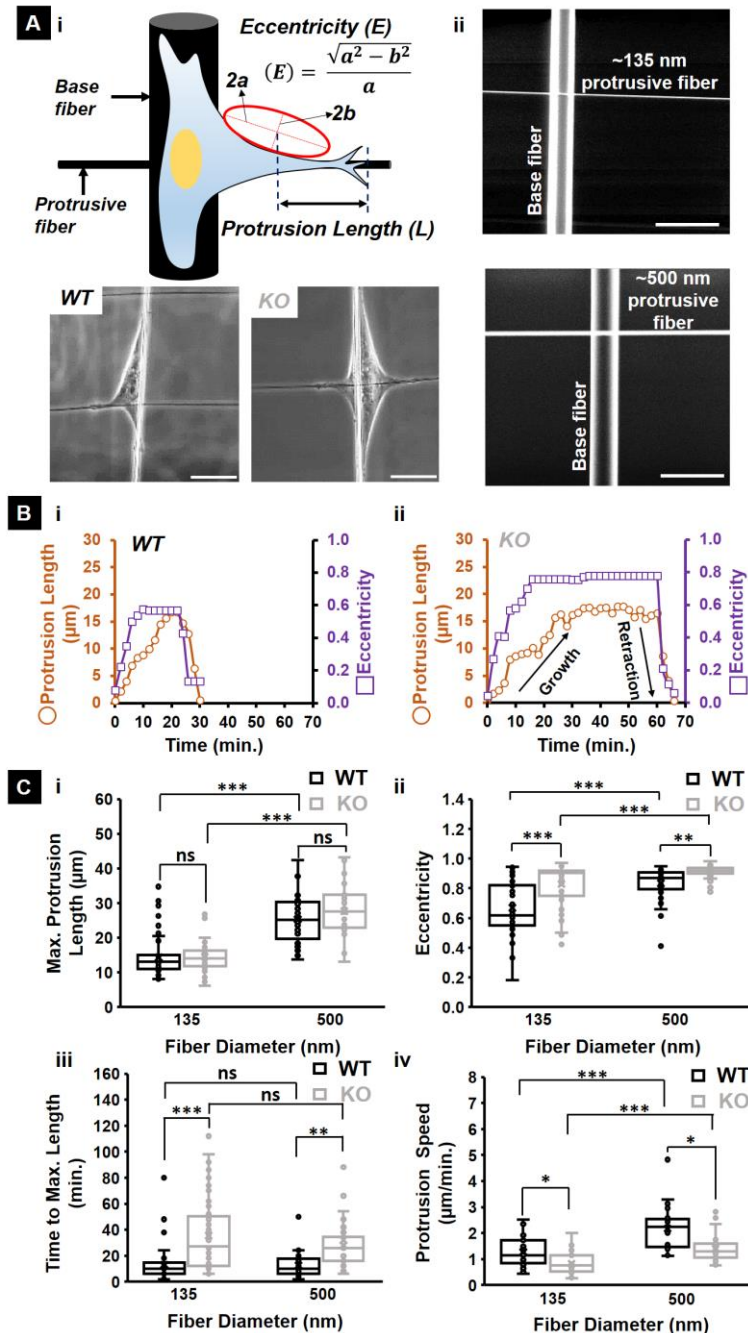
Figure 5.2: IRSp53 KO glioma cells extend protrusions slower compared to WT cells on suspended fiber networks. (A.i) Schematic showing how the protrusion length and eccentricity are quantified on the fiber networks. (A.ii) Scanning electron microscopy (SEM) images of the fiber networks manufactured using non-electrospinning STEP technique for the protrusion measurements. Scale bars are 5 μm. (A.iii) Brightfield images depicting typical protrusions formed by a WT and KO cell on 135 nm diameter protrusive fibers. Scale bars are 20 μm. Representative protrusive cycles for both WT (B.i) and KO (B.ii) cells highlighting the significant differences in protrusion formation dynamics. (C) Quantifying the differences in (i) maximum protrusion length, (ii) eccentricity at the maximum length, (iii) time taken to reach the maximum length and (iv) protrusion speed between WT and KO cells extending protrusions on both 135 nm and 500 nm diameter protrusive fibers. n values for KO cells are 50 and 38 on 135 nm and 500 nm diameters respectively and for WT cells are 50 and 32 on 135 nm and 500 nm diameters respectively. All error bars shown represent standard error of mean.

reported, this configuration allows bulk cell body migration to be constrained along with the base fiber, while individual protrusive events are elicited and studied along the protrusive fibers. To quantify the protrusion dynamics, we measured the protrusion length (L) and the eccentricity (E, a measure of the protrusion width at its base). Low eccentricity values (E< ~0.6) signified "rod-like" protrusions, while higher eccentricity values (E> ~0.8) indicate broader, "kite-shaped" protrusions. Using the combination of the protrusion length and eccentricity allowed us to quantitatively describe a "protrusion cycle." A typical protrusion cycle commences with the base of the protrusion broadening rapidly, i.e., an increase in the eccentricity, followed closely by an increase in the protrusion length until the protrusion reaches a maximum length and finally retracts back to the main cell body (**Fig. 5.2B (i, ii)**). We found no significant differences in average maximum protrusion lengths between the KO and WT cells on both fiber diameters tested (**Fig. 5.2C(i)**). However, we found that on both fiber diameters, the eccentricity (E) was significantly higher for the KO cells suggesting broader protrusions (**Fig. 5.2C(ii)**). Despite the lengths being similar, interestingly, we found that IRSP53-KO cells took a longer time to reach their maximum protrusion lengths (**Figure 5.2C(iii)**), indicating lower protrusive speeds (**Figure 5.2C(iv)**). Additionally, the KO cells exhibited significant fluctuations (extension and retraction) during their growth phase (**Supplementary Figure 5.S4**).

Previously we have demonstrated that cells can physically sense the suspended fibers by *coiling* at the protrusion tip, i.e., by "wrapping around the fiber axis" (**Fig. 5.3A(i, ii)**) [212]. Based upon our findings of delayed protrusive activity in IRSp53 KO cells, we naturally inquired if these differences translated to differences in the *coiling* cycle occurring at the protrusion tip (**Fig. 5.3B(i)**). While the maximum *coil* width increased with fiber diameter (**Fig. 5.3B(ii)**), in agreement with our previous findings[212], the maximum *coil* width was significantly lower for the KO case

(**Figure 5.3B(ii)**). Overall, we found that IRSp53 protein depletion did not impact the protrusion lengths but impaired protrusion formation dynamics and led to diminished *coil* width at the protrusion tip.
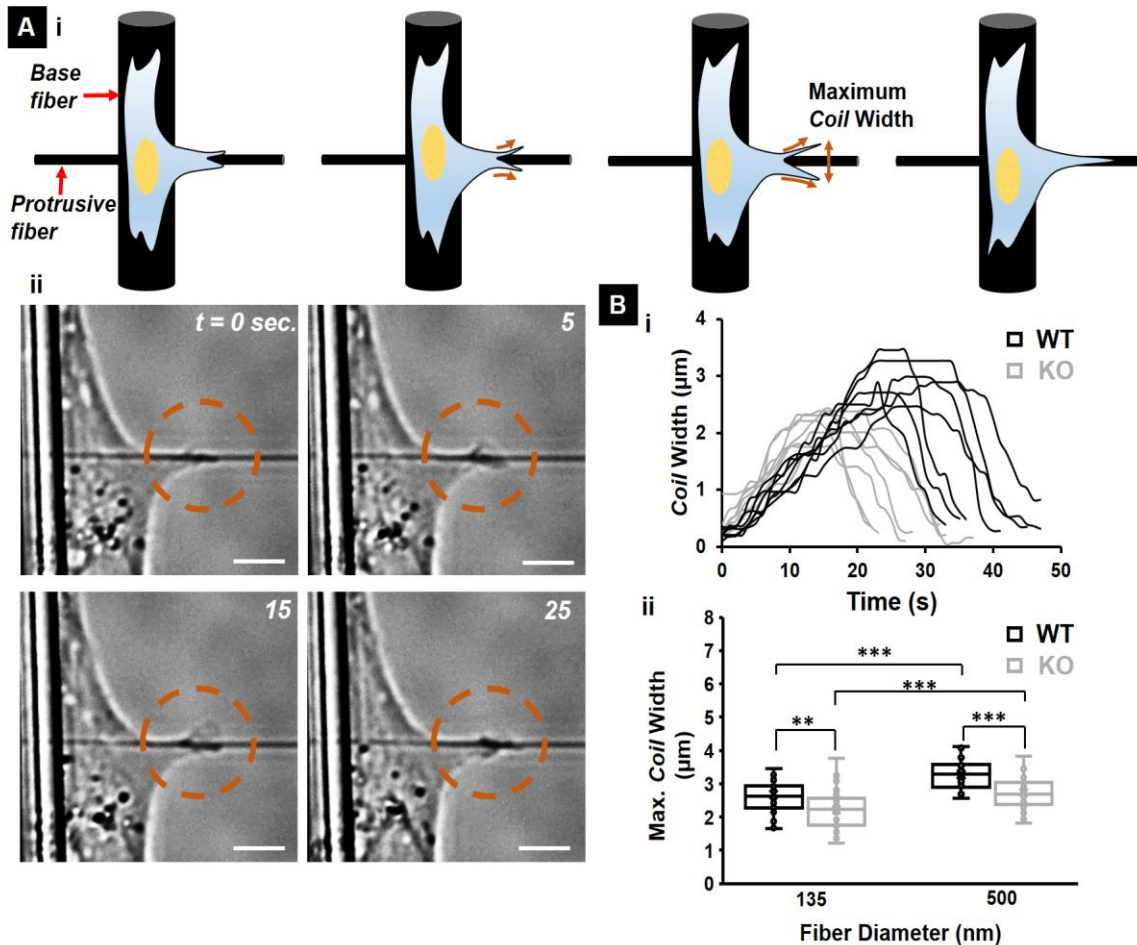
Figure 5.3: IRSp53 KO cells exhibited lower *coil* widths at the protrusion tip. (A.i) Schematic showing a typical *coiling* cycle with (ii) associated phase images for a KO cell on 135 nm diameter protrusive fiber. Scale bars are 5 μm each. Dashed orange circles highlight the *coiling* in each of the phase images. (B.i) Representative *coiling* cycles for both WT and KO cells on 135 nm diameter protrusive fiber (7 representative profiles for each case). (B.ii) maximum *coil* width highlighting the diminished *coil* width for the KO cells. n = 30 for both WT and KO cells on each of the two fiber diameters investigated. All error bars shown represent standard error of mean.

IRSp53 depletion affects actin networks and contractility

Since delayed cell spreading is associated with a loss of force exertion[274], we inquired if suspended fiber networks could quantitate loss of contractility. We used nanonet force microscopy (NFM) to quantify the forces exerted by single cells[157,218,275], as they spread on two parallel fibers of the same diameters. NFM estimates forces by establishing force vectors that originate at focal adhesion clusters (FAC) and are directed along the actin stress fibers (**Fig. 5.4A**). On suspended fibers, cells form FAC at the poles (4 in case of parallel fibers); thus, the overall contractility of the cell is estimated as $F_{cell} = \sum FAC$. Using fluorescent images of filamentous actin, we first quantified the average stress fiber angle wrt. to the fiber (θ, **Fig. 4 B(i)**) and found no difference between the KO and WT cells on both fiber diameters (**Fig. 5.4B (ii)**). However, for both cell types, the average stress fiber angle increased significantly with the increase in the fiber diameter. IRSp53 KO cells exerted ~40% less forces than WT cells (**Fig. 5.4C(i, ii)**), which, interestingly coincided with a reduction in the density of stress fibers (**Fig. 5.4D(i)**, and **Supplementary Figure 5.S5**).

Given that actomyosin contractility-driven forces have previously been implicated in modulating nuclear deformations [276], we inquired if the diminished forces exerted by the KO cells affected nuclear compression. Using confocal microscopy, we measured the nucleus thickness for both KO and WT cells. We found that the KO cells had ~30% thicker nuclei (indicating reduced nucleus compression, **Figure 5.4D(ii, iii)**). To confirm that these results were not exclusive to U251, we quantified the stress fiber angles, the exerted forces, and the nucleus thickness for gingival cancer Ca9-22 WT and KO cells (**Supplementary Figure 5.S6**). Motivated by these results on two fiber systems, we enquired if there were any differences in the nucleus shape for cells migrating on single fibers. Confocal imaging of fixed cells revealed invaginations in the
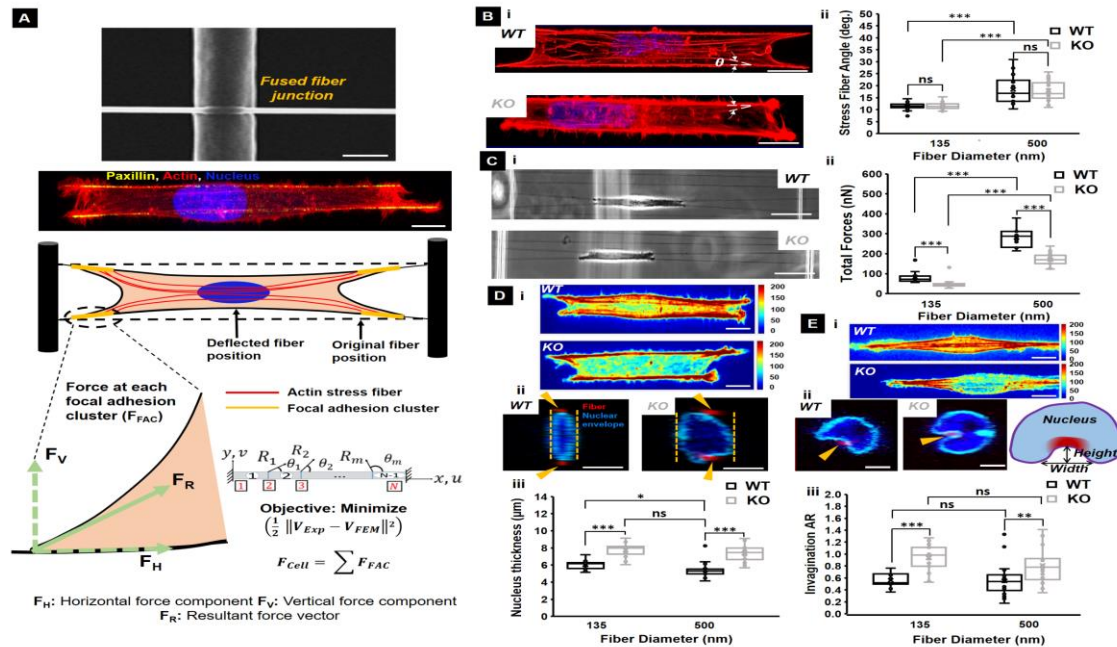
Figure 5.4: Quantifying single-cell forces using Nanonet Force Microscopy (NFM) (A) Schematic providing an overview of how forces are calculated using fused nanonets. The SEM image shows a fused fiber junction. Scale bar is 2 μm. The fluorescent image shows actin filaments in red, nucleus in blue and focal adhesion protein paxillin clustering in yellow. Scale bar is 20 μm. NFM establishes force vectors that originate from focal adhesion clusters and are directed along the actin stress fibers. An inverse finite element model minimizes the error between computational and experimental fiber deflections. (B) Representative fluorescence microscopy images of (i) WT (top) and KO (bottom) cells with actin stained in red and (ii) quantification of the stress fiber angles for both cell types on 135 and 500 nm diameter fibers. Scale bars are 10 μm. Dotted white lines in the fluorescent images depict the stress fiber angles. n values are 25 and 25 for the KO cells and 25 and 27 for WT cells on 135 nm and 500 nm diameter fibers respectively. (C) Representative phase images of (i) WT (top) and KO (bottom) cells exerting forces by pulling on suspended fibers with scale bars of 50 μm and (ii) quantification of the forces exerted for both cell types on 135 and 500 nm diameter fibers. n values are 25 for both cell types on each of the two fiber diameters investigated. (D.i) Representative heat maps in arbitrary units of the actin stress fiber distributions for the two cell types with scale bars of 10 μm. (ii) Representative confocal images of WT and KO nucleus cross-section (yz plane) with scale bar of 5 μm, and (iii) quantification of the nucleus thickness. (E.i) Representative heat maps in arbitrary units of the actin stress fiber distributions for the two cell types attached to single fibers in spindle shapes with scale bars of 10 μm, (ii) Representative confocal images of WT and KO nucleus cross-section (yz plane) with scale bar of 5 μm, and (iii) quantification of the nucleus invagination aspect ratio (AR). The schematic in E.ii shows how AR was measured. In the confocal images, the nucleus is in blue, the nuclear envelope is in cyan and the cross-section of the suspended fibers is in red shown using yellow arrowheads. n values are 18 for the nucleus thickness measurements in (D) and 25 for the invagination AR measurements in (E) for both cell types on each of the two fiber diameters investigated.

nuclear envelope at fiber-specific sites. We examined the shape of local invaginations and found

a remarkable difference between the WT and KO cells (**Fig. 5.4E(i, ii)**). The invaginations in the KO cells were sharper and deeper than the shallower and broader invaginations in WT cells. Quantifying the invagination aspect ratio (height/width) revealed an increase in the invagination aspect ratio for the KO cell nuclei.

Altogether, we found that the number density of cell-spanning stress fibers was significantly diminished in KO than WT cells. Consequently, the KO cells exerted significantly lower forces on the fibers than the WT cells, which ultimately translated to reduced nuclear compressions and altered invagination shapes at fiber-specific sites.

IRSp53 depletion causes loss of stick-slip migration and a breakdown in nucleus-cytoskeleton coupling

Given that IRSp53 depletion altered force exertion and shape of nuclei, we inquired if these changes ultimately resulted in differences in migration dynamics. Thus, we quantified single-cell migration of both KO and WT cells attached to 500 nm diameter fiber networks as well as on a flat 2D surface (which served as the control). We first investigated the morphology of migrating cells by quantifying the average circularity and aspect ratio (**Supplementary Figure 5.S7**). As expected, both KO and WT cells showed significantly lower circularity and higher aspect ratio on fibers than the flat surface, in agreement with our previous findings[215]. Next, we investigated the migration dynamics and found WT cells migrated on both substrates using the classical stick-slip mode, whereby in a migration cycle, the leading edge would continue to grow, and the trailing edge would retract in a slingshot manner. In contrast, KO cells exhibited a slower smooth and sliding migratory behavior at low persistence (**Fig. 5.5A(i, ii)**). In the stick-slip mode of migration, WT cells demonstrated synchronous displacement between the bulk cell body and the nucleus, while in KO cells, the nucleus lagged the cell body displacement during migration. To further

88

quantify this behavior, we measured the correlation factor between the nucleus and the cell body

displacements. The correlation factor ranges from -1 to 1 (see Methods for details), with values

close to 1 indicating highly correlated motion (i.e., the nucleus and cell body move in the same

direction together), values close to zero indicating no correlation, and values close to -1 indicating
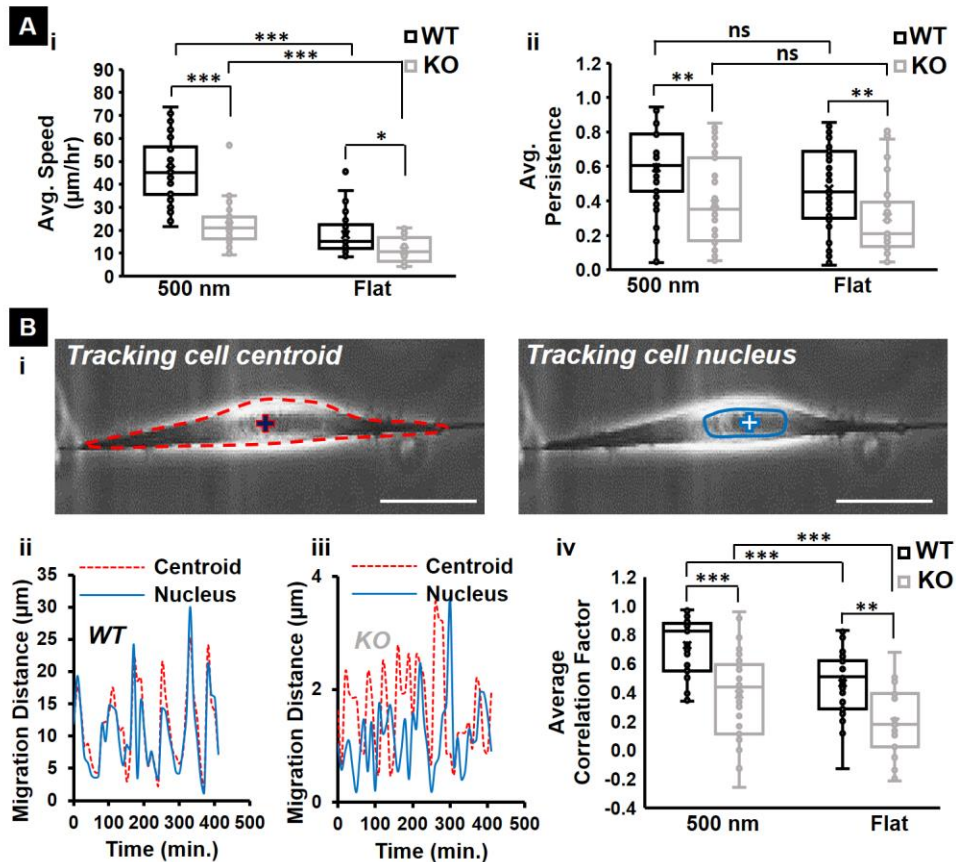
Figure 5.5: Quantifying migration behavior between IRSp53 KO and WT cells on suspended fibers and 2D flat surface. (A) Quantification of the (i) speed, and (ii) persistence of both WT and KO cells on 500 nm diameter suspended fibers and flat 2D surface (control). (B) Quantifying the synchronicity between the nucleus and cytoskeleton during migration for WT and KO cells. (i) Phase images showing that either the centroid or nucleus can be tracked during migration. Red "+" sign indicates the centroid of the cell body that is outlined by the red dashed boundary. Blue "+" sign indicates the nucleus of the same cell. Typical transient profiles of the distances migrated by the centroid (red) and nucleus (blue) for (ii) WT and (iii) KO cells. (iv) Quantification of the average correlation factor between the centroid and nucleus movement during migration for both WT and KO cells on suspended fibers and flat surface. n values for both cell types are 35 on each substrate. All error bars shown represent standard error of mean.

anticorrelated motion. We found that cells on fibers had higher correlation values indicating a strong coupling between cell body and nucleus during a migration cycle. However, depletion of IRSp53 resulted in the loss of correlation, with cells on flat showing values closer to zero, indicating almost no coupling between the nucleus and cell body during migration (**Fig. 5.5B**). In addition to the reduced coordination during migration, we also found that the KO cells exhibited fewer fluctuations in the cell shape during migration than the WT cells (**Supplementary Figure 5.S8**). Overall, we found that cells moved faster with higher persistence on fibers than on the flat substrates, and IRSp53 depletion resulted in the loss of classical stick-slip migratory mode and uncoupling of the nucleus from the cell body during migration.

Reconstituting IRSp53 recovers WT behavior

We wanted to confirm that the impaired *coiling* dynamics at the protrusion tip, reduced contractility, and hindered migration dynamics were due to depletion of IRSp53. We reconstituted IRSp53 protein (KO+IRSp53 cell line) and recovered WT protrusive behavior (**Fig. 5.6A**). Furthermore, KO+IRSp53 cells exerted similar forces, resulting in increased nuclear compression and recovery of nucleus thickness similar to WT cells (**Fig. 5.6B**). Finally, reconstituted cells recovered stick-slip migration dynamics and nuclear invagination aspect ratios similar to that of the WT cells (**Fig. 5.6C**). Altogether, we found that IRSp53 KO cells reconstituted with IRSp53 protein (KO+IRSp53 cell line) recovered WT functionalities.
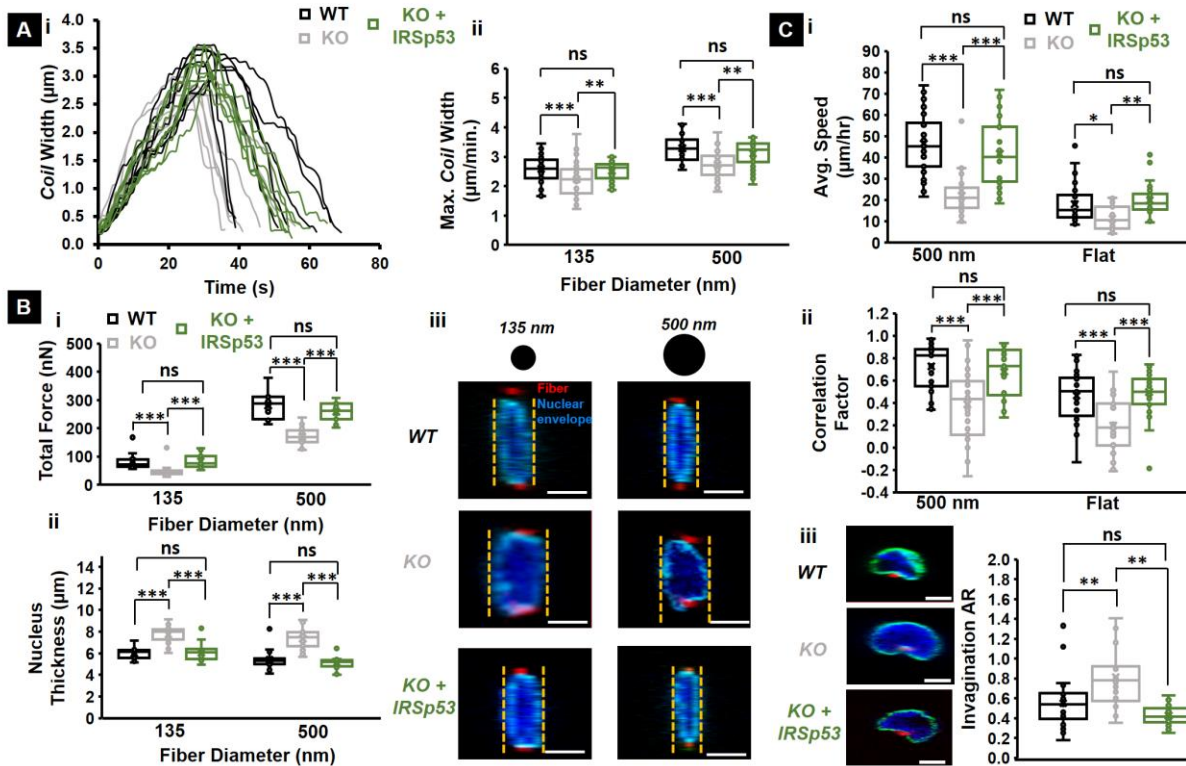
Figure 5.6: IRSp53 reconstitution in KO cells recovers WT cell function (A.i) Representative *coiling* cycle profiles for IRSp53 KO, WT and IRSp53 reconstituted cells on 500 nm diameter suspended fibers. 8 representative profiles selected for each cell category. Quantification of (A.ii) maximum *coil* width for all three cell types on both 135 nm and 500 nm diameter protrusive fibers. n values are 30 for KO cells, 30 for WT cells and 35 for IRSp53 reconstituted cells on each of the two fiber diameters tested. (B) Quantification of the (i) total forces exerted and (ii) nucleus thickness of IRSp53 KO, WT and IRSp53 reconstituted cells on both 135 nm and 500 nm diameter fibers. (B.iii) Representative confocal images showing that reconstitution of IRSp53 in IRSp53 deficient cells leads to recovery of nucleus thickness similar to the WT cells. n values for the force calculations are 25 for all cell categories on both fiber diameters tested. n values for the nucleus thickness measurements are 18 for the KO cells on both fiber diameters, 18 for the WT cells on both fiber diameters, 18 and 22 for the IRSp53 reconstituted cells on the 135 nm and 500 nm diameter fibers respectively. In the confocal images, the nucleus is in blue, the nuclear envelope is in cyan and the cross-section of the suspended fibers is in red. Scale bars are 5 μm. (C) Quantification of the (i) average speed and (ii) nucleus-cytoskeleton correlation factor during migration. n values are 35 for both WT and KO cells and 30 for the KO+IRSp53 cells on both fibers and flat substrate. (C.iii) Representative confocal microscopy images of the nucleus invagination for WT, KO and KO+IRSp53 cell nuclei and associated quantification of the invagination aspect ratio. Scale bars are all 5 µm. n = 25 for all three cell lines. All error bars shown represent standard error of mean.

Theoretical analysis captures IRSp53 effects in 1D migration and predicts actin polymerization

We wanted to inquire if we could describe the migratory behavior of IRSp53 KO cells using a theoretical model of one-dimensional cell migration[270]. The model is coarse-grained and simplified, which allows us to qualitatively relate the observed changes in migration characteristics to possible effects of IRSp53 on the microscopic parameters of the cell migration mechanism robustly.

One-dimensional elongated cells have actin polymerization activity within this model at their two opposing ends (**Fig. 5.7A**). The net actin retrograde flow in the cell, given by the difference between the flows from both ends, advects polarity cues that transiently diffuse or adsorb to the treadmilling actin[271]. For the full theoretical description, we refer the reader to the methods section. In the model, the cell length plays a crucial role: when the cell length is smaller than a critical value l_c, the actin flow can not form a large gradient of the polarity cue, and the small difference along the cell length is not sufficient to maintain a polarized cell with a finite net flow. In this case, the actin polymerization activity drives symmetric cell elongation at both ends of the cell, until the cell reaches a length l_p, where the cell's elasticity balances the protrusive forces. We plot the phase diagram of the different migration patterns of the cell, as predicted by our model (**Fig. 5.7B**)[270]. In the phase diagram, we find that a non-motile phase ($l_p < l_c$) occurs when either the cell-substrate adhesion is low (denoted by the parameter r), or when the maximal actin retrograde speed (denoted by β) is low. In both conditions, the polymerization of actin at the cell's ends does not generate protrusive forces that are sufficiently large in order to elongate the cell above the critical length l_c, which is needed in order to polarize (**Fig. 5.7C(i-iii)**). Beyond the non-motile regime, for larger r or β, we predict a regime where cells migrate smoothly (**Fig. 5.7D**), and as β increases further, the cell is predicted to transition into stick-slip migration mode (**Fig.**

5.7E,F). Comparing the theoretical model to the experimental observations of decreased protrusive speed and low force exertion, we can therefore propose that the IRSp53-KO cells have a lower maximal actin treadmilling speed (β) which places them in the slower and smooth migration or non-motile regimes (points i, ii in Fig. 5.7B, compare to experimental data in **Fig. 5.7G**), while the WT cells have a high level of β at their edges, placing them in the stick-slip migration regime (points iii, iv in Fig. 5.7B and shown with experimental data in **Fig. 5.7H**)

The model naturally explains the increased persistence in the WT cells compared to the IRSp53-KO cells (Fig. 5.5A(ii)). With the increase of β, the speed of the retrograde actin flow increases, which in turn gives rise to a larger front-back gradient of the polarity cue. Thus, cells with a higher speed of the internal actin flow have a higher persistent time, remaining robustly polarized along one direction of motion (in 1D), despite various internal noise sources; a prominent result of the Universal Coupling of Speed and Persistence (UCSP) model [270,271]. Indeed, our model predictions match the decreased persistence times observed for IRSp53-KO compared to WT cells (**Fig. 5.7I**).

We tested our prediction of WT cells having high actin polymerization at the leading edge by analyzing the retrograde flow of actin using the Halo-tagged actin introduced into the WT and KO cells. Using speckle microscopy, we generated actin flow kymographs correlating with the extent of the actin polymerization at the leading edge (**Supplementary Figure 5.S9**)[277]. We found that the retrograde actin flow was faster in the IRSp53-KO cells expressing IRSp53 than in the IRSp53-KO cells expressing GFP, both for the 2D flat surface and the fibers (**Fig. 5.7J**). Overall, our theoretical 1D model of cell migration describes the transition of slip-stick migratory behavior to a smooth low-speed migratory mode in cells depleted of IRSp53 through a loss of actin polymerization, at the cell's leading edges, which we confirmed experimentally.
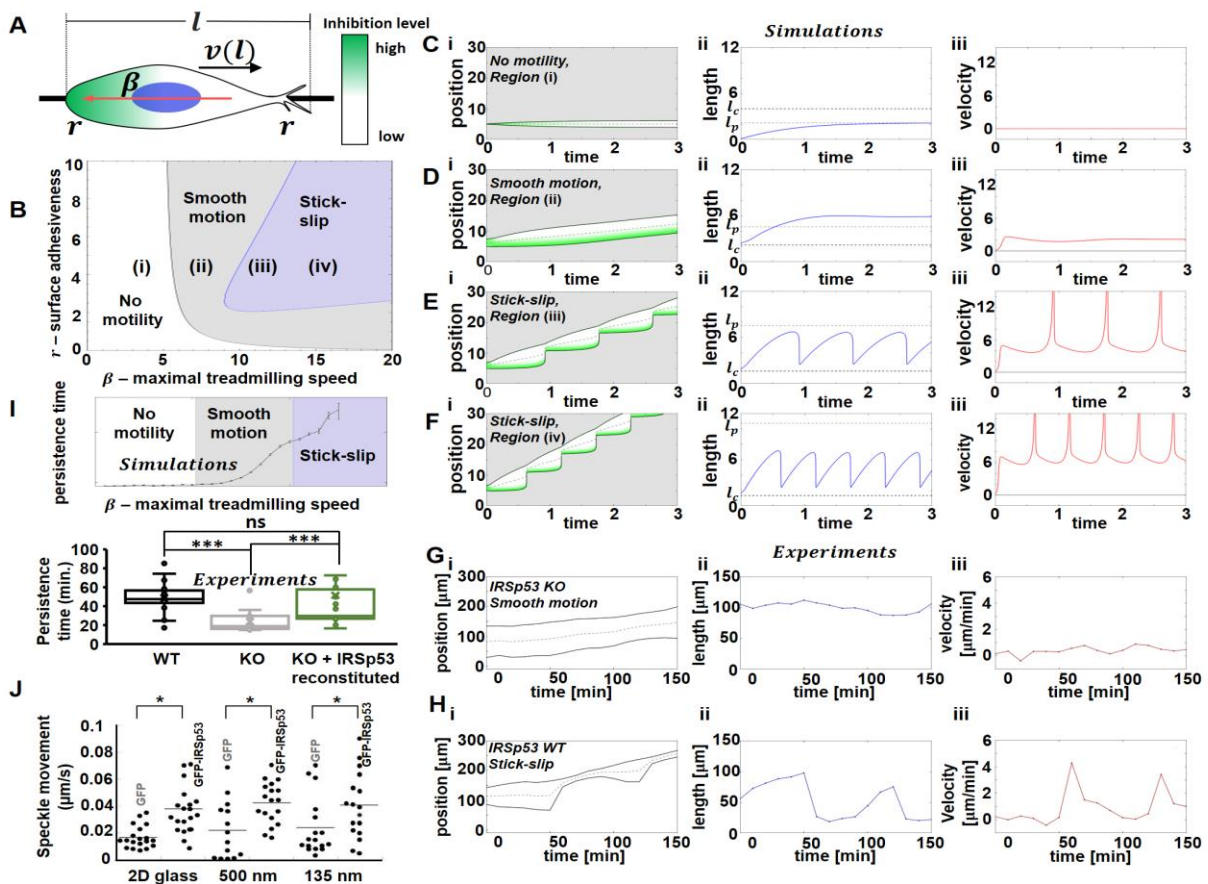
Figure 5.7: Relating the migration patterns of the IRSp53 KO and WT cells on suspended fibers to a theoretical model of one-dimensional cell migration. (A) Illustration of the theoretical model. A cell of length l migrating on a linear 1D fiber. $v(l)$ represents the velocity of the cell's center of mass, which depends on the cell length. β represents the maximal actin treadmilling flow velocity (red arrow), driven by a gradient of an inhibitory polarity cue (depicted by the colors green/white for high/low inhibition). r represents the local cell-surface adhesiveness at the cell edges, and the blue circle denotes the location of the nucleus. (B) A theoretical phase-diagram denoting the different migration patterns as function of the adhesiveness of the substrate (r) and the maximal actin treadmilling flow (β). Fixing the adhesion value, with increasing β the model predicts: (i) cells that are non-motile, elongating symmetrically (up to a maximal length l_p) but do not cross the critical length for polarization l_c shown in (C (i-iii)), (ii) migrating smoothly with speed that increases with β shown in (D (i-iii)), (iii-iv) exhibiting stick-slip migration, with speed and stick-slip frequency increasing with β shown in (E (i-iii) and F (i-iii)). For each condition we plot: (i) The kymographs, where the green/white color gradient is the polarity cue gradient (high/low) and the gray dashed line is the position of the center of mass, (ii) The length time series in blue, and l_p/l_c in dashed gray/black line, and (iii) the center-of-mass velocity in red. (G,H) The theoretical results are compared to experiments of IRSp53 KO (G) and WT (H) cells: (i) typical kymographs where the dashed gray line is the nucleus position, (ii) cell length, and (iii) nucleus velocity time series. (I) Top panel: simulation results for the persistence time as a function of the strength of the maximal actin treadmilling flow (β). The parameters used for the calculations of the model are presented in the methods section. Bottom panel: experimental measurements shows IRSp53 reconstituted KO cells recover WT persistence times (n=35 per category for cells on suspended fibers and 30 per category for cells on flat). (J) Speckle movement, where each dot represents a measure of the actin retrograde flow velocity at the leading edge of a IRSp53-KO cell expressing GFP and IRSp53-KO cell with GFP-IRSp53.

Discussion:

IRSp53, a member of the curvature sensing and curvature generating BAR family of proteins plays a central role in facilitating the bidirectional signal transduction between the cell membrane and key cytoskeletal regulatory proteins[242,244,254]. Consequently, the loss of IRSp53 has been implicated in the impairment of vital cellular functions, including protrusive activity at the cell membrane[244], recruitment of actin filaments[278], and migration dynamics[262,279,280]. In this study, we establish the role of IRSp53 in mediating protrusive activity at U-251 glioma cell extremities with force generation deep inside the cell to establish a regular "stick-slip" migration cycle in cells migrating on nanofiber matrices mimicking the *in vivo* ECM. IRSp53 related studies have primarily been conducted on flat 2D substrates. We started the study by understanding the importance of using fibrous networks by conducting cell-spreading experiments on high and low curvature fiber networks and compared them with flat 2D. We found that both WT and IRSp53 KO cells increased in area similarly on all substrates, but were smaller in size on fibers. Our findings of IRSp53 KO cells having similar spreading dynamics concur with IRSp53 deficient NIH 3T3 and C2C12 cells [281,282]. However, our studies identify that protrusion driven changes in shape during spreading signified by circularity (roundedness) was delayed on fibers but not on 2D.

Since IRSp53 KO cells exhibited delayed shape changes on fiber networks, we naturally quantified protrusion morphodynamics (protrusion length, eccentricity, speed, and fiber-specific 3D *coiling* at the protrusion tips). While the protrusion length remained unaffected by the knockout of IRSp53, the protrusions were broader (higher eccentricity), taking significantly longer times to reach the maximum lengths. Our findings contrast previous reports of protrusive filopodial impairment with depletion of IRSp53[251,252,257]. Unique to fiber matrices, we found that KO cells had decreased *coil* widths. Given that IRSp53 KO has been linked with reduced invasive potential

in cancer cells [255,264,265], this result is in agreement with our previous work, which has shown that the non-tumorigenic cells have reduced *coil* widths compared to their invasive counterparts [212].

To understand the actin stress fiber-driven force generation inside the cells, we utilized suspended nanonets (two-fiber parallel networks). Unexpectedly, we found that KO cells applied lower forces that translated to reduced nuclear compression in the KO than those in the WT cells. We found that the loss in contractility in IRSp53 cells correlated with a reduction in the number density of cell-spanning actin stress fibers, which are most effective in producing global contractile forces. We extended the study to cells attached to only single fibers. Interestingly, we found that compressive forces due to actin cytoskeleton caused invaginations inside the nucleus that ran along the nucleus's length at sites of cell-body contact with the suspended fibers. IRSp53 KO cells with low contractility were found to have narrower and deeper invaginations than the shallower and broad invaginations found in normal cells. To the best of our knowledge, our study is the first to link IRSp53 to both the force-generating machinery and resultant sculpting of the nucleus shape deep inside the cell body.

The altered protrusive dynamics and cytoskeletal contractility in the IRSp53 KO cells prompted us to inquire whether migratory patterns were affected. We found that IRSp53 KO cells exhibited a slower migration rate and lower persistence than the WT cells on both suspended fiber networks and on a flat 2D surface. Our findings are in general agreement with previous studies that have used a combination of *in vitro* [264,265] and *in vivo* assays [262] to demonstrate that depleting IRSp53 results in hindered migration dynamics[283]. However, unexpectedly, we discovered that IRSp53 KO leads to an impairment of the nucleus-cytoskeleton coupling, as evidenced by the significant reduction in the correlation between the nucleus and cell body displacement. The loss of nucleus-cytoskeleton coupling could possibly be due to the reduction of cell-spanning actin

stress fibers that constrict the nucleus. Upon reconstituting IRSp53 in the KO cells resulted in the recovery of cell contractility, nucleus centroid correlation factor and stick-slip migratory phenotype. To describe these behaviors, we used a theoretical model (UCSP) that demonstrates how polarity cues, such as myosin-II, and inhibitors of actin polymerization, affect actin polymerization and speed of the treadmilling actin in a positive feedback loop, thus, driving the spontaneous polarization of the cell. Our theoretical analysis robustly captures the migratory phenotypes observed by us; faster moving stick-slip in normal cells and slower-moving sliding in IRSp53 KO cells. The model predicted these varied migratory outcomes to rely upon the maximal actin retrograde treadmilling speed (β), with the loss of stick-slip migratory behavior due to decreased actin polymerization recruitment to the leading edge of the cells. Indeed, using speckled microscopy, we were able to verify these predictions by direct measurements of the speed of treadmilling actin at the protruding edges of the cells. Lower recruitment of actin polymerization to the cell's edges can also offer an explanation for the lower number of cell-spanning stress fibers in the IRSp53 KO cells. The ability of IRSp53 to recruit actin to the cell edges is strongly related to its curvature-sensitivity at the cell membrane.

Summary:

In conclusion, our use of ECM mimicking suspended nanofibers provides insights into cell-fiber interactions possibly occurring *in vivo* with the loss of IRSp53. Using fibers of varying diameters shows the sensitivity of cell behaviors to the curvature that are either masked or unidentifiable on flat 2D substrates. We link the actions of IRSp53 depletion at the cell peripheries with the sculpting of the nucleus deep inside the cell through the contractility of cell-spanning stress fibers. Altogether, we demonstrate that these actions work in concert to alter the migratory phenotype, thus providing new insights into the role of IRSp53 in mechanotransduction.

Supplementary Figure 5.S1: Western-blot demonstrates IRSp53 knock-out in U-251 cells. Bands of IRSp53 are shown by blue arrows.

Supplementary Figure 5.S2: Quantifying fiber diameter distribution. Histograms showing the fiber diameter distribution for (A) ~135 nm diameter, (B) ~500 nm diameter fibers used in this study. n values are 40, and 35, for the ~135 nm, and 500 nm diameters respectively.
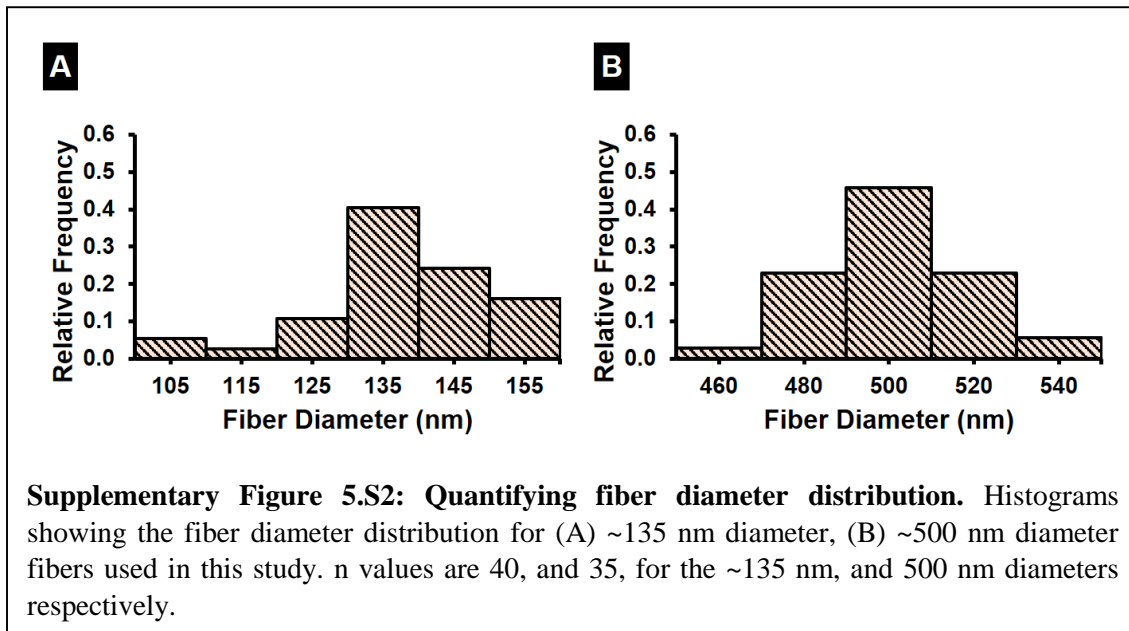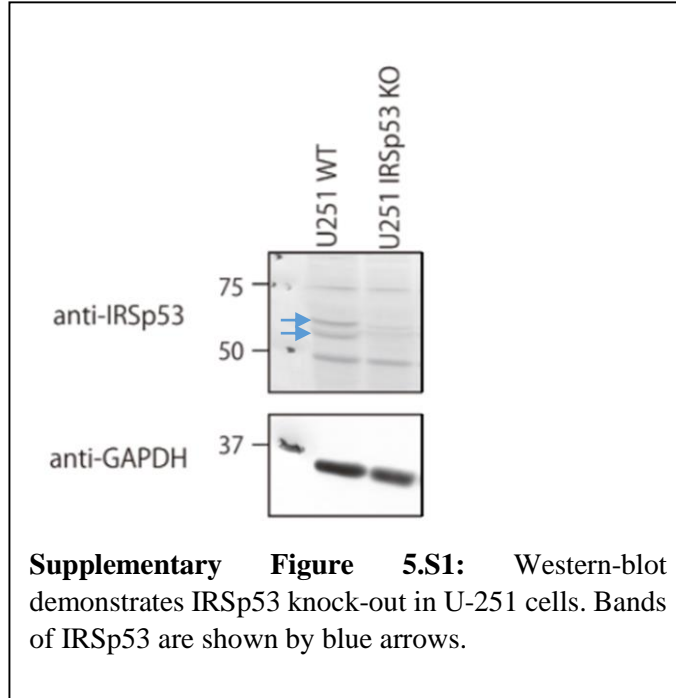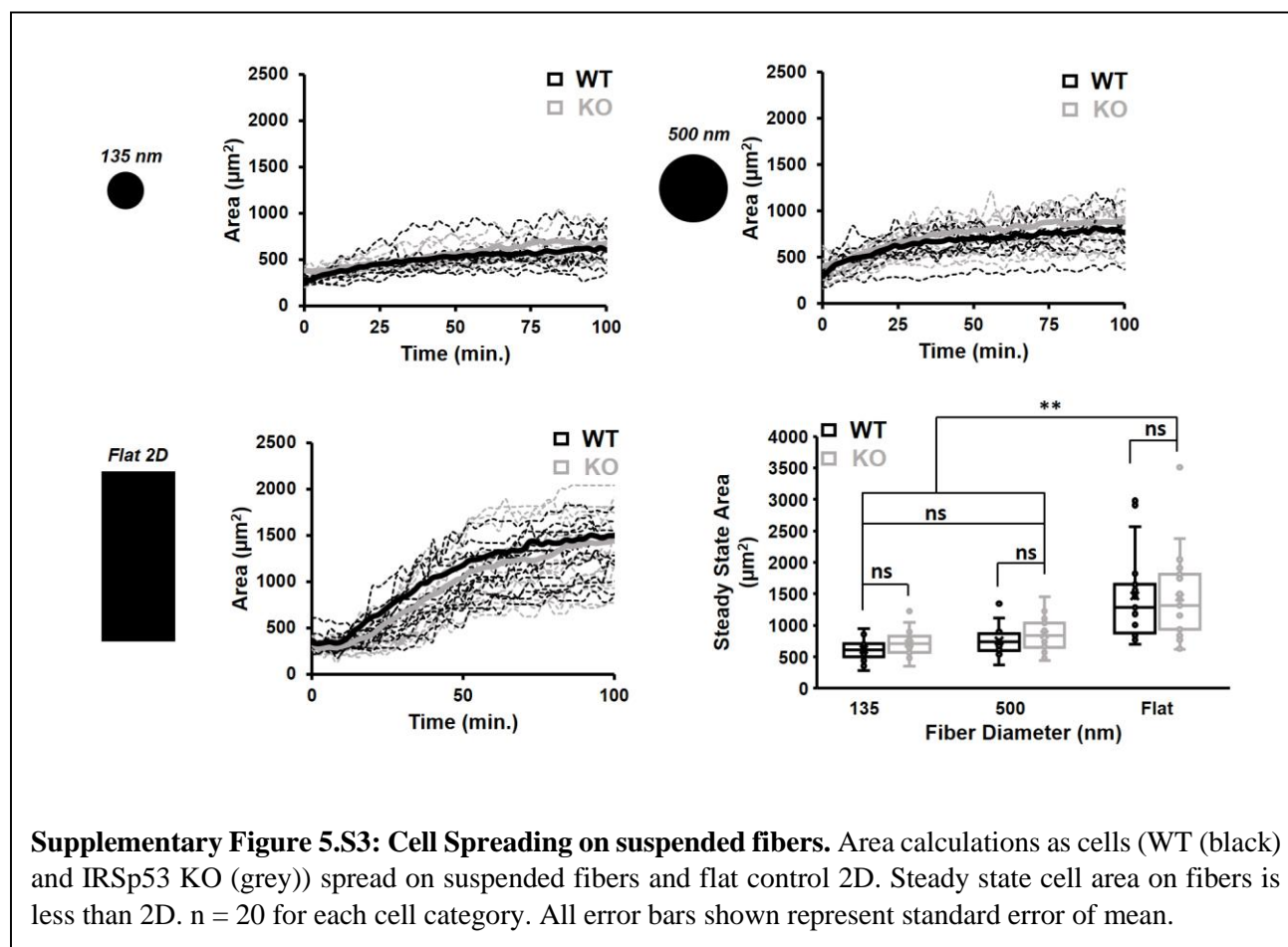
Supplementary Figure 5.S3: Cell Spreading on suspended fibers. Area calculations as cells (WT (black) and IRSp53 KO (grey)) spread on suspended fibers and flat control 2D. Steady state cell area on fibers is less than 2D. n = 20 for each cell category. All error bars shown represent standard error of mean.
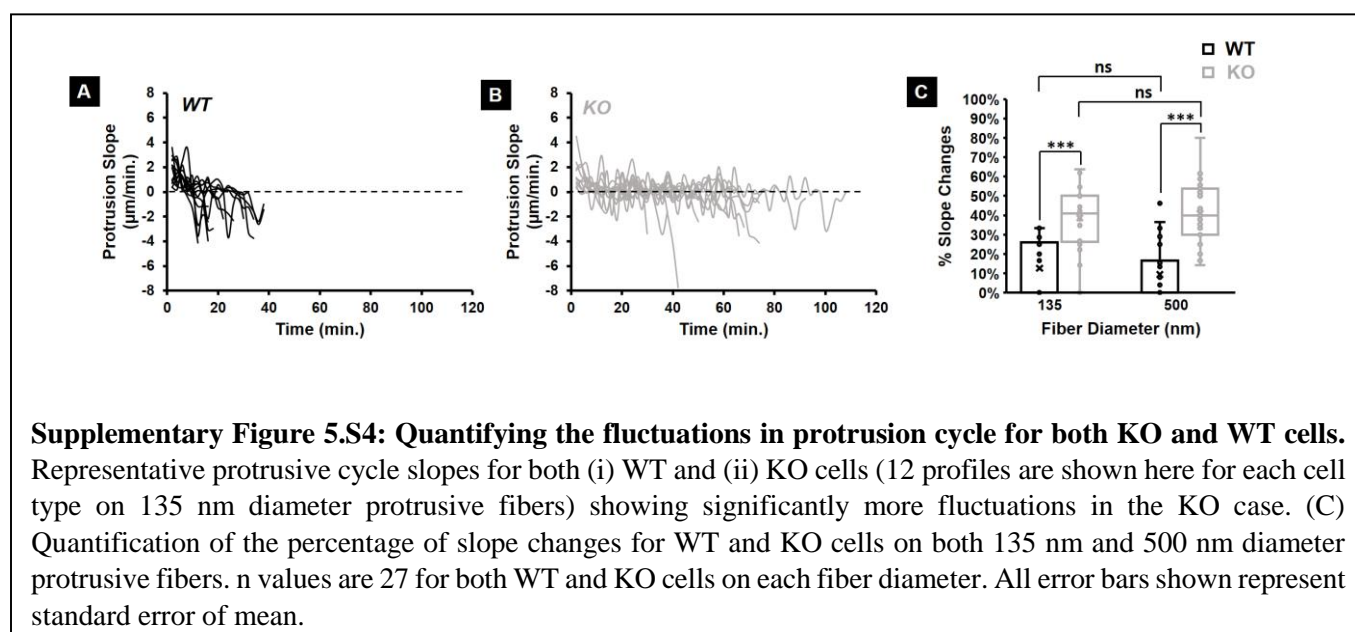
Supplementary Figure 5.S4: Quantifying the fluctuations in protrusion cycle for both KO and WT cells. Representative protrusive cycle slopes for both (i) WT and (ii) KO cells (12 profiles are shown here for each cell type on 135 nm diameter protrusive fibers) showing significantly more fluctuations in the KO case. (C) Quantification of the percentage of slope changes for WT and KO cells on both 135 nm and 500 nm diameter protrusive fibers. n values are 27 for both WT and KO cells on each fiber diameter. All error bars shown represent standard error of mean.

Supplementary Figure 5.S5: Actin stress fiber distribution. Color maps (arbitrary units) showing the actin stress fiber distribution for both WT and KO cells on 500 nm diameter suspended fibers in cells attached to two fibers (top two panels) and single fibers (bottom two panels). Scale bars are all 10 μm. In both cell shapes, KO cells have reduced number density of actin stress fibers
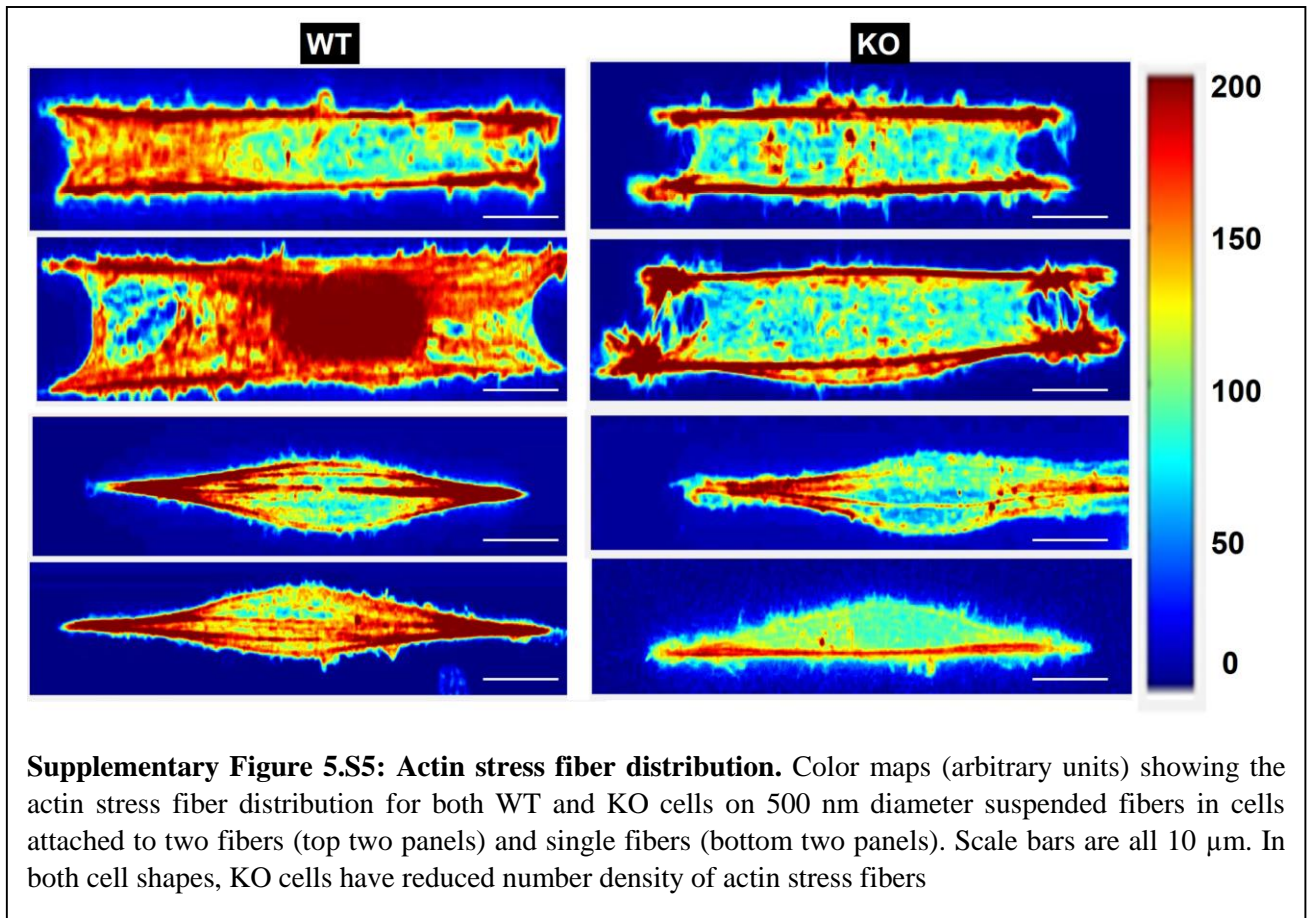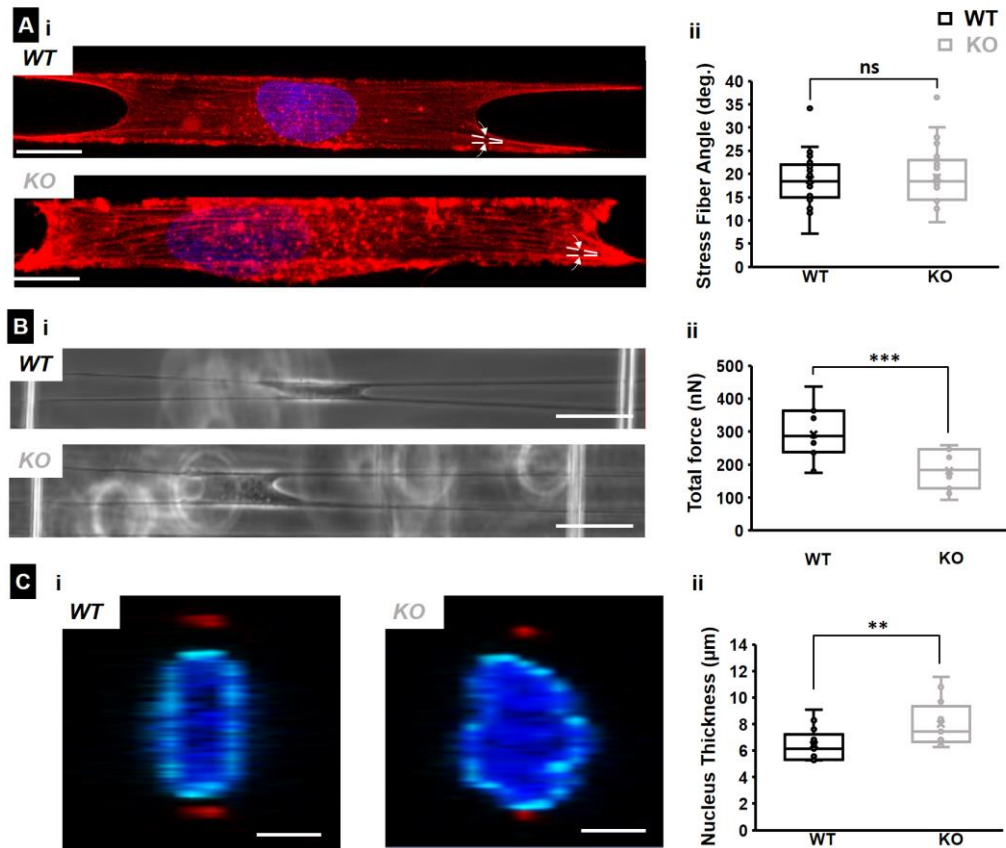
Supplementary Figure 5.S6: IRSp53 KO oral cancer cells show reduced forces and thicker nuclei compared to WT counterparts. (A) Representative fluorescence microscopy images of (i) WT (top) and KO (bottom) cells with f-actin stained in red and (ii) quantification of the stress fiber angles for both cell types on 500 nm diameter fibers. Scale bars are 10 μm. Dotted white lines in the fluorescent images depict the stress fiber angles. n values are 24 and 25 for the KO and WT cells respectively. (B) Representative phase images of (i) WT (top) and KO (bottom) cells exerting forces by pulling on suspended fibers and (ii) quantification of the forces exerted for both cell types on 500 nm diameter fibers. Scale bars are 50 μm. n values are 15 for both cell types. (C) Representative confocal images of (i) WT and KO nucleus cross-section (yz plane) on 500 nm diameter suspended fibers and (ii) quantification of the nucleus thickness. In the confocal images, the nucleus is in blue, the nuclear envelope is in cyan and the cross-section of the suspended fibers is in red. The yellow dotted lines depict the nucleus width. n values are 15 for both cell types. All error bars shown represent standard error of mean.
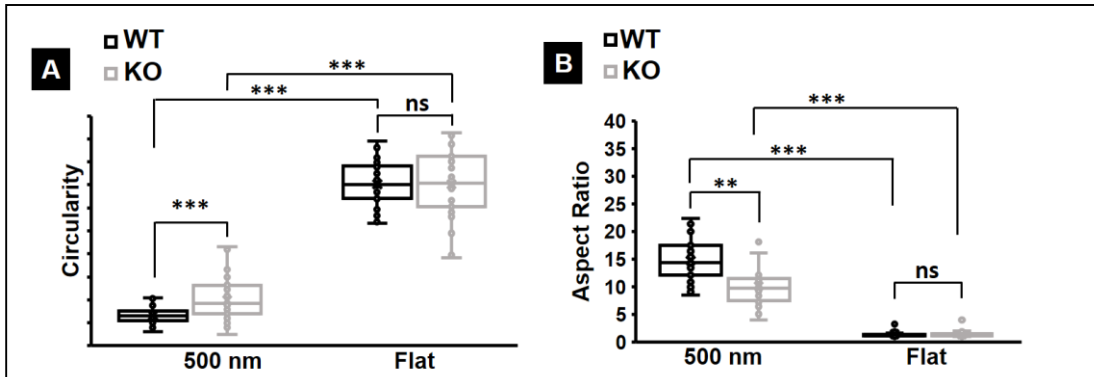
Supplementary Figure 5.S7: Quantification of average morphology metrics during migration. Average (A) circularity and (B) aspect ratio of migrating WT and IRSp53 KO cells on 500 nm diameter suspended fibers and on flat, 2D surface. n for cells on fibers is 35 for both categories and on fibers is 30 for both categories. All error bars shown represent standard error of mean.
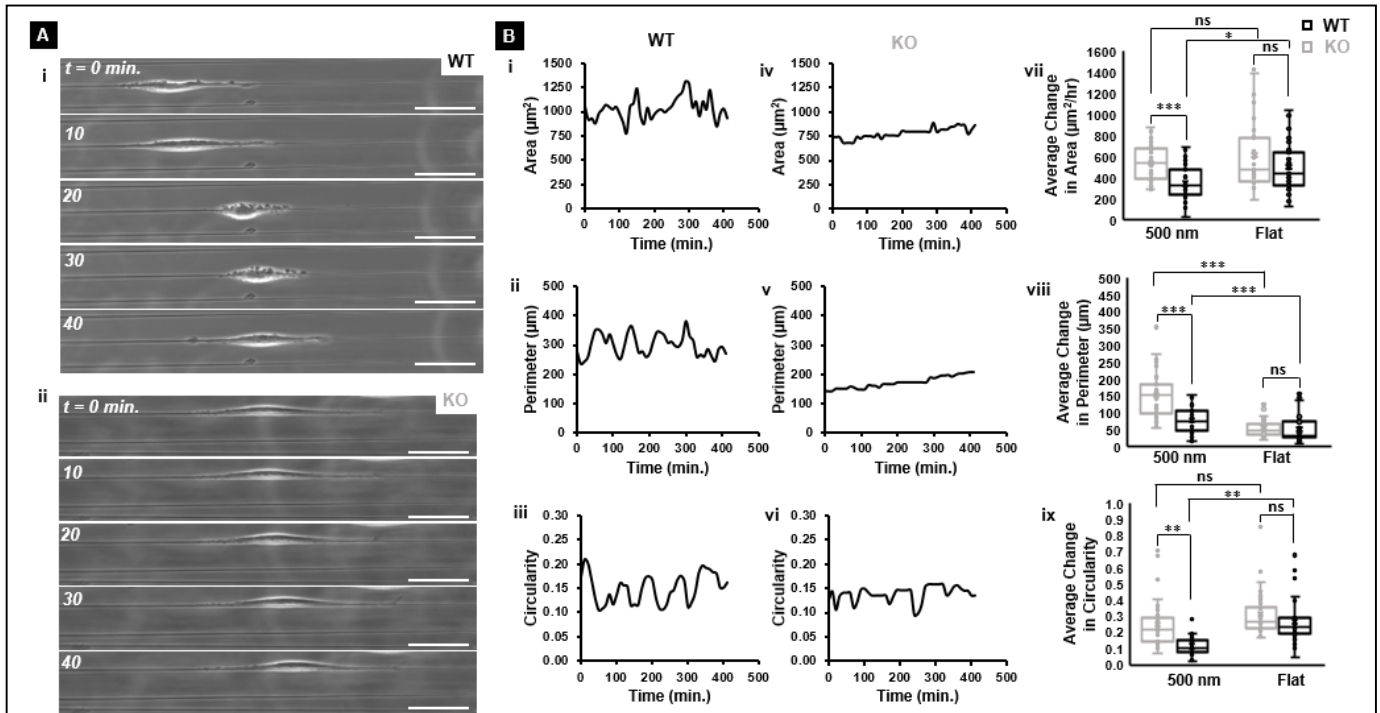
Supplementary Figure 5.S8: Quantification of the morphology changes during migration. (A) Representative phase images showing the change in cell shape during migration for (i) WT and (ii) KO cells. All scale bars are 50 μm. (B) Representative area, perimeter and circularity profiles for (i-iii) WT cells and (iv-vi) KO cells on 500 nm diameter suspended fibers. Quantification of the (vii) average change in area, (viii) average change in perimeter, and (ix) average change in the circularity of WT and KO cells on both 500 nm diameter suspended fibers and flat, 2D surfaces. n values are 35 for both cell types on the 500 nm diameter suspended fiber and 30 for both cell types on the flat surface respectively. All error bars shown represent standard error of mean.

Supplementary Figure 5.S9: Speckle microscopy of actin flow. Fluorescence speckled microscopy images of both WT and IRSp53 KO cells on both 2D glass substrate (left panel) and suspended fiber networks (right panel).
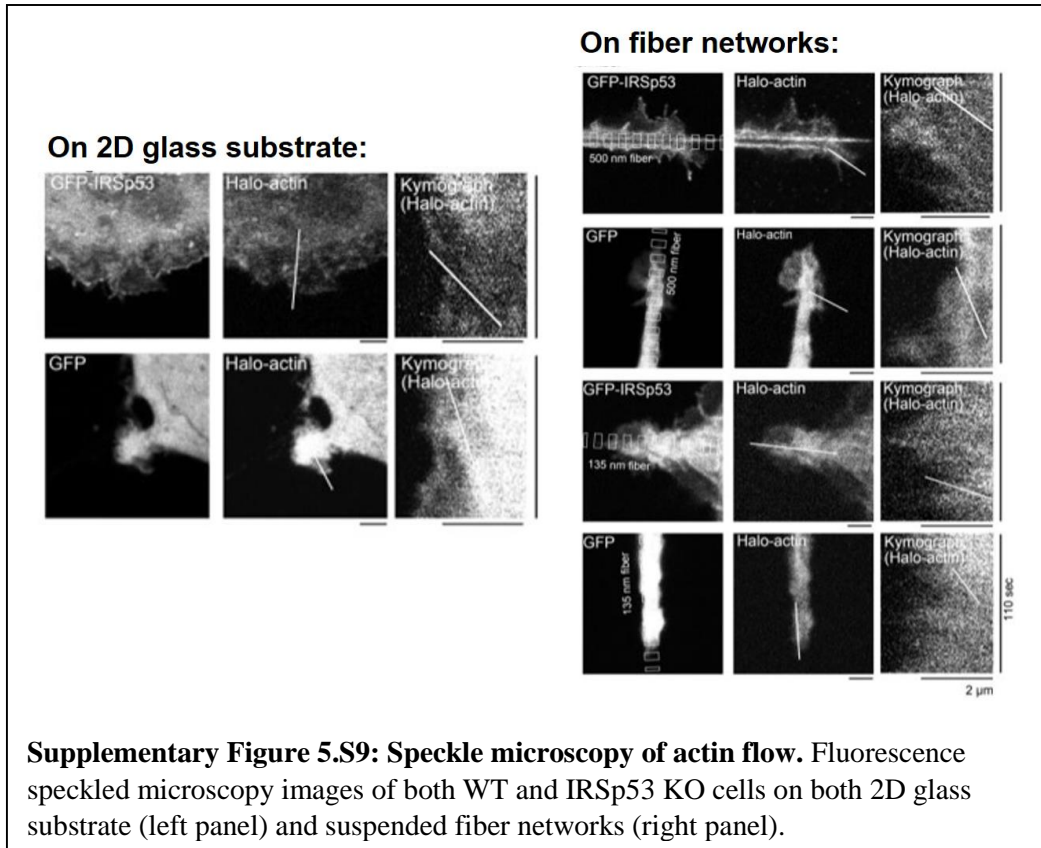
Chapter 6: Impact and Future Directions

The Bigger Picture:

The vast majority of deaths related to cancer originate from the metastasis of the cancer cells from the primary tumor to secondary and tertiary sites in the body. The contribution of the fibrous tumor microenvironment in facilitating the metastatic cascade cannot be underestimated. Over the last few decades the role of biophysical cues provided by the fibrous network (such as fiber diameter and network architecture) surrounding the primary tumor in encouraging the tumor cells to detach from the primary tumor, migrate through the stroma and intravasate into blood vessels have been gradually elucidated. However, these studies have primarily focused on the migration dynamics of the tumor cells after they have already detached from the primary tumor. How these tumor cells, initially at the primary tumor boundary, probe and sense their fibrous surroundings by extending protrusions before deciding to detach and migrate through the surrounding stroma remains unclear. Answering this question can help pave the way for developing therapeutics that can potentially arrest and hinder the metastatic cascade at a significantly nascent stage compared to current treatment regimes centered around disrupting paracrine signaling and impairing the invasive capacity of cancer cells.

In this study, we used a previously reported non-electrospinning Spinneret based Tunable Engineered Parameters (STEP) technique to manufacture suspended fiber networks with precisely tunable fiber diameter and network architecture that allowed us to systematically investigate single cell-fiber interactions and specifically, how single cancer cells sense individual fibers. We find that cancer cells sense fibers by extending protrusions and *coiling* (wrapping around the fiber axis) at the protrusion tip, a previously undescribed mechanism. Furthermore, we find that both the fiber dimension and the metastatic capacity of cancer cells modulate the *coiling* activity. Finally, we

identify a previously undescribed role played by the Insulin Receptor tyrosine kinase Substrate protein of 53 kDa (IRSp53) in acting as a key adaptor protein and translating the changes at the cell membrane initiated by the protrusive activity to the underlying cytoskeletal structure by mediating cell contractility and overall migration.

The results obtained from this study offer novel perspectives regarding what fiber architectures and dimensions surrounding the primary tumor site can either promote or hinder the metastatic cascade. In the long run, this knowledge can lay the groundwork for developing drugs that specifically target the fibrous tumor microenvironment and remodel it such that the resulting architecture and fiber sizes are unfavorable for the detachment and subsequent migration of cancer cells towards the blood vessels. Additionally, this study positions the novel *coiling* mechanism as a key component towards the development of a genetic-marker independent index for predicting the invasive capacity of cancer cells. Such a "biophysical metastatic index" could offer a complementary diagnostic tool to oncologists and potentially alleviate key issues surrounding current standard of care diagnostic tools including high cost, lack of repeatability and significant time lag between testing and processing.

Future Directions:

Specific Aim 1 (Quantification of *Coiling* Morphodynamics on STEP Nanofibers)

Results obtained from this specific aim demonstrate that cells sense ECM-mimicking suspended fibers by *coiling* along the fiber axis. Furthermore, we find that metastatic cancer cells exhibit significantly enhanced *coiling* compared to their benign counterparts. This prompts the intriguing question whether *coiling*, in addition to a sensory mechanism can potentially aid in the degradation and remodeling of the surrounding matrix. If so, that might partially explain why the

more metastatic cancer cell variant demonstrates more pronounced *coiling* at the protrusion tip. To answer this question, we have done some preliminary, proof-of-concept studies in which cancer cells seeded on the suspended fiber networks have been embedded in collagen matrices. In these studies we have observed cancer cells *coiling* along both the suspended fibers as well as through the collagen gel, potentially along the axis of individual collagen fibers (**Figure 6.1**).
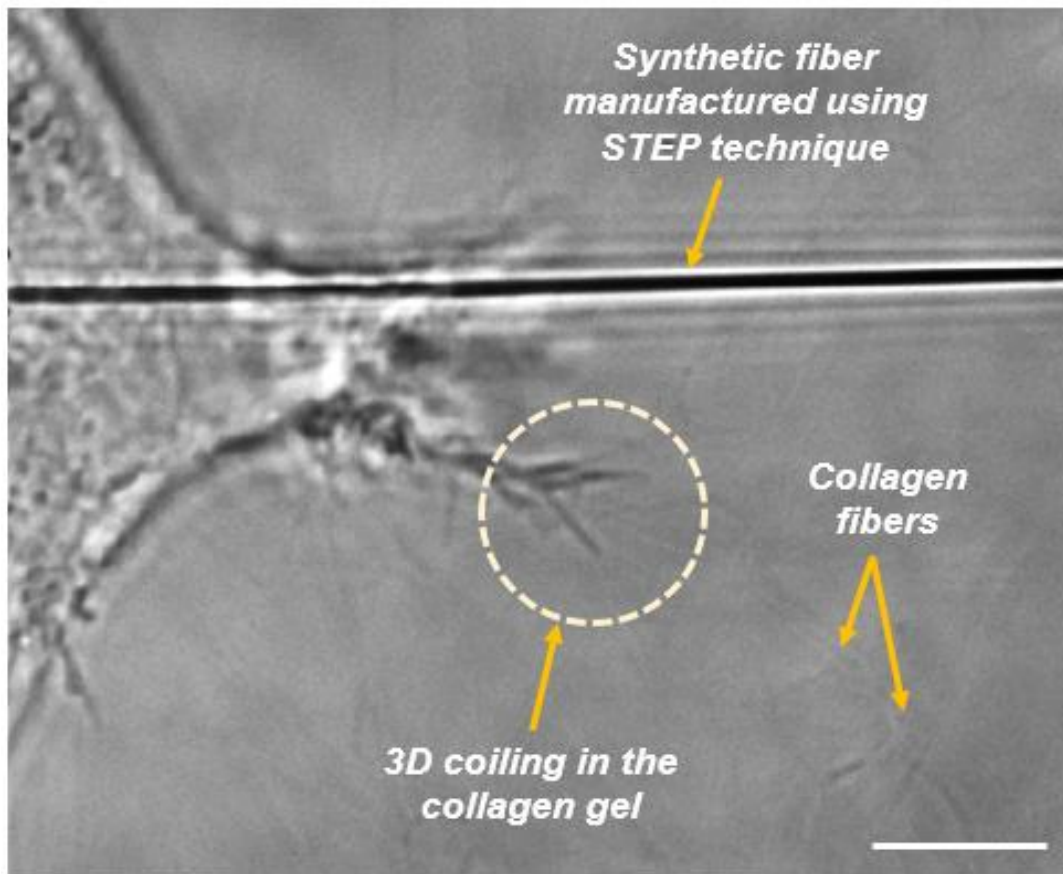
Figure 6.1: U-251 glioblastoma cell exhibiting *coiling* in the collagen matrix. The collagen concentration used here was 1 mg/ml. Scale bar is 10 μm.

In the future, second harmonic generation imaging could be employed in conjunction with fluorescently tagged collagen matrices to image and compare the degree of collagen degradation

resulting from a benign cancer cell vs it's metastatic counterpart. Furthermore, properties of the collagen matrix such as stiffness, porosity, amount of cross-linker, etc. can all be systematically tuned to identify the *coiling* response in each case. Complementary to these investigations, future studies should also look into the forces that can be exerted by single *coiling* events which might help to address the question of what extent of remodeling can a single cell undertake by *coiling*? This could help provide some answers regarding what density and number of cells might be required for degrading substrates of widely contrasting stiffness such as the blood vessels vs the bone by cancer cells as they metastasize. This could be carried out by employing atomic force microscopy (AFM) techniques in which an AFM probe can be precisely placed next to a cell that is beginning a *coiling* cycle. As the cell *coils,* the AFM tip would get deflected leading to a force read-out.

Our results in this specific aim thus far have been limited to *coiling* exhibited by single cells using orthogonally deposited fibers of contrasting curvature. Our aim with this fiber configuration was to recapitulate the highly aligned fibers at the tumor boundary reported during advanced stages of cancer progression. However, cancer cells at the tumor boundary *in vivo* are typically surrounded by a large number of cells and do not exist in isolation. To this end, we have carried out some preliminary studies in which we show that when tumor spheroids are seeded on fiber networks, cells at the tumor boundary, despite being surrounded by a large number of cells, still sense the suspended fibers by *coiling* and extending protrusions along the fiber. Thus, future studies could look into the differences in *coiling* resulting from tumor spheroids on suspended fibers in contrast with single cells. How does the presence of mechanical and chemical cues from surrounding cells influence the *coiling* activity by the tumor boundary cells?

Specific Aim 2 (Using Biophysical Metrics to Predict Metastatic Capacity)

Results obtained from this specific aim demonstrate that our suspended fiber matrices can be used to quickly and repeatably quantify biophysical metrics, including *coiling*, in cancer progression models, thus laying the groundwork for the development of alternative diagnostic tools for determining disease progression. However, these studies only consider the biophysical cues provided by the fiber network whereas the tumor microenvironment *in vivo* also provides biochemical cues to tumor cells via the paracrine signaling loop[28,284]. Thus, future studies could consider integrating different types of suspended fiber networks in microfluidic devices in order to systematically provide cancer cells with both biophysical and biochemical cues in conjunction.

The studies in this section were conducted using an ovarian cancer mouse model. In the ovarian cancer microenvironment, shear stress due to fluid flow in the peritoneal cavity plays an important role in facilitating the metastatic cascade[16]. Thus, a microfluidic device as described above, could also introduce a systematically tunable fluid flow to investigate how the biophysical metrics described earlier were altered in the presence of this additional shear stress.

<u>Specific Aim 3 (IRSp53: At the Interface Between Membrane Dynamics and Cell Contractility)</u>

Results obtained from this study describe a previously unknown role played by the Insulin Receptor tyrosine kinase Substrate protein of 53 kDa (IRSp53) in translating the effects at the cell membrane caused by protrusive activity to the underlying cytoskeletal contractility and resulting migration dynamics on ECM-mimicking suspended fibers. These studies indicate, for the first time, that knocking out IRSp53 not only impairs contractility, but also leads to lower nucleus compression (i.e. a thicker nucleus) compared to the wild type (WT) counterpart. Given that the nucleus shape can modulate which sites on the chromatin are conformationally open for transcription, future studies could investigate if IRSp53 impairment can indirectly influence gene expression in cancer cells.

Furthermore, we find that removing IRSp53 leads to a partial decoupling between the nucleus and the cytoplasm as evidenced by a decrease in the nucleus-cell body centroid correlation factor. Previous studies have highlighted the role played by the Linker of Nucleoskeleton and Cytoskeleton (LINC) complex in facilitating connections between the nucleus and cytoplasm[285,286]. Furthermore, a breakdown of the LINC complex has previously been shown to disrupt the cytoskeletal dynamics[287]. Thus, it is tempting to speculate that IRSp53 may play an indirect role in ensuring that the LINC complex continues to establish the connections between the nucleus and cytoplasm. The potential linkage between the LINC complex and IRSp53 should be investigated in future work.

References:

1. Siegel, R. L., Miller, K. D., Fuchs, H. E. & Jemal, A. Cancer Statistics, 2021. *CA. Cancer J. Clin.* doi:10.3322/CAAC.21654

2. Pathak, A. & Kumar, S. Biophysical regulation of tumor cell invasion: moving beyond matrix stiffness. *Integr. Biol. (Camb).* **3,** 267–78 (2011).

3. Guan, X. Cancer Metastases: Challenges and Opportunities. *Acta Pharm. Sin. B* **5,** 402–418 (2016).

4. Gregory, P. A., Bert, A. G., Barry, S. C. & Tsykin, A. The miR-200 family and miR-205 regulate epithelial to mesenchymal transition by targeting ZEB1 and SIP1. *Artic. Nat. Cell Biol.* (2008). doi:10.1038/ncb1722

5. Christiansen, J. J. & Rajasekaran, A. K. Reassessing Epithelial to Mesenchymal Transition as a Prerequisite for Carcinoma Invasion and Metastasis. *Cancer Res* **66,** 8319–

8345 (2006).

6.   Wolf, K. & Friedl, P. Mapping proteolytic cancer cell-extracellular matrix interfaces T.
      Clin. Exp. Metastasis **26,** 289–298 (2009).

7.   Egeblad, M. & Werb, Z. Regulation of MMP activity NEW FUNCTIONS FOR THE
      MATRIX METALLOPROTEINASES IN CANCER PROGRESSION.
      doi:10.1038/nrc745

8.   Poincloux, R., Lizárraga, F. & Chavrier, P. Matrix invasion by tumour cells: a focus on
      MT1-MMP trafficking to invadopodia. *J. Cell Sci.* **122,** (2009).

9.   Gialeli, C., Theocharis, A. D. & Karamanos, N. K. Roles of matrix metalloproteinases in
      cancer progression and their pharmacological targeting. *FEBS J.* **278,** 16–27 (2011).

10.   Shay, G., Lynch, C. C. & Fingleton, B. Moving targets: Emerging roles for MMPs in
      cancer progression and metastasis. (2015). doi:10.1016/j.matbio.2015.01.019

11.   Roussos, E. T., Condeelis, J. S. & Patsialou, A. Chemotaxis in Cancer. *Nat. Rev. Cancer*
      11, 573–587 (2011).

12.   Pantel, K. & Brakenhoff, R. H. DISSECTING THE METASTATIC CASCADE.
      doi:10.1038/nrc1370

13.   Weidner, N. Tumor angiogenesis: review of current applications in tumor prognostication.
      Semin. Diagn. Pathol. **10,** 302–13 (1993).

14.   Yokota, J. Tumor progression and metastasis. *Carcinogenesis* **21,** 497–503 (2000).

15.   Carey, S. P. *et al.* Local extracellular matrix alignment directs cellular protrusion
      dynamics and migration through Rac1 and FAK Local extracellular matrix alignment

directs cellular protrusion dynamics and migration through Rac1 and FAK. *Integr. Biol.*

Integr. Biol **8,** 821–835 (2016).

16. Novak, C., Horst, E. & Mehta, G. Review: Mechanotransduction in ovarian cancer:

    Shearing into the unknown. *APL Bioeng.* **2,** 031701 (2018).

17. Joyce, J. a & Pollard, J. W. Microenvironmental regulation of metastasis. *Nat. Rev.*

    Cancer **9,** 239–52 (2009).

18. Gritsenko, P. G., Ilina, O. & Friedl, P. Interstitial guidance of cancer invasion. *J. Pathol.*

    226, 185–99 (2012).

19. Schuppan, D. Structure of the Extracellular Matrix in Normal and Fibrotic Liver:

    Collagens and Glycoproteins. *Semin. Liver Dis.* **10,** 1–10 (1990).

20. Ushiki, T. Collagen fibers, reticular fibers and elastic fibers. A comprehensive

    understanding from a morphological viewpoint. *Arch. Histol. Cytol.* **65,** 109–26 (2002).

21. Theocharis, A. D., Skandalis, S. S., Gialeli, C. & Karamanos, N. K. Extracellular matrix

    structure ☆. *Adv. Drug Deliv. Rev.* **97,** 4–27 (2016).

22. Fernández, M. *et al.* Small-angle x-ray scattering studies of human breast tissue samples.

    Phys. Med. Biol. **47,** 577–92 (2002).

23. Sharma, P., Sheets, K., Elankumaran, S. & Nain, A. S. The mechanistic influence of

    aligned nanofibers on cell shape, migration and blebbing dynamics of glioma cells. *Integr.*

    Biol. **5,** 1036–1044 (2013).

24. Montgomery, H. *et al.* Proteomic profiling of breast tissue collagens and site-specific

    characterization of hydroxyproline residues of collagen alpha-1-(I). *J. Proteome Res.* **11,**

5890–902 (2012).

25. Zoumi, A., Yeh, A. & Tromberg, B. J. Imaging cells and extracellular matrix in vivo by using second-harmonic generation and two-photon excited fluorescence. **99,** (2002).

26. Alexander, D. C. *et al.* Orientationally invariant indices of axon diameter and density from diffusion MRI. *Neuroimage* **52,** 1374–89 (2010).

27. Paszek, M. J. & Weaver, V. M. The tension mounts: mechanics meets morphogenesis and malignancy. *J. Mammary Gland Biol. Neoplasia* **9,** 325–42 (2004).

28. Wyckoff, J. *et al. A Paracrine Loop between Tumor Cells and Macrophages Is Required for Tumor Cell Migration in Mammary Tumors. Cancer Research* **64,** (2004).

29. Walker, R. A. The complexities of breast cancer desmoplasia. *Breast Cancer Res.* **3,** 143 (2001).

30. Levental, K. R. *et al.* Matrix Crosslinking Forces Tumor Progression by Enhancing Integrin Signaling. *Cell* **139,** 891–906 (2009).

31. Shi, Q. *et al.* Rapid disorganization of mechanically interacting systems of mammary acini. doi:10.1073/pnas.1311312110

32. Goetz, J. G. *et al.* Biomechanical remodeling of the microenvironment by stromal caveolin-1 favors tumor invasion and metastasis. *Cell* **146,** 148–63 (2011).

33. Provenzano, P. P. & Keely, P. J. Mechanical signaling through the cytoskeleton regulates cell proliferation by coordinated focal adhesion and Rho GTPase signaling. *J. Cell Sci.* **124,** 1195–205 (2011).

34. Provenzano, P. P. & Keely, P. J. The role of focal adhesion kinase in tumor initiation and

progression. *Cell Adhes. Migr.* **3,** (2009).

35.   Conklin, M. W. *et al.* Aligned collagen is a prognostic signature for survival in human breast carcinoma. *Am. J. Pathol.* **178,** 1221–32 (2011).

36.   Wang, W. *et al.* Single Cell Behavior in Metastatic Primary Mammary Tumors Correlated with Gene Expression Patterns Revealed by Molecular Profiling 1,2. *CANCER Res.* **62,** 6278–6288 (2002).

37.   Condeelis, J. & Segall, J. E. Intravital imaging of cell movement in tumours. *Nat. Rev. Cancer* **3,** 921–930 (2003).

38.   Tate, M. C. & Aghi, M. K. Biology of Angiogenesis and Invasion in Glioma. *Neurotherapeutics* **6,** 447–457 (2009).

39.   Mahiphot, J., Iamsaard, S., Sawatpanich, T., Sae-Jung, S. & Khamanarong, K. A Morphometric study on subaxial cervical pedicles of thai people. *Spine (Phila. Pa. 1976).* **44,** E579–E584 (2019).

40.   Signaling, S. *et al.* Glioma Cell Migration on Three-dimensional Nanofiber Scaffolds Is Regulated by Substrate Topography and Abolished by Inhibition. *Neoplasia* **13,** 831–840 (2011).

41.   Stoletov, K. *et al.* Quantitative in vivo whole genome motility screen reveals novel therapeutic targets to block cancer metastasis. *Nat. Commun.* **9,** 2343 (2018).

42.   Friedl, P. & Wolf, K. Tumour-cell invasion and migration: Diversity and escape mechanisms. *Nature Reviews Cancer* **3,** 362–374 (2003).

43.   Friedl, P. & Alexander, S. Cancer invasion and the microenvironment: plasticity and

reciprocity. *Cell* **147,** 992–1009 (2011).

44.   Even-Ram, S. & Yamada, K. M. Cell migration in 3D matrix. *Curr. Opin. Cell Biol.* **17,** 524–32 (2005).

45.   Paňková, K., Rösel, D., Novotný, M. & Brábek, J. The molecular mechanisms of transition between mesenchymal and amoeboid invasiveness in tumor cells. *Cell. Mol. Life Sci.* **67,** 63–71 (2010).

46.   Friedl, P. & Wolf, K. Proteolytic interstitial cell migration: a five-step process. *Cancer Metastasis Rev.* **28,** 129–35 (2009).

47.   Alexandrova, A. Y., Chikina, A. S. & Svitkina, T. M. Actin cytoskeleton in mesenchymal-to-amoeboid transition of cancer cells. in *International Review of Cell and Molecular Biology* **356,** 197–256 (Elsevier Inc., 2020).

48.   Talkenberger, K., Ada Cavalcanti-Adam, E., Voss-Böhme, A. & Deutsch, A. Amoeboid-mesenchymal migration plasticity promotes invasion only in complex heterogeneous microenvironments. *Sci. Rep.* **7,** 9237 (2017).

49.   Friedl, P. Prespecification and plasticity: shifting mechanisms of cell migration. *Curr. Opin. Cell Biol.* **16,** 14–23 (2004).

50.   Sharma, P. *et al.* Aligned fibers direct collective cell migration to engineer closing and nonclosing wound gaps. *Mol. Biol. Cell* **28,** 2579–2588 (2017).

51.   Malet-Engra, G. *et al.* Collective Cell Motility Promotes Chemotactic Prowess and Resistance to Chemorepulsion. *Curr. Biol.* **25,** 242–250 (2015).

52.   Friedl, P. & Gilmour, D. Collective cell migration in morphogenesis, regeneration and

cancer. *Nat. Rev. Mol. Cell Biol.* **10,** 445–457 (2009).

53.   Pollard, T. D. & Borisy, G. G. Cellular motility driven by assembly and disassembly of actin filaments. *Cell* **112,** 453–465 (2003).

54.   Wu, C. *et al.* Arp2/3 is critical for lamellipodia and response to extracellular matrix cues but is dispensable for chemotaxis. *Cell* **148,** 973–987 (2012).

55.   Krause, M. & Gautreau, A. Steering cell migration: lamellipodium dynamics and the regulation of directional persistence. (2014). doi:10.1038/nrm3861

56.   Pollard, T. D., Blanchoin, L. & Mullins, R. D. Molecular Mechanisms Controlling Actin Filament Dynamics in Nonmuscle Cells. *Annu. Rev. Biophys. Biomol. Struct.* **29,** 545–576 (2000).

57.   Yang, C. & Svitkina, T. Filopodia initiation. *Cell Adh. Migr.* **5,** 402–408 (2011).

58.   Yang, C., Hoelzle, M., Disanza, A., Scita, G. & Svitkina, T. Coordination of Membrane and Actin Cytoskeleton Dynamics during Filopodia Protrusion. *PLoS One* **4,** e5678 (2009).

59.   Scita, G., Confalonieri, S., Lappalainen, P. & Suetsugu, S. IRSp53: crossing the road of membrane and actin dynamics in the formation of membrane protrusions. *Trends in Cell Biology* **18,** 52–60 (2008).

60.   Le Clainche, C. & Carlier, M.-F. Regulation of Actin Assembly Associated With Protrusion and Adhesion in Cell Migration. *Physiol. Rev.* **88,** (2008).

61.   Koestler, S. A. *et al.* Arp2/3 complex is essential for actin network treadmilling as well as for targeting of capping protein and cofilin. *Mol. Biol. Cell* **24,** 2861–75 (2013).

62. Svitkina, T. M. *et al.* Mechanism of filopodia initiation by reorganization of a dendritic network. *J. Cell Biol.* **160,** (2003).

63. Mattila, P. K. & Lappalainen, P. Filopodia: molecular architecture and cellular functions. *Nat. Rev. Mol. Cell Biol.* **9,** 446–454 (2008).

64. Pruyne, D. *et al.* Role of Formins in Actin Assembly: Nucleation and Barbed-End Association. *Science (80-.).* **297,** (2002).

65. Martin Pring, ‡, Marie Evangelista, §, Charles Boone, §,∥, Changsong Yang, ⊥ and & Sally H. Zigmond*, ⊥. Mechanism of Formin-Induced Nucleation of Actin Filaments. (2002). doi:10.1021/BI026520J

66. Suetsugu, S., Kurisu, S. & Takenawa, T. Dynamic Shaping of Cellular Membranes by Phospholipids and Membrane-Deforming Proteins. *Physiol. Rev.* **94,** 1219–1248 (2014).

67. Simunovic, M., Voth, G. A., Callan-Jones, A. & Bassereau, P. When Physics Takes Over: BAR Proteins and Membrane Curvature. *Trends in Cell Biology* **25,** 780–792 (2015).

68. Suetsugu, S., Toyooka, K. & Senju, Y. Subcellular membrane curvature mediated by the BAR domain superfamily proteins. *Seminars in Cell and Developmental Biology* **21,** 340–349 (2010).

69. Ahmed, S., Goh, W. I. & Bu, W. I-BAR domains, IRSp53 and filopodium formation. *Seminars in Cell and Developmental Biology* **21,** 350–356 (2010).

70. Prévost, C. *et al.* IRSp53 senses negative membrane curvature and phase separates along membrane tubules. *Nat. Commun.* **6,** 1–11 (2015).

71. Wolf, K. & Friedl, P. Mapping proteolytic cancer cell-extracellular matrix interfaces. *Clin.*

Exp. Metastasis **26,** 289–298 (2009).

72.   Gligorijevic, B. *et al.* N-WASP-mediated invadopodium formation is involved in intravasation and lung metastasis of mammary tumors. *J. Cell Sci.* **125,** 724–734 (2012).

73.   Klemke, R. L. Trespassing cancer cells: 'fingerprinting' invasive protrusions reveals metastatic culprits. *Curr. Opin. Cell Biol.* **24,** 662–9 (2012).

74.   Leong, H. S. *et al.* Invadopodia Are Required for Cancer Cell Extravasation and Are a Therapeutic Target for Metastasis. *Cell Rep.* **8,** 1558–1570 (2014).

75.   Buccione, R., Orth, J. D. & McNiven, M. A. Foot and mouth: podosomes, invadopodia and circular dorsal ruffles. *Nat. Rev.* **5,** 647–657 (2004).

76.   Yamaguchi, H. Pathological roles of invadopodia in cancer invasion and metastasis. *European Journal of Cell Biology* **91,** 902–907 (2012).

77.   Giri, A. *et al.* The Arp2/3 complex mediates multigeneration dendritic protrusions for efficient 3-dimensional cancer cell migration. *FASEB J.* **27,** 4089–99 (2013).

78.   Fraley, S. I. *et al.* Three-dimensional matrix fiber alignment modulates cell migration and MT1-MMP utility by spatially and temporally directing protrusions. *Sci. Rep.* **5,** 14580 (2015).

79.   Petrie, R. J., Gavara, N., Chadwick, R. S. & Yamada, K. M. Nonpolarized signaling reveals two distinct modes of 3D cell migration. *J. Cell Biol.* **197,** 439–455 (2012).

80.   M.McKee R. H.Colby, T. E. Long, G. L. W. Correlations of Solution Rheology With Electrospin Fiber Formation of Linear Branched Polyesters. *Macromolecules* **37,** 1760 (2004).

81. S. L.Shenoy H. L.Frisch , G. E.Wnek, W. D. B. Role of chain entanglements on fiber formation during electrospinning of polymer solutions: good solvent, non-specific-polymer interaction limit. *Polymer (Guildf).* **46,** (2005).

82. P.Gupta T. E. Long, G. L. Wilkes, C. E. Electrospinning of linear homopolymers of poly (methyl methylacrylate): expploring relationships between fiber formation, viscosity, molecular weight and concentration. *Polymer (Guildf).* **46,** (2005).

83. Agarwal, S., Greiner, A. & Wendorff, J. H. Functional materials by electrospinning of polymers. *Prog. Polym. Sci.* **38,** 963–991 (2013).

84. Ramakrishna, S., Fujihara, K., Teo, W.-E., Lim, T.-C. & Ma, Z. *An Introduction to Electrospinning and Nanofibers*. *Journal of Applied* **96,** (World Scientific Publishing Co. Pte. Ltd., 2005).

85. Zhang, Y., Lim, C. T., Ramakrishna, S. & Huang, Z.-M. Recent development of polymer nanofibers for biomedical and biotechnological applications. *J. Mater. Sci. Mater. Med.* **16,** 933–46 (2005).

86. Deitzel, J. ., Kleinmeyer, J., Harris, D. & Beck Tan, N. . The effect of processing variables on the morphology of electrospun nanofibers and textiles. *Polymer (Guildf).* **42,** 261–272 (2001).

87. Deitzel, J. Controlled deposition of electrospun poly(ethylene oxide) fibers. *Polymer (Guildf).* **42,** 8163–8170 (2001).

88. Fridrikh, S. V, Yu, J. H., Brenner, M. P. & Rutledge, G. C. Controlling the fiber diameter during electrospinning. *Phys. Rev. Lett.* **90,** 144502 (2003).

89. Huang, Z.-M., Zhang, Y.-Z., Kotaki, M. & Ramakrishna, S. A review on polymer nanofibers by electrospinning and their applications in nanocomposites. *Compos. Sci. Technol.* **63,** 2223–2253 (2003).

90. Theron, S. a., Yarin, a. L., Zussman, E. & Kroll, E. Multiple jets in electrospinning: experiment and modeling. *Polymer (Guildf).* **46,** 2889–2899 (2005).

91. Theron, S. a., Zussman, E. & Yarin, a. L. Experimental investigation of the governing parameters in the electrospinning of polymer solutions. *Polymer (Guildf).* **45,** 2017–2030 (2004).

92. Ding, B., Kimura, E., Sato, T., Fujita, S. & Shiratori, S. Fabrication of blend biodegradable nanofibrous nonwoven mats via multi-jet electrospinning. *Polymer (Guildf).* **45,** 1895–1902 (2004).

93. Kidoaki, S., Kwon, I. K. & Matsuda, T. Mesoscopic spatial designs of nano- and microfiber meshes for tissue-engineering matrix and scaffold based on newly devised multilayering and mixing electrospinning techniques. *Biomaterials* **26,** 37–46 (2005).

94. Kim, G., Cho, Y.-S. & Kim, W. D. Stability analysis for multi-jets electrospinning process modified with a cylindrical electrode. *Eur. Polym. J.* **42,** 2031–2038 (2006).

95. Kumar, A., Wei, M., Barry, C., Chen, J. & Mead, J. Controlling Fiber Repulsion in Multijet Electrospinning for Higher Throughput. *Macromol. Mater. Eng.* **295,** 701–708 (2010).

96. Srivastava, Y., Marquez, M. & Thorsen, T. Multijet Electrospinning of Conducting Nanofibers from Microfluidic Manifolds. 2–4 (2007). doi:10.1002/app

97. Varesano, A., Rombaldoni, F., Mazzuchetti, G., Tonin, C. & Comotto, R. Multi-jet nozzle electrospinning on textile substrates: observations on process and nanofibre mat deposition. *Polym. Int.* **59,** 1606–1615 (2010).

98. Li, D., Wang, Y. & Xia, Y. Electrospinning of Polymeric and Ceramic Nanofibers as Uniaxially Aligned Arrays. *Nano Lett.* **3,** 1167–1171 (2003).

99. Li, D. & Xia, Y. Fabrication of Titania Nanofibers by Electrospinning. *Nano Lett.* **3,** 555–560 (2003).

100. Carnell, L. S. *et al.* Aligned Mats from Electrospun Single Fibers. *Macromolecules* **41,** 5345–5349 (2008).

101. Hellmann, C. *et al.* High Precision Deposition Electrospinning of nanofibers and nanofiber nonwovens. *Polymer (Guildf).* **50,** 1197–1205 (2009).

102. Badrossamay, M. R., McIlwee, H. A., Goss, J. a & Parker, K. K. Nanofiber assembly by rotary jet-spinning. *Nano Lett.* **10,** 2257–61 (2010).

103. Chang, C., Limkrailassiri, K. & Lin, L. Continuous near-field electrospinning for large area deposition of orderly nanofiber patterns. *Appl. Phys. Lett.* **93,** 123111 (2008).

104. Larsen, G., Velarde-Ortiz, R., Minchow, K., Barrero, A. & Loscertales, I. G. A Method for Making Inorganic and Hybrid (Organic/Inorganic) Fibers and Vesicles with Diameters in the Submicrometer and Micrometer Range via Sol−Gel Chemistry and Electrically Forced Liquid Jets. *J. Am. Chem. Soc.* **125,** 1154–1155 (2003).

105. Viswanathamurthi, P. *et al.* Preparation and morphology of niobium oxide fibres by electrospinning. *Chem. Phys. Lett.* **374,** 79–84 (2003).

106. Dai, H., Gong, J., Kim, H. & Lee, D. A novel method for preparing ultra-fine alumina-borate oxide fibres via an electrospinning technique. *Nanotechnology* **13,** 674–677 (2002).

107. Katta, P., Alessandro, M., Ramsier, R. D. & Chase, G. G. Continuous Electrospinning of Aligned Polymer Nanofibers onto a Wire Drum Collector. *Nano Lett.* **4,** 2215–2218 (2004).

108. Li, D., Ouyang, G., McCann, J. T. & Xia, Y. Collecting Electrospun Nanofibers with Patterned Electrodes. *Nano Lett.* **5,** 913–916 (2005).

109. Zussman, E., Theron, A. & Yarin, A. L. Formation of nanofiber crossbars in electrospinning. *Applied Physics Letters* **82,** 973–975 (2003).

110. Theron, A., Zussman, E. & Yarin, A. Electrostatic field-assisted alignment of electrospun nanofibres. *Nanotechnology* **12,** 384–390 (2001).

111. Sarkar, S., Deevi, S. & Tepper, G. Biased AC Electrospinning of Aligned Polymer Nanofibers. *Macromol. Rapid Commun.* **28,** 1034–1039 (2007).

112. Sun, D., Chang, C., Li, S. & Lin, L. Near-Field Electrospinning. (2006). doi:10.1021/nl0602701

113. Brown, T. D., Dalton, P. D. & Hutmacher, D. W. Direct writing by way of melt electrospinning. *Adv. Mater.* **23,** 5651–5657 (2011).

114. Mellado, P. *et al.* A simple model for nanofiber formation by rotary jet-spinning. *Appl. Phys. Lett.* **99,** (2011).

115. Golecki, H. M. *et al.* Effect of solvent evaporation on fiber morphology in rotary jet spinning. *Langmuir* **30,** 13369–13374 (2014).

116. van der Walt, C., Hulsen, M. a., Bogaerds, a. C. B. & Anderson, P. D. Transient modeling of fiber spinning with filament pull-out. *J. Nonnewton. Fluid Mech.* **208–209,** 72–87 (2014).

117. Deravi, L. F. *et al.* Design and Fabrication of Fibrous Nanomaterials Using Pull Spinning. *Macromol. Mater. Eng.* **302,** 1–14 (2017).

118. Nain, A. S., Sitti, M., Jacobson, A., Kowalewski, T. & Amon, C. Dry spinning based spinneret based tunable engineered parameters (STEP) technique for controlled and aligned deposition of polymeric nanofibers. *Macromol. Rapid Commun.* **30,** 1406–1412 (2009).

119. Wang, J. & Nain, A. S. Suspended micro/nanofiber hierarchical biological scaffolds fabricated using non-electrospinning STEP technique. *Langmuir* **30,** 13641–13649 (2014).

120. Jana, A. *et al.* Crosshatch nanofiber networks of tunable interfiber spacing induce plasticity in cell migration and cytoskeletal response. *FASEB J.* **33,** 10618–10632 (2019).

121. Ji Wang, A. N. Exquisite Suspended Multilayer Micro/Nanofiber Hierarchical Assemblies as Biological Scaffolds. (2014).

122. Sheets, K., Wunsch, S., Ng, C. & Nain, A. S. Shape-dependent cell migration and focal adhesion organization on suspended and aligned nanofiber scaffolds. *Acta Biomater.* **9,** 7169–7177 (2013).

123. Cox, T. R. *et al.* LOX-mediated collagen crosslinking is responsible for fibrosis-enhanced metastasis. *Under Rev.* **13,** (2018).

124. Grossman, M. *et al.* Tumor cell invasion can be blocked by modulators of collagen fibril

alignment that control assembly of the extracellular matrix. *Am. Assoc. Cancer Res.* **8,** (2018).

125. Clainche, C. L. E. & Carlier, M. Regulation of actin assembly associated with protrusion and adhesion in cell migration. *Physiol. Rev.* **88,** 489–513 (2008).

126. MacHacek, M. *et al.* Coordination of Rho GTPase activities during cell protrusion. *Nature* **461,** 99–103 (2009).

127. Pollard, T. D. & Borisy, G. G. Cellular motility driven by assembly and disassembly of actin filaments. *Cell* **112,** 453–465 (2003).

128. Blanchoin, L., Boujemaa-Paterski, R., Sykes, C. & Plastino, J. Actin Dynamics, Architecture, and Mechanics in Cell Motility. *Physiol. Rev.* **94,** (2014).

129. Koons, B. *et al.* Cancer protrusions on a tightrope: nanofiber curvature contrast quantitates single protrusion dynamics. *ACS Nano* **11,** 12037–12048 (2017).

130. Friedl, P. & Wolf, K. Plasticity of cell migration: a multiscale tuning model. *J. Cell Biol.* **188,** 11–19 (2010).

131. Ponti, A., Machacek, M., Gupton, S. L., Waterman-Storer, C. M. & Danuser, G. Two distinct actin networks drive the protrusion of migrating cells. *Science (80-.).* **305,** 1782–1786 (2004).

132. Alblazi, K. & Siar, C. Cellular protrusions - lamellipodia, filopodia, invadopodia and podosomes - and their roles in progression of orofacial tumours: current understanding. *Asian Pac J Cancer Prev* **16,** 2187–2191 (2015).

133. Lo, C. M., Wang, H. B., Dembo, M. & Wang, Y. L. Cell movement is guided by the

rigidity of the substrate. *Biophys. J.* **79,** 144–152 (2000).

134. Harland, B., Walcott, S. & Sun, S. X. Adhesion dynamics and durotaxis in migrating cells. *Phys. Biol.* **8,** 015011 (2011).

135. Zigmond, S. H., Foxman, E. F. & Segall, J. E. Chemotaxis assays for eukaryotic cells. *Curr. Protoc. Cell Biol.* **Chapter 12,** Unit 12.1 (2001).

136. Wu, C. *et al.* Arp2/3 Is Critical for Lamellipodia and Response to Extracellular Matrix Cues but Is Dispensable for Chemotaxis. *Cell* **148,** 973–987 (2012).

137. Rhoads, D. S. & Guan, J.-L. Analysis of directional cell migration on defined FN gradients: Role of intracellular signaling molecules. *Exp. Cell Res.* **313,** 3859–3867 (2007).

138. Weber, M. *et al.* Interstitial dendritic cell guidance by haptotactic chemokine gradients. *Science* **339,** 328–32 (2013).

139. Linder, S. The matrix corroded: podosomes and invadopodia in extracellular matrix degradation. *Trends Cell Biol.* **17,** 107–117 (2007).

140. Weaver, A. M. Invadopodia: specialized cell structures for cancer invasion. *Clin. Exp. Metastasis* **23,** 97–105 (2006).

141. Clark, R. A. F. *et al.* Fibronectin and fibrin provide a provisional matrix for epidermal cell migration during wound reepithelialization. *J. Invest. Dermatol.* **79,** 264–269 (1982).

142. Kennedy, K. M., Bhaw-Luximon, A. & Jhurry, D. Cell-matrix mechanical interaction in electrospun polymeric scaffolds for tissue engineering: Implications for scaffold design and performance. *Acta Biomater.* **50,** 41–55 (2017).

143. Meehan, S. & Nain, A. S. Role of Suspended Fiber Structural Stiffness and Curvature on Single-Cell Migration, Nucleus Shape, and Focal-Adhesion-Cluster Length. *Biophys. J.* **107,** 2604–2611 (2014).

144. Starke, J., Maaser, K., Wehrle-Haller, B. & Friedl, P. Mechanotransduction of mesenchymal melanoma cell invasion into 3D collagen lattices: Filopod-mediated extension–relaxation cycles and force anisotropy. *Exp. Cell Res.* **319,** 2424–2433 (2013).

145. Meshel, A. S., Wei, Q., Adelstein, R. S. & Sheetz, M. P. Basic mechanism of three-dimensional collagen fibre transport by fibroblasts. *Nat. Cell Biol.* **7,** 157–164 (2005).

146. Riching, K. M. *et al.* 3D Collagen Alignment Limits Protrusions to Enhance Breast Cancer Cell Persistence. *Biophys. J.* **107,** 2546–2558 (2014).

147. Jolly, L. A. *et al.* Fibroblast-Mediated Collagen Remodeling Within the Tumor Microenvironment Facilitates Progression of Thyroid Cancers Driven by BrafV600E and Pten Loss. *Cancer Res.* **76,** (2016).

148. Metzler, R. Anomalous diffusion in membranes and the cytoplasm of biological cells. *Biophys. J.* **112,** 476a (2017).

149. Caspi, A., Granek, R. & Elbaum, M. Enhanced diffusion in active intracellular transport. *Phys. Rev. Lett.* **85,** 5655–5658 (2000).

150. Bressloff, P. & Newby, J. Stochastic models of intracellular transport. *Rev. Mod. Phys.* **85,** 136–191 (2013).

151. Wachsmuth, M., Waldeck, W. & Langowski, J. Anomalous diffusion of fluorescent probes inside living cell nuclei investigated by spatially-resolved fluorescence correlation

spectroscopy. *J. Mol. Biol.* **298,** 677–689 (2000).

152. Bronstein, I. *et al.* Transient anomalous diffusion of telomeres in the nucleus of mammalian cells. *Phys. Rev. Lett.* **103,** 018102 (2009).

153. Tolić-Nørrelykke, I. M., Munteanu, E.-L., Thon, G., Oddershede, L. & Berg-Sørensen, K. Anomalous diffusion in living yeast cells. *Phys. Rev. Lett.* **93,** 1–4 (2004).

154. Banks, D. S. & Fradin, C. Anomalous diffusion of proteins due to molecular crowding. *Biophys. J.* **89,** 2960–2971 (2005).

155. Reverey, J. F. *et al.* Superdiffusion dominates intracellular particle motion in the supercrowded cytoplasm of pathogenic Acanthamoeba castellanii. *Sci. Rep.* **5,** 11690 (2015).

156. Saxton, M. J. Anomalous diffusion due to obstacles: a Monte Carlo study. *Biophys. J.* **66,** 394–401 (1994).

157. Sheets, K., Wang, J., Zhao, W., Kapania, R. & Nain, A. S. Nanonet force microscopy for measuring cell forces. *Biophys. J.* **111,** 197–207 (2016).

158. Provenzano, P. P. *et al.* Collagen reorganization at the tumor-stromal interface facilitates local invasion. *BMC Med.* **4,** 38 (2006).

159. Zhou, X. *et al.* 3D Bioprinting a Cell-Laden Bone Matrix for Breast Cancer Metastasis Study. (2016). doi:10.1021/acsami.6b10673

160. Lelekakis, M. *et al. A novel orthotopic model of breast cancer metastasis to bone. Clinical & Experimental Metastasis* **17,** (1999).

161. Mastro, A. M., Gay, C. V & Welch, D. R. *The skeleton as a unique environment for breast*

cancer cells. *Clinical & Experimental Metastasis* **20,** (2003).

162. Senger, D. R. & Perruzzi, C. A. Cell migration promoted by a potent GRGDS-containing thrombin-cleavage fragment of osteopontin. *Biochim. Biophys. Acta - Mol. Cell Res.* **1314,** 13–24 (1996).

163. Gilles, C. *et al.* SPARC/osteonectin induces matrix metalloproteinase 2 activation in human breast cancer cell lines. *Cancer Res.* **58,** 5529–36 (1998).

164. Choi, S. *et al.* Intrafibrillar, bone-mimetic collagen mineralization regulates breast cancer cell adhesion and migration. *Biomaterials* **198,** 95–106 (2019).

165. Sheets, K., Wunsch, S., Ng, C. & Nain, A. S. Shape-dependent cell migration and focal adhesion organization on suspended and aligned nanofiber scaffolds. *Acta Biomater.* **9,** 7169–7177 (2013).

166. Ozga, M. *et al.* A systematic review of ovarian cancer and fear of recurrence. *Palliat. Support. Care* **13,** 1771–1780 (2013).

167. Torre, L. A. *et al.* Ovarian cancer statistics, 2018. *CA. Cancer J. Clin.* **68,** 284–296 (2018).

168. Dinkelspiel, H. E. *et al.* Long-term mortality among women with epithelial ovarian cancer. *Gynecol. Oncol.* **138,** 421–428 (2015).

169. Bast, R. C., Hennessy, B. & Mills, G. B. The biology of ovarian cancer: New opportunities for translation. *Nature Reviews Cancer* **9,** 415–428 (2009).

170. Cannistra, S. A. Cancer of the Ovary. *N. Engl. J. Med.* **351,** 2519–2529 (2004).

171. Doubeni, C. A., Doubeni, A. R. B. & Myers, A. E. *Diagnosis and Management of*

Ovarian Cancer. *American Family Physician* **93,** (2016).

172. Rojas, V., Hirshfield, K., Ganesan, S. & Rodriguez-Rodriguez, L. Molecular

Characterization of Epithelial Ovarian Cancer: Implications for Diagnosis and Treatment.

Int. J. Mol. Sci. **17,** 2113 (2016).

173. Jelovac, D. & Armstrong, D. K. Recent progress in the diagnosis and treatment of ovarian

cancer. *CA. Cancer J. Clin.* **61,** 183–203 (2011).

174. Goff, B. A., Mandel, L., Muntz, H. G. & Melancon, C. H. Ovarian carcinoma diagnosis.

Cancer **89,** 2068–2075 (2000).

175. Rustin, G. CA125 Response: Can it Replace the Traditional Response Criteria in Ovarian

Cancer? (2002). doi:10.1634/theoncologist.7-5-437

176. Phillips-Chavez, C., Watson, M., Coward, J. & Schloss, J. A systematic literature review

assessing if genetic biomarkers are predictors for platinum-based chemotherapy response

in ovarian cancer patients. doi:10.1007/s00228-020-02874-4

177. Tran, A. M. *et al.* A New World of Biomarkers and Therapeutics for Female Reproductive

System and Breast Cancers: Circular RNAs. *Frontiers in Cell and Developmental Biology*

8, (2020).

178. Kenny, H. A. *et al.* Mesothelial cells promote early Ovarian cancer metastasis through

fibronectin secretion. *J. Clin. Invest.* **124,** 4614–4628 (2014).

179. Lengyel, E. Ovarian cancer development and metastasis. *American Journal of Pathology*

177, 1053–1064 (2010).

180. El Aziz, M. A. A., Agarwal, K., Dasari, S. & Mitra, A. K. Productive cross-talk with the

microenvironment: A critical step in ovarian cancer metastasis. *Cancers* **11,** (2019).

181. Wilkosz, S. *et al.* A comparative study of the structure of human and murine greater omentum. *Anat. Embryol. (Berl).* **209,** 251–261 (2005).

182. Niedbala, M. J., Crickard, K. & Bernacki, R. J. Interactions of human ovarian tumor cells with human mesothelial cells grown on extracellular matrix. An in vitro model system for studying tumor cell adhesion and invasion. *Exp. Cell Res.* **160,** 499–513 (1985).

183. Iwanicki, M. P. *et al.* ovarian cancer spheroids Use Myosin-Generated Force to clear the Mesothelium. (2011). doi:10.1158/2159-8274.CD-11-0010

184. Satpathy, M., Shao, M., Emerson, R., Donner, D. B. & Matei, D. Tissue transglutaminase regulates matrix metalloproteinase-2 in ovarian cancer by modulating cAMP-response element-binding protein activity. *J. Biol. Chem.* **284,** 15390–15399 (2009).

185. Huang, S. Contributions of Stromal Metalloproteinase-9 to Angiogenesis and Growth of Human Ovarian Carcinoma in Mice. *CancerSpectrum Knowl. Environ.* **94,** 1134–1142 (2002).

186. Heath, R. M., Jayne, D. G., O'Leary, R., Morrison, E. E. & Guillou, P. J. Tumour-induced apoptosis in human mesothelial cells: A mechanism of peritoneal invasion by Fas Ligand/Fas interaction. *Br. J. Cancer* **90,** 1437–1442 (2004).

187. Friedl, P. & Wolf, K. Tumour-cell invasion and migration: diversity and escape mechanisms. *Nat. Rev. Cancer* **3,** 362–374 (2003).

188. Kraning-Rush, C. M., Califano, J. P. & Reinhart-King, C. A. Cellular traction stresses increase with increasing metastatic potential. *PLoS One* **7,** (2012).

189. Munevar, S., Wang, Y. L. & Dembo, M. Traction force microscopy of migrating normal and H-ras transformed 3T3 fibroblasts. *Biophys. J.* **80,** 1744–1757 (2001).

190. Reig, G., Pulgar, E. & Concha, M. L. Cell migration: from tissue culture to embryos. *Development* **141,** 1999–2013 (2014).

191. Plotnikov, S. V., Pasapera, A. M., Sabass, B. & Waterman, C. M. Force fluctuations within focal adhesions mediate ECM-rigidity sensing to guide directed cell migration. *Cell* **151,** 1513–1527 (2012).

192. Beningo, K. A., Dembo, M., Kaverina, I., Small, J. V. & Wang, Y. -l. L. Nascent focal adhesions are responsible for the generation of strong propulsive forces in migrating fibroblasts. *J. Cell Biol.* **153,** 881–887 (2001).

193. Zijlstra, A., Lewis, J., DeGryse, B., Stuhlmann, H. & Quigley, J. P. The Inhibition of Tumor Cell Intravasation and Subsequent Metastasis via Regulation of In Vivo Tumor Cell Motility by the Tetraspanin CD151. *Cancer Cell* **13,** 221–234 (2008).

194. Carey, S. P., Kraning-Rush, C. M., Williams, R. M. & Reinhart-King, C. a. Biophysical control of invasive tumor cell behavior by extracellular matrix microarchitecture. *Biomaterials* **33,** 4157–65 (2012).

195. Indra, I. *et al.* An in vitro correlation of mechanical forces and metastatic capacity. (2011). doi:10.1088/1478-3975/8/1/015015

196. Condeelis, J. & Segall, J. E. Intravital imaging of cell movement in tumours. *Nat. Rev. Cancer* **3,** 921–30 (2003).

197. Carlsen, J. *et al.* Ultrasound Elastography in Breast Cancer Diagnosis. *Ultraschall der*

Medizin - Eur. J. Ultrasound **36,** 550–565 (2015).

198. Pepin, K. M., Ehman, R. L. & McGee, K. P. Magnetic resonance elastography (MRE) in cancer: Technique, analysis, and applications. *Progress in Nuclear Magnetic Resonance Spectroscopy* **90–91,** 32–48 (2015).

199. Darling, E. M., Zauscher, S., Block, J. A. & Guilak, F. A thin-layer model for viscoelastic, stress-relaxation testing of cells using atomic force microscopy: Do cell properties reflect metastatic potential? *Biophys. J.* **92,** 1784–1791 (2007).

200. Phillip, J. M. *et al.* Biophysical and biomolecular determination of cellular age in humans. *Nat. Biomed. Eng.* **1,** 0093 (2017).

201. Yadav, S., Barton, M. J. & Nguyen, N. T. Biophysical properties of cells for cancer diagnosis. *Journal of Biomechanics* **86,** 1–7 (2019).

202. Nain, A. S. & Wang, J. Polymeric Nanofibers: Isodiametric Design Space and Methodology for Depositing Aligned Nanofiber Arrays in Single and Multiple Layers. *Polym. J.* **451,** 695–700 (2013).

203. Sharma, P. *et al.* Aligned Fibers Direct Collective Cell Migration to Engineer Closing and Non-Closing Wound Gaps. *Under Rev.*

204. Dobbie, J. W., Zaki, M. & Wilson, L. *Ultrastructural Studies on the Peritoneum With Special Reference to Chronic Ambulatory Peritoneal Dialysis. Medical Journal Scott Med J* **26,** (1981).

205. Thomas, N. W. Embryology and Structure of the Mesothelium. in *Pathology of the Mesothelium* 1–13 (Springer London, 1987). doi:10.1007/978-1-4471-1404-8_1

206. Roberts, P. C. *et al.* Sequential molecular and cellular events during neoplastic progression: A mouse syngeneic ovarian cancer model. *Neoplasia* **7,** 944–956 (2005).

207. Cohen, C. A., Shea, A. A., Lynn Heffron, C., Schmelz, E. M. & Roberts, P. C. The Parity-Associated Microenvironmental Niche in the Omental Fat Band Is Refractory to Ovarian Cancer Metastasis. (2013). doi:10.1158/1940-6207.CAPR-13-0227

208. Cohen, C. A., Shea, A. A., Heffron, C. L., Schmelz, E. M. & Roberts, P. C. Interleukin-12 Immunomodulation Delays the Onset of Lethal Peritoneal Disease of Ovarian Cancer. *J. Interf. Cytokine Res.* **36,** 62–73 (2016).

209. Merritt, M. A. *et al.* Gene Expression Signature of Normal Cell-of-Origin Predicts Ovarian Tumor Outcomes. *PLoS One* **8,** e80314 (2013).

210. Anderson, A. S. *et al.* Metabolic changes during ovarian cancer progression as targets for sphingosine treatment. *Exp. Cell Res.* **319,** 1431–1442 (2013).

211. Creekmore, A. L. *et al.* Changes in Gene Expression and Cellular Architecture in an Ovarian Cancer Progression Model. *PLoS One* (2011). doi:10.1371/journal.pone.0017676

212. Mukherjee, A., Behkam, B. & Nain, A. S. Cancer Cells Sense Fibers by Coiling on them in a Curvature-Dependent Manner. *iScience* **19,** 905–915 (2019).

213. Tu-Sekine, B. *et al.* Inositol polyphosphate multikinase is a metformin target that regulates cell migration. *FASEB J.* **33,** 14137–14146 (2019).

214. Koons, B. *et al.* Cancer Protrusions on a Tightrope: Nanofiber Curvature Contrast Quantitates Single Protrusion Dynamics. *ACS Nano* **11,** 12037–12048 (2017).

215. Estabridis, H. M., Jana, A., Nain, A. & Odde, D. J. Cell Migration in 1D and 2D

Nanofiber Microenvironments. *Ann. Biomed. Eng.* **46,** 392–403 (2018).

216. Jana, A. *et al.* Crosshatch nanofiber networks of tunable interfiber spacing induce plasticity in cell migration and cytoskeletal response. *FASEB J.* **33,** 10618–10632 (2019).

217. Padhi, A. *et al.* Bioenergetics underlying single-cell migration on aligned nanofiber scaffolds. *Am. J. Physiol. - Cell Physiol.* **318,** C476–C485 (2020).

218. Padhi, A. *et al.* Force-exerting perpendicular lateral protrusions in fibroblastic cell contraction. *Commun. Biol.* **3,** 1–11 (2020).

219. Webb, K., Hlady, V. & Tresco, P. A. Relationships among cell attachment, spreading, cytoskeletal organization, and migration rate for anchorage-dependent cells on model surfaces. *J. Biomed. Mater. Res.* **49,** 362–368 (2000).

220. Gupton, S. L. & Waterman-Storer, C. M. Spatiotemporal Feedback between Actomyosin and Focal-Adhesion Systems Optimizes Rapid Cell Migration. *Cell* **125,** 1361–1374 (2006).

221. Compton, S. L. E. *et al.* Adaptation of metabolism to multicellular aggregation, hypoxia and obese stromal cell incorporation as potential measure of survival of ovarian metastases. *Exp. Cell Res.* **399,** 112397 (2021).

222. Greico, J. . Progression-mediated changes in mitochondrial morphology promotes adaptation to hypoxic peritoneal conditions in serous ovarian cancer. *Front. Oncol.* (2020).

223. Meirson, T., Gil-Henn, H. & Samson, A. O. Invasion and metastasis: the elusive hallmark of cancer. *Oncogene* **39,** 2024–2026 (2020).

224. Steeg, P. S. Tumor metastasis: Mechanistic insights and clinical challenges. *Nature Medicine* **12,** 895–904 (2006).

225. Valastyan, S. & Weinberg, R. A. Tumor metastasis: Molecular insights and evolving paradigms. *Cell* **147,** 275–292 (2011).

226. Hanahan, D. & Weinberg, R. A. Hallmarks of cancer: The next generation. *Cell* **144,** 646–674 (2011).

227. Garraway, L. A. & Lander, E. S. Lessons from the cancer genome. *Cell* **153,** 17–37 (2013).

228. Lawrence, M. S. *et al.* Discovery and saturation analysis of cancer genes across 21 tumour types. *Nature* **505,** 495–501 (2014).

229. Weinstein, J. N. *et al. The Cancer Genome Atlas Pan-Cancer analysis project. Nature Publishing Group* (2013). doi:10.1038/ng.2764

230. Wu, P. H. *et al.* Single-cell morphology encodes metastatic potential. *Sci. Adv.* **6,** eaaw6938 (2020).

231. El-Deiry, W. S. *et al.* The current state of molecular testing in the treatment of patients with solid tumors, 2019. *CA. Cancer J. Clin.* **69,** caac.21560 (2019).

232. Tomar, S. *et al.* ETS1 induction by the microenvironment promotes ovarian cancer metastasis through focal adhesion kinase. *Cancer Lett.* **414,** 190–204 (2018).

233. Yamamoto, H. *et al.* Requirement for FBP17 in Invadopodia Formation by Invasive Bladder Tumor Cells. *J. Urol.* **185,** 1930–1938 (2011).

234. Coopman, P. J., Do, M. T., Thompson, E. W. & Mueller, S. C. Phagocytosis of cross-

linked gelatin matrix by human breast carcinoma cells correlates with their invasive capacity. *Clin. Cancer Res.* **4,** 507–15 (1998).

235. Papageorgis, P. *et al.* Smad Signaling Is Required to Maintain Epigenetic Silencing during Breast Cancer Progression. *Mol. Cell. Pathobiol.* **70,** 968–978 (2010).

236. Ning, Y. *et al.* Interleukin-8 is associated with proliferation, migration, angiogenesis and chemosensitivity in vitro and in vivo in colon cancer cell line models. *Int. J. Cancer* **128,** 2038–2049 (2011).

237. Liu, W., Cheng, S., Asa, S. L. & Ezzat, S. The Melanoma-Associated Antigen A3 Mediates Fibronectin-Controlled Cancer Progression and Metastasis. *Cancer Res* **68,** 8104–8116 (2008).

238. Rösel, D. *et al.* Up-Regulation of Rho/ROCK Signaling in Sarcoma Cells Drives Invasion and Increased Generation of Protrusive Forces. *Mol Cancer Res* **6,** 1410–1430 (2008).

239. Ketene, A. N., Schmelz, E. M., Roberts, P. C. & Agah, M. The effects of cancer progression on the viscoelasticity of ovarian cell cytoskeleton structures. *Nanomedicine Nanotechnology, Biol. Med.* **8,** 93–102 (2012).

240. Ketene, A. N., Roberts, P. C., Shea, A. A., Schmelz, E. M. & Agah, M. Actin filaments play a primary role for structural integrity and viscoelastic response in cells. *Integr. Biol.* **4,** 540–549 (2012).

241. Mim, C. & Unger, V. M. Membrane curvature and its generation by BAR proteins. *Trends in Biochemical Sciences* **37,** 526–533 (2012).

242. Prévost, C. *et al.* IRSp53 senses negative membrane curvature and phase separates along

membrane tubules. *Nat. Commun.* **6,** 1–11 (2015).

243. Chen, Y., Aardema, J., Misra, A. & Corey, S. BAR proteins in cancer and blood disorders
     . *Int. J. Biochem. Mol. Biol.* **3,** 198–208 (2012).

244. Scita, G., Confalonieri, S., Lappalainen, P. & Suetsugu, S. IRSp53: crossing the road of
     membrane and actin dynamics in the formation of membrane protrusions. *Trends in Cell
     Biology* **18,** 52–60 (2008).

245. Suetsugu, S. *et al.* The RAC binding domain/IRSp53-MIM homology domain of IRSp53
     induces RAC-dependent membrane deformation. *J. Biol. Chem.* **281,** 35347–35358
     (2006).

246. Gov, N. S. & Gopinathan, A. Dynamics of membranes driven by actin polymerization.
     Biophys. J. **90,** 454–69 (2006).

247. Kabaso, D. *et al.* On the role of membrane anisotropy and BAR proteins in the stability of
     tubular membrane structures. *J. Biomech.* **45,** 231–238 (2012).

248. Gov, N. S. Guided by curvature: Shaping cells by coupling curved membrane proteins and
     cytoskeletal forces. *Philosophical Transactions of the Royal Society B: Biological
     Sciences* **373,** 1–13 (2018).

249. Fošnarič, M. *et al.* Theoretical study of vesicle shapes driven by coupling curved proteins
     and active cytoskeletal forces. *Soft Matter* **15,** 5319–5330 (2019).

250. Kim, B. L. *et al.* The Cdc42 effector IRSp53 generates filopodia by coupling membrane
     protrusion with actin dynamics. *J. Biol. Chem.* **283,** 20454–20472 (2008).

251. Krugmann, S. *et al.* Cdc42 induces filopodia by promoting the formation of an

IRSp53:Mena complex. *Curr. Biol.* **11,** 1645–1655 (2001).

252. Disanza, A. *et al.* Regulation of cell shape by Cdc42 is mediated by the synergic actin-bundling activity of the Eps8-IRSp53 complex. *Nat. Cell Biol.* **8,** 1337–1347 (2006).

253. Sahari, A., Traore, M. A., Scharf, B. E. & Behkam, B. Directed Transport of Bacteria-Based Drug Delivery Vehicles: Bacterial Chemotaxis Dominates Particle Shape. *Biomed. Microdevices* **16,** 717–725 (2014).

254. Kast, D. J. & Dominguez, R. Mechanism of IRSp53 inhibition by 14-3-3. *Nat. Commun.* **10,** 1–14 (2019).

255. Oikawa, T. *et al.* IRSp53 Mediates Podosome Formation via VASP in NIH-Src Cells. *PLoS One* **8,** 1–14 (2013).

256. Nakagawa, H. *et al.* IRSp53 is colocalised with WAVE2 at the tips of protruding lamellipodia and filopodia independently of Mena. *Journal of Cell Science* **116,** 2577–2583 (2003).

257. Suetsugu, S. *et al.* Optimization of WAVE2 complex-induced actin polymerization by membrane-bound IRSp53, PIP3, and Rac. *J. Cell Biol.* **173,** 571–585 (2006).

258. Miki, H., Yamaguchi, H., Suetsugu, S. & Takenawa, T. IRSp53 is an essential intermediate between Rac and WAVE in the regulation of membrane ruffling. *Nature* **408,** 732–735 (2000).

259. Takenawa, T. & Suetsugu, S. The WASP–WAVE protein network: connecting the membrane to the cytoskeleton. *Nat. Rev. Mol. Cell Biol.* **8,** 37–48 (2007).

260. Chen, Z. *et al.* Structure and control of the actin regulatory WAVE complex. *Nature* **468,**

533–538 (2010).

261. Meyen, D. *et al.* Dynamic filopodia are required for chemokine-dependent intracellular polarization during guided cell migration in vivo. *Elife* **2015,** 1–25 (2015).

262. Disanza, A. *et al.* CDC42 switches IRSp53 from inhibition of actin growth to elongation by clustering of VASP. *EMBO J.* **32,** 2735–2750 (2013).

263. Begemann, I. *et al.* Mechanochemical self-organization determines search pattern in migratory cells. *Nat. Phys.* **15,** 848–857 (2019).

264. Funato, Y. *et al.* IRSp53/Eps8 complex is important for positive regulation of Rac and cancer cell motility/invasiveness. *Cancer Res.* **64,** 5237–5244 (2004).

265. Capdevielle, C. *et al.* HDAC inhibition induces expression of scaffolding proteins critical for tumor progression in pediatric glioma: Focus on EBP50 and IRSp53. *Neuro. Oncol.* **22,** 550–562 (2020).

266. Cattaneo, M. G., Cappellini, E. & Vicentini, L. M. Silencing of Eps8 blocks migration and invasion in human glioblastoma cell lines. *Exp. Cell Res.* **318,** 1901–1912 (2012).

267. Singh, J., Pagulayan, A., Camley, B. A. & Nain, A. S. Rules of contact inhibition of locomotion for cells on suspended nanofibers. *Proc. Natl. Acad. Sci.* **118,** 1–9 (2021).

268. Mashiko, D. *et al.* Generation of mutant mice by pronuclear injection of circular plasmid expressing Cas9 and single guided RNA. *Sci. Rep.* **3,** 1–6 (2013).

269. Hanawa-Suetsugu, K. *et al.* Phagocytosis is mediated by two-dimensional assemblies of the F-BAR protein GAS7. *Nat. Commun.* **10,** 1–13 (2019).

270. Ron, J. E., Monzo, P., Gauthier, N., Voituriez, R. & Gov, N. S. One dimensional cell

motility patterns. *Phys. Rev. Res.* **2,** 1–27 (2020).

271. Maiuri, P. *et al.* Actin flows mediate a universal coupling between cell speed and cell persistence. *Cell* **161,** 374–386 (2015).

272. Doedel, E. *et al.* AUTO-07P: Continuation and bifurcation software for ordinary differential equations. 1–247 (2007).

273. Minegishi, T. *et al.* Shootin1b Mediates a Mechanical Clutch to Produce Force for Neuronal Migration. *Cell Rep.* **25,** 624–639 (2018).

274. Dubin-Thaler, B. J. *et al.* Quantification of Cell Edge Velocities and Traction Forces Reveals Distinct Motility Modules during Cell Spreading. *PLoS One* **3,** 1–15 (2008).

275. Graybill, P. M., Jana, A., Kapania, R. K., Nain, A. S. & Davalos, R. V. Single Cell Forces after Electroporation. *ACS Nano* **15,** 2554–2568 (2021).

276. Friedl, P., Wolf, K. & Lammerding, J. Nuclear mechanics during cell migration. *Current Opinion in Cell Biology* **23,** 55–64 (2011).

277. Miller, C. M., Korkmazhan, E. & Dunn, A. R. Extraction of accurate cytoskeletal actin velocity distributions from noisy measurements. *bioRxiv* 1–22 (2020). doi:10.1101/2020.08.13.247304

278. Weiss, S. M. *et al.* IRSp53 Links the Enterohemorrhagic E. coli Effectors Tir and EspFU for Actin Pedestal Formation. *Cell Host Microbe* **5,** 244–258 (2009).

279. Kast, D. J. & Dominguez, R. IRSp53 coordinates AMPK and 14-3-3 signaling to regulate filopodia dynamics and directed cell migration. *Mol. Biol. Cell* **30,** 1285–1297 (2019).

280. Liu, P. S., Jong, T. H., Maa, M. C. & Leu, T. H. The interplay between Eps8 and IRSp53

contributes to Src-mediated transformation. *Oncogene* **29,** 3977–3989 (2010).

281. Rajagopal, S. *et al.* Scaffold proteins IRSp53 and spinophilin regulate localized Rac activation by T-lymphocyte Invasion and Metastasis Protein 1 (TIAM1). *J. Biol. Chem.* **285,** 18060–18071 (2010).

282. Misra, A. *et al.* Insulin Receptor Substrate protein 53 kDa (IRSp53) is a negative regulator of myogenic differentiation. *Int. J. Biochem. Cell Biol.* **44,** 928–941 (2012).

283. Sadhu, R. K., Penič, S., Iglič, A. & Gov, N. S. Modelling cellular spreading and emergence of motility in the presence of curved membrane proteins and active cytoskeleton forces. *arXiv* 1–30 (2021).

284. Oudin, M. J. & Weaver, V. M. Physical and chemical gradients in the tumor microenvironment regulate tumor cell invasion, migration, and metastasis. *Cold Spring Harb. Symp. Quant. Biol.* **81,** 189–205 (2013).

285. Bouzid, T. *et al.* The LINC complex, mechanotransduction, and mesenchymal stem cell function and fate. *Journal of Biological Engineering* **13,** 68 (2019).

286. Chang, W., Worman, H. J. & Gundersen, G. G. Accessorizing and anchoring the LINC complex for multifunctionality. *Journal of Cell Biology* **208,** 11–22 (2015).

287. Luo, Y., Lee, I.-W., Jo, Y.-J., Namgoong, S. & Kim, N.-H. Depletion of the LINC complex disrupts cytoskeleton dynamics and meiotic resumption in mouse oocytes. *Sci. Rep.* **6,** 20408 (2016).